THREE-DIMENSIONAL ULTRASTRUCTURAL ANALYSIS OF CORONAVIRUS AND ALPHAVIRUS REARRANGEMENTS OF HOST CELL ORGANELLE MEMBRANES

by

Elaine M. Mihelc

A Dissertation

Submitted to the Faculty of Purdue University

In Partial Fulfillment of the Requirements for the degree of

Doctor of Philosophy

Department of Biological Sciences

West Lafayette, Indiana

August 2020

THE PURDUE UNIVERSITY GRADUATE SCHOOL

STATEMENT OF COMMITTEE APPROVAL

Dr. Jason Lanman, Co-Chair

Department of Biological Sciences

Dr. Wen Jiang, Co-Chair

Department of Biological Sciences

Dr. Andrew Mesecar

Department of Biological Sciences

Dr. Claudio Aguilar

Department of Biological Sciences

Dr. Susan Baker

Department of Microbiology and Immunology
Loyola University Chicago

Approved by:

Dr. Jason Cannon

Dr. Janice Evans

To my family

ACKNOWLEDGMENTS

A PhD is far from a lone endeavor, and I am grateful for the many people whose presence in my life has allowed me to reach the point of completing my degree.

First, I would like to thank the members of my dissertation committee. To my advisor, Dr. Jason Lanman, thank you for your vision and contagious excitement for large volume electron tomography. I would like to thank Dr. Susan Baker for introducing me to the coronavirus field. Thank you for your helpful input on my manuscript, and for always making time for discussions. Thank you to Dr. Wen Jiang for academic guidance and stepping in to fill a role as co-advisor in the last couple years. Thanks also to my other committee members, Dr. Andrew Mesecar and Dr. Claudio Aguilar, for input throughout my PhD. Thank you to Dr. Seema Mattoo and Dr. Rob Stahelin for involving me in the JoVE video article which has been a bright spot in the final year of my PhD. Seema, I am grateful for your genuine desire to help me in my career. I would also like to thank Dr. Mark Browning, the coordinator of the Biology 110/111 course for which I was a teaching assistant for 5 years. Your leadership created a positive environment in which to spend time each week and to develop my teaching skills.

In addition to those who provided input during my PhD years, there are several research advisors to whom I owe everything in bringing me to the point of beginning my graduate studies. First, Dr. Martin Smith: thank you for giving me, as a 16-year-old, a meaningful role in a research project, as well as some of the best advice on academia that I have received. I will always remember and seek to emulate your academic generosity. I thank Dr. Glenn Marsch, my undergraduate research advisor at Grove City College, for introducing me to biophysics and to working at the interface of instrumentation and complex biological problems. Drs. Lei Wei and Jianjian Shi, thank you for always encouraging me to pursue academic excellence, particularly in working with my hands. I am grateful to Dr. Cliff Johnston for allowing me to work on interesting projects and introducing me to several new analytical techniques. Working in your lab was truly enjoyable and reignited my passion for research, and your patience, encouragement, and support have impacted my life greatly. I would also like to thank Dr. Richard Borgens for giving me independence as a technician, which allowed me to develop the confidence needed to pursue a PhD.

There are also many friends and colleagues who have enriched my grad school experience. To the members of the Lanman lab, Dr. Melissa Mikolaj, Stephanie Angel, and Logan Pankratz: thank you for the lab lunches, impromptu discussions, and companionship during long days in the lab or weekends on the Titan. Thank you Samantha Tinney for your contributions to my project and for your excitement to learn. I especially want to thank Dr. Amar Parvate for being the Best Labmate Ever and for the afternoon "peace offerings" of coffee and conversation. And thanks to Dr. Ranjan Sengupta for the many brainstorming sessions and discussions. Working on the alphavirus project, from the time we first saw the "cell of interest" at on the Titan to the final model presented in the manuscript discussion, has been one of the most intellectually stimulating projects of my career. I would also like to thank all my friends outside the lab, especially Summer and Adrial, for supporting me and putting up with my odd work hours and my incessant need to discuss double membrane vesicles.

Finally, it is impossible to adequately thank my family. To my siblings Catherine, Kirk, Leslie, and Laura: thank you for your friendship, laughter, and support no matter what. And Nolan, thanks for being the sweetest nephew ever. Your smiles have brought so much joy to my life. I also thank my parents, Dr. William Mihelc and Marilyn Mihelc for your life-long love for me and commitment to my education. I have never appreciated being raised and educated by you as much as I have during this PhD. Thank you for preparing me well. Mom, thank you for your interest in my project, for your listening ear and keen desire (and scientific ability) to understand the intricacies of my work, and for your many prayers.

And to the One who knows all: thank you for giving me this glimpse into the depths of your world. *And these are but the outer fringe of his works; how faint the whisper we hear of him!*

TABLE OF CONTENTS

LIST OF TABLES

LIST OF FIGURES

LIST OF ABBREVIATIONS

CM	convoluted membrane
CoV	coronavirus
CPV	cytopathic vacuole
CPVI	cytopathic vacuole I
CPVII	cytopathic vacuole II
CQ	chloroquine
cryo-EM	cryo-electron microscopy
cryo-ET	cryo-electron tomography
DMV	double membrane vesicle
EAV	equine arteritis virus
EM	electron microscopy
ER	endoplasmic reticulum
ERAD	ER associated degradation
ERGIC	ER-Golgi intermediate compartment
ET	electron tomography
FS	freeze substitution
HPF	high pressure freezing
LN_2	liquid nitrogen
LVT	large volume electron tomography
MERS-CoV	Middle East respiratory syndrome coronavirus
MHV	mouse hepatitis virus
mRNA	messenger RNA
NC	nucleocapsid
nsp	nonstructural protein (coronavirus)
nsP	nonstructural protein (alphavirus)
RdRP	RNA-dependent RNA polymerase
RTC	replication-transcription complex
RVN	reticulovesicular network

SARS-CoV-2	severe acute respiratory syndrome coronavirus 2
TEM	transmission electron microscopy
VEEV	Venezuelan equine encephalitis virus
VP	virus particle
zER	zippered ER

ABSTRACT

Single-stranded positive-sense RNA viruses commonly rearrange host cell organelle membranes into neo-organelles which are involved in virus replication and assembly. These organelles serve to concentrate viral and host factors as well as to conceal viral RNA replication activities from host cell surveillance. To date, many virus-induced membrane rearrangements have been studied by targeted electron tomographic (ET) imaging of specific viral structures at timepoints of known interest. However, the broad cellular context within which these membrane modifications occur and how they change over time are not well understood. A question spanning many virus families is the morphological mechanism of formation of membrane rearrangements. Additionally, it is largely unknown how the membrane modifications affect the morphology of the organelle of origin. In this study, we address specific questions about virus-derived organelles induced by two positive-sense RNA viruses: the coronavirus mouse hepatitis virus (MHV) and the alphavirus Venezuelan equine encephalitis virus (VEEV). Utilizing serial sectioning and montage imaging for ET, volumes representing approximately 10% of virus-infected cells were imaged and detailed organelle analysis was performed. Using MHV-infected cells, we demonstrate that coronavirus-induced double-membrane vesicles (DMVs) are formed by budding from the endoplasmic reticulum (ER) and are trafficked to lysosomes for degradation. The ER remains largely morphologically normal early in infection despite the presence of hundreds of DMVs; however, late in infection, virus envelopment in the ER lumen leads to loss of cisternal morphology. For the alphavirus VEEV, we analyze the structure and origin of virus-derived cytopathic vacuoles II (CPVII). We identify four distinct morphological forms of CPVII and provide evidence that all four forms are derived from the Golgi apparatus. Additionally, a protocol is outlined for a newly-developed method for improved cell ultrastructure during genetically-encoded peroxidase tagging of membrane-proteins. This method is also amenable to ET. Overall, this work provides morphological cellular context for virus-induced membrane rearrangements from two families of positive-sense RNA viruses. Analysis of virus-host cell interactions from this large-scale ultrastructural perspective has the potential to lead to new approaches and strategies to combat current and future viral diseases.

CHAPTER 1. INTRODUCTION

1.1 Historical perspective on virology and electron microscopy

The field of virology has been closely tied to techniques in electron microscopy throughout its history. At the turn of the 20th century, prior to the coining of the term "virus", it was known that infectious agents existed which were significantly smaller than bacteria, unable to live without a cell host, and unable to be visualized with light microscopy[1]. In 1931, Ernst Rusk introduced the electron microscope to the world, but it was thought that his new instrument would not be suitable for examining biological samples. It was believed that the harsh electron beam and the dehydration required of imaging a sample in a vacuum would obliterate any structures inside tissues and cells[2]. However, eight years after the invention of the electron microscope, Ernst Rusk's brother Helmut was the first to visualize a virus, tobacco mosaic virus, using the electron microscope[2], [3]. Helmut and his colleagues went on to image dozens of pathogens, including many other viruses such as poxviruses, varicella-zoster virus, and bacteriophages[4]–[7]. Over time, EM analysis of virus morphology became commonplace, with virus identification and classification largely dependent upon morphology.

In the 1950s, the cellular effects of virus infection became an area of research. One of the first viruses to be studied in this way was poliovirus, where cytoplasmic bodies were identified which were related to virus infection, but did not seem to be associated with virus particle formation[8]. The remainder of the century saw many electron microscopy studies which described virus-derived modifications of cells and organelles. In the early 2000s, cellular electron tomography (ET) was first used to image some of these membrane rearrangements in 3D, the first being modified mitochondria induced by Flock House virus infection[9]. This work has been followed by ET studies of virus-derived structures from numerous families, including major animal, plant, and insect pathogens. Additionally, the explosion of the field of cryo-electron microscopy (cryo-EM) and cryo-electron tomography (cryo-ET) in recent years has led to unprecedented structural understanding of virus particles and their constituent proteins. Much like the two Rusk brothers, the fields of virology and electron microscopy have remained close kin as they have grown up together over the last century. Electron microscopy advances make way for greater understanding

of virus morphology, structure, and cellular effects; new understandings lead to new questions which in turn provide impetus to generate new technologies.

1.2 Positive-sense RNA virus families and their membrane rearrangements

Single-stranded positive-sense RNA viruses include significant human pathogens such as poliovirus, hepatitis C virus, Zika virus, SARS-coronavirus, and the newly emerged SARS-CoV-2 causing the current global pandemic of coronavirus disease 2019 (COVID-19). These viruses are classified based on their single-stranded, positive-sense RNA genome which can act as messenger RNA (mRNA) and be directly translated with the host cell cytoplasm. Positive-sense RNA viruses commonly commandeer the membrane-bound organelles of a cell, rearranging them to create new viral organelles in which to complete essential elements of their lifecycles[10]–[12]. These neo-organelles are often associated with viral replication and are hypothesized to aid in concentrating viral proteins, creating a structural environment in which the virus can anchor its replication machinery and efficiently perform replication, and protect the virus's rogue activities from being detected by the cell's innate immune system[10], [13], [14]. Individual viruses make use of a variety of membrane-bound organelles, including mitochondria, endosome/lysosome, Golgi, and endoplasmic reticulum (ER) [10]. These rearrangements as described in 3D by ET are described in the subsequent sections and are summarized in Table 1.1.

Table 1.1. 3D rearrangements produced by positive-sense RNA viruses, as described by electron tomography. Abbreviations: FHV, Flock House Virus; CVB3, Coxsackievirus B3; EMCV, Encephalomyocarditis Virus; RUBV, Rubella Virus; HCV, Hepatitis C Virus; DENV, Dengue Virus; WNV, West Nile Virus; TBEV, Tick-Borne Encephalitis Virus; ZIKV, Zika Virus; SARS-CoV, Severe Acute Respiratory Syndrome Virus; MHV, Mouse Hepatitis Virus; EAV, Equine Arteritis Virus.

Virus Family	**Genus**	**Virus**	**Organelle**	**Membrane Rearrangements**	**ET References**
Nodaviridae	Alphanodavirus	FHV	mitochondria	spherules	Kopek 2007 [9]
Picornaviridae	Enterovirus	Poliovirus	ER, Golgi	single membrane vesicles & tubules, DMVs	Belov 2012 [15]
		CVB3			Limpens 2011 [16]
	Cardiovirus	EMCV			Melia 2018 [17]
Togaviridae	Rubivirus	RUBV	late endosome/ lysosome	spherules	Fontana 2010 [18]
Flaviviridae	Hepacivirus	HCV	ER, Golgi	DMVs, CM	Romero-Brey 2012[19] Ferraris 2013[20]
	Flavivirus	DENV	ER	invaginated vesicles (spherules)	Welsch 2009 [21] Junjhon 2014 [22]
		WNV			Gillespie 2010[23]
		TBEV			Miorin 2013 [24] Bily 2015 [25]
		ZIKV		invaginated vesicles (spherules), zippered ER	Cortese 2017 [26]
Coronaviridae	Betacoronavirus	SARS-CoV	ER	DMVs, CM	Knoops 2008 [27]
		MHV			This study, Chapter 2
	Gammacoronavirus	IBV	ER	DMVs, double membrane spherules, zippered ER	Maier 2013 [28]
Arteriviridae	Alphaarterivirus	EAV	ER	DMVs	Knoops 2012 [29] van der Hoeven 2017 [30]

1.2.1 *Nodaviridae*

The Nodavirus Flock House virus (FHV) modifies mitochondrial membranes by forming small spherules. FHV membrane rearrangements were the first to be described in 3D using ET. Spherules were described with average diameter ~50 nm. These spherules are localized to both the inner and outer mitochondrial membranes, and the interior of the spherules is open to the cytoplasm by an ~10 nm neck[9]. Later work visualized the spherule structure in greater detail, revealing coiled filaments of RNA within the spherule, and that the spherule size correlated with

the RNA template length[31]. The replication protein, protein A, was found to be arranged in a ring structure at the neck of the spherule, and subtomogram averaging revealed a twelve-fold symmetry in this structure[31].

1.2.2 *Picornaviridae*

Picornaviruses of two genera have been studied by 3D EM methods. Enteroviruses coxsackievirus B3 (CVB3) and poliovirus both were shown to rearrange ER and Golgi membranes into single walled tubules and double membrane vesicles (DMVs)[15], [16]. Single membrane tubules predominate early in infection and decrease in number over time, while DMVs increase in number as infection progresses. Late in infection, multi-lamellar structures are visualized, which appear to form by the wrapping of DMVs by additional membranes [16]. Large volume imaging utilizing serial block face scanning electron microscopy (SBF-SEM) revealed that the virus-derived membrane structures have greater association with ER early in infection and Golgi later in infection, and revealed that the regions are enriched in lipid droplets [32]. Encephalomyocarditis virus (EMCV), from the genus *Cardiovirus*, has been shown to induce remarkably similar membrane rearrangements to the enteroviruses, including single and double membrane vesicles. Additionally, the ET study showed morphological evidence that single membrane vesicles and tubules are converted into double membrane vesicles[17]. It thus appears that many of the structural features of organelle rearrangement are conserved among members of the picornavirus family.

1.2.3 *Togaviridae*

Togaviruses include alphaviruses and the rubivirus, Rubella virus (RUBV). RUBV replication occurs on modified endosome or lysosome membranes, referred to as cytopathic vacuoles (CPVs). CPVs are of large size, up to 2 microns[33]. 3D analysis revealed that these large compartments contain variable structures including stacked membranes, rigid sheets, small vesicles, and larger vacuoles. CPVs were found closely associated with rough ER and Golgi in what were termed “virus factories” [18]. Alphaviruses also modify late endosomes or lysosomes in order to form CPVs. These organelles were first described by EM in 1968, and are distinguished by the presence of spherules inside the outer surface of the vacuole[34]. Although no 3D ultrastructural studies

have been done on alphavirus spherules, 2D data indicates that they have a diameter of ~50 nm and are connected to the cytoplasm by a ~10 nm diameter neck, similarly to nodavirus FHV spherules[34]. Spherules form on the plasma membrane, and are internalized into endosomes, although in the case of Chikungunya virus, the spherules remain at the plasma membrane and do not form CPVI [35]–[37]. The spherules do have a central density, but high-resolution cryo-EM studies are needed to determine if a proteinaceous ring structure is present at the spherule neck as is the case in FVH spherules [31].

1.2.4 *Flaviviridae*

The flavivirus family is perhaps the most thoroughly studied by cellular ET. Viruses from two genera have been imaged, and were found to induce quite dissimilar membrane rearrangements, though all of the rearrangements are ER-derived. The hepacivirus Hepatitis C virus (HCV) induces a membranous web of contiguous vesicles, continuous with the ER. The membranous web also includes markers for COP vesicles, endosomes, mitochondria, and lipid droplets, indicating that multiple cellular components are required for the viral replication factory [19], [20]. The membranous web includes DMVs which are often connected to the ER and protrude into the cytoplasm, and multi-lamellar vesicles. In 8% of the DMVs analyzed, a ~10 nm opening was found, which is similar in size to the openings present in nodavirus and togavirus spherules, and thus it is tempting to speculate that the openings are involved in shuttling newly synthesized RNA out to the cytoplasm for virus particle assembly[19].

Members of the *Flavivirus* genus which have been imaged by ET include Dengue virus (DENV), West Nile virus (WNV), tick-borne encephalitis virus (TBEV), and Zika virus (ZIKV), all of which have similar membrane rearrangements[21]–[26]. These viruses induce formation of an ER-derived network consisting of convoluted membranes and vesicles located within the ER lumen. Vesicles are often arranged in groups of several vesicles within dilated ER, referred as vesicle packets. These 90-nm vesicles have 10-nm pores opening their interior to the cytoplasm. Flavivirus particles also assemble on ER membranes, and a close spatial relationship has been observed between the vesicle pore, and assembling virus on ER directly opposite the pore. DENV also infects mosquitoes, and ET of DENV-infected mosquito cells revealed similar vesicle packets in the ER, closely associated with budding virus. However, no convoluted membranes were

observed [22]. A unique structure observed in ZIKV-infected cells in addition to the typical rearrangements was zippered ER. These regions of ER with very little lumenal volume were often adjacent dilated regions filled with vesicles [26], [38].

1.2.5 *Coronaviridae*

Prior to the Severe Acute Respiratory Syndrome coronavirus (SARS-CoV) outbreak in 2002, mouse hepatitis virus (MHV) was the most thoroughly studied betacoronavirus. MHV induces membrane rearrangements including double membrane vesicles and convoluted membranes associated with replication [39]–[41]. These vesicles of 100-300 nm diameter are believed to originate from the ER, and were found to increase in number along with the progression of infection up to 10 hours post infection[41]. ET of SARS-CoV-infected cells revealed that DMVs and CMs were connected by small membrane connections into what was referred to as a "reticulovesicular network" [27]. Middle East Respiratory Syndrome coronavirus (MERS-CoV) also induces formation of DMVs of similar size to those of MHV and SARS-CoV, along with CM [42]. Interestingly, no openings from betacoronavirus DMVs to the cytoplasm have been observed, leading to questioning whether DMVs are the site of active replication. The gammacoronavirus infectious bronchitis virus (IBV) induces the formation of ER-connected DMVs as well as double-membrane spherules; however, no convoluted membranes were observed. Spherules are 60-80 nm in size and have an ~5 nm pore opening to the cytoplasm. Spherules are located in regions of paired ER termed zippered ER[43]. IBV is the only positive-sense RNA virus to form both DMVs and spherules. Open spherules are clearly associated with replication and the pore is required for transfer of RNA to the cytoplasm for virus assembly. However, the role of closed DMVs is unknown.

1.2.6 *Arteriviridae*

Arteriviruses belong to the order *Nidovirales* along with coronaviruses. Equine arteritis virus (EAV) induces formation of DMVs containing an inner double-stranded RNA density, with no opening to the cytosol[29]. DMVs are ~100 nm in diameter, smaller than coronavirus DMVs, and no convoluted membranes are present [29]. Additionally, a network of tubules containing

nucleocapsid were observed [29]. ET revealed morphological evidence for two different mechanisms of DMV formation: double budding and wrapping of zippered ER [30].

1.2.7 Common morphological themes

Two overarching morphological themes emerge from analysis of the structures formed by positive-sense RNA viruses for replication. The invaginated vesicle, or spherule, form is most common, being present on various organelles such as mitochondria in nodaviruses, late endosomes or lysosomes in togaviruses, and ER in flaviviruses and some coronaviruses. Spherules have a fairly narrow size range between 50-90 nm, and all have small pore-like openings to the cytoplasm which appear to be used for transfer of newly synthesized RNA out to cytoplasmic locations for assembly into new virus particles. The morphology of spherules is thus in excellent agreement with their function in harboring the replication complex in infection.

The second morphological form for replication organelles is the double membrane vesicle, present in picornaviruses, coronaviruses, arteriviruses, and the flavivirus HCV. The majority of DMVs form from the ER, while some DMVs in picornaviruses may have a Golgi origin. DMVs are generally larger than spherules, ranging in size from about 100-300 nm. Interestingly, while the double-stranded RNA replication intermediate is associated with DMVs, in many cases no pore is visible in DMVs. Small openings have only been observed for HCV, and those in less than 10% of DMVs. The dearth of observable openings leads to several plausible explanations. One is that the pore is transient, either present for a short time prior to closing, or dynamically opening and closing periodically to release new RNA. A second option is that DMVs may include a proteinaceous channel with which to pass RNA. Finally, DMVs may not be associated with active replication at all, but rather serve to protect viral replication byproducts from detection by the cell. With the exception of arteriviruses, DMV-forming viruses include other membrane rearrangements such as convoluted membranes which could be the site of active replication. This potentially positions DMVs as end-stage vesicles which are filled with RNA and protein waste from replication. These products could be loaded into DMVs while they are forming, before being sealed off from the cytoplasm. While the forms of DMVs are similar across many positive-sense RNA virus families, it is also possible that their functions are slightly different. Many interesting questions remain about DMVs, their structure, and their role in virus replication and infection.

1.3 Coronaviruses

1.3.1 Human coronaviruses

Coronaviruses (CoV) cause respiratory and gastrointestinal disease in a wide variety of mammals and birds. Human coronaviruses are typically mild respiratory viruses causing the common cold; however, in the past 20 years, three new human CoV with significant mortality have emerged. All three viruses are believed to have originated in bats, which are a large reservoir for coronaviruses. It is expected that CoV will continue to cross species from bats and other animals into humans in the future, and thus the study and understanding of CoV is of relevance to global human health.
Severe acute respiratory syndrome (SARS) was a viral respiratory disease which was first identified in southern China in late 2002. SARS spread to 26 countries and infected 8098 people, with a mortality rate around 10%[44]. While SARS was readily spread by close contact with an infected individual or their respiratory droplets, persons with SARS were contagious only when symptomatic. Thus strict quarantining of patients and identification and isolation of close contacts proved to be effective strategies for containment. The outbreak was contained by late 2003, and no new cases of SARS have been identified since 2004 [44]. The viral causative agent of SARS was identified as a novel human coronavirus and named severe acute respiratory syndrome coronavirus (SARS-CoV) [45], [46]. It was determined that SARS-CoV most likely originated from a bat virus which evolved to cross a species barrier, allowing spread to humans via animal markets [47], [48].

Middle East respiratory syndrome (MERS) was another respiratory disease found to be caused by a novel coronavirus (Middle East respiratory syndrome coronavirus, MERS-CoV). MERS-CoV emerged in Saudi Arabia in 2012, with similar respiratory symptoms to SARS. Since that time, MERS cases have been identified in 27 countries, with a total as of May 21, 2020 of 2494 cases and 858 deaths, a case-fatality rate of 34% [49]. Over 84% of MERS cases have been diagnosed in Saudi Arabia, with a notable outbreak of 186 cases in the Republic of Korea in 2015[50]. Today, MERS-CoV cases continue to be present in low numbers, mostly centered in the Arabian Peninsula. Like SARS-CoV, MERS-CoV is thought to have its origin in bats[51]. The virus has been found to be endemic in dromedary camel populations for some time, and MERS-CoV was found to be able to be transferred from camels to humans through close contact[52], [53]. While research on

MERS-CoV is ongoing, currently no vaccine or specific treatment is available, and thus MERS continues to be a significant global health threat.

Currently CoV are in the global spotlight due to the pandemic caused by the human CoV severe acute respiratory syndrome virus 2 (SARS-CoV-2), a respiratory virus which causes coronavirus disease 2019 (COVID-19). According to the World Health Organization, 5 million cases of COVID-19 have been diagnosed worldwide to date, with over 325,000 confirmed deaths. COVID-19 has spread from its origin in Wuhan, China in late 2019, to 216 countries by the present (May 21, 2020). The United States has 1.5 million cases, leading to over 90,000 deaths[54]. On December 31, 2019, a cluster of cases of pneumonia of unknown origin were first reported in Wuhan, Hubei Province, China. The infectious agent was isolated and quickly identified by sequencing as a novel CoV which shared 79.6% sequence identity with SARS-CoV, hence the naming of the novel virus as SARS-CoV-2[55]. The bat origin of SARS-CoV-2 was confirmed by a 96% overall sequence identity with a bat coronavirus RaTG13[55]. The rapid and extensive spread of COVID-19 compared to SARS and MERS is likely due to the presence of large numbers of asymptomatic infection, as well as the ability to spread the infection in the presymptomatic period.

1.3.2 Coronavirus taxonomy and genome

Coronaviruses are pleomorphic, enveloped positive-sense RNA viruses belonging to Group IV based on the Baltimore classification. The family *Coronaviridae* is a member of the order *Nidovirales* along with families *Arteriviridae, Mesoniviridae,* and *Roniviridae*. Within the *Coronaviridae* family, viruses are divided into two subfamilies, *Coronavirinae* and *Torovirinae*. *Coronavirinae* includes four genera: alpha, beta, gamma, and delta coronaviruses. Two human CoV which cause mild respiratory infections are alphaCoV, 229E and NL63[56], [57]. Two other CoV causing mild human infections, OC43 and HKU1, are betaCoV, along with all three previously discussed major human pathogens: SARS-CoV, MERS-CoV, and SARS-CoV-2[58]. The murine virus, Mouse Hepatitis Virus (MHV) is also a betacoronavirus, and was one of the best-studied coronaviruses prior to the SARS outbreak in 2002.

Coronaviruses contain large RNA genomes ranging in size from 26 to 32 kilobases[59]. The genome includes a 3' poly (A) tail and a 5' cap, allowing it to be translated similarly to mRNA within the host cell. Approximately two-thirds of the genome contains the replicase gene, which includes two large open reading frames, ORF1a and ORF1b, and the final third encodes structural and accessory proteins (Figure 1.1 A). The two ORFs express two polyproteins, pp1a and pp1ab, the latter which is expressed via a ribosomal -1 frame shift[60]. The two polyproteins are processed into sixteen non-structural proteins (nsps) by viral proteases encoded within nsp3 and nsp5. The papain-like proteases (PLpro) in nsp3 cleave at three sites between nsps 1-4, while the viral main protease, a 3C-like protease in nsp5, cleaves between nsps 4-16 (Figure 1.1 B)[61], [62].

Following cleavage by the proteases, many of the nsps are assembled into a complex referred to as the replication transcription complex (RTC), where the factors are concentrated for RNA replication and transcription of sub-genomic RNAs. In addition to the aforementioned roles of nsps in cleavage of the polyproteins, each of the other nsps has one or multiple activities within the RTC. The RNA-dependent RNA polymerase (RdRp) is encoded by nsp12 [59], [63], and nsp7 and nsp8 are present in a hexadecameric complex which also contains polymerase activity[64]–[66]. Other nsps are involved in evasion of host cell immune response (nsp1) [67], RNA binding (nsp 9)[68], or contain domains related to helicase (nsp13) [69]–[71], exoribonuclease (nsp14)[72], endoribonuclease (nsp15)[73], [74], and AdoMetdependent (nucleoside-2'O)-methyltransferase (2'O-MTase) (nsp16)[75] activities. The ribonuclease activity is a unique feature of *Nidovirales*, and it may be involved in replication fidelity of such a large genome[76], [77] . Three of the nonstructural proteins, nsp3, 4, and 6, have hydrophobic transmembrane or membrane-associated domains which play a role in the membrane-association of the RTC and the membrane rearrangements induced by CoV infection (Figure 1.1 C) [78], [79].

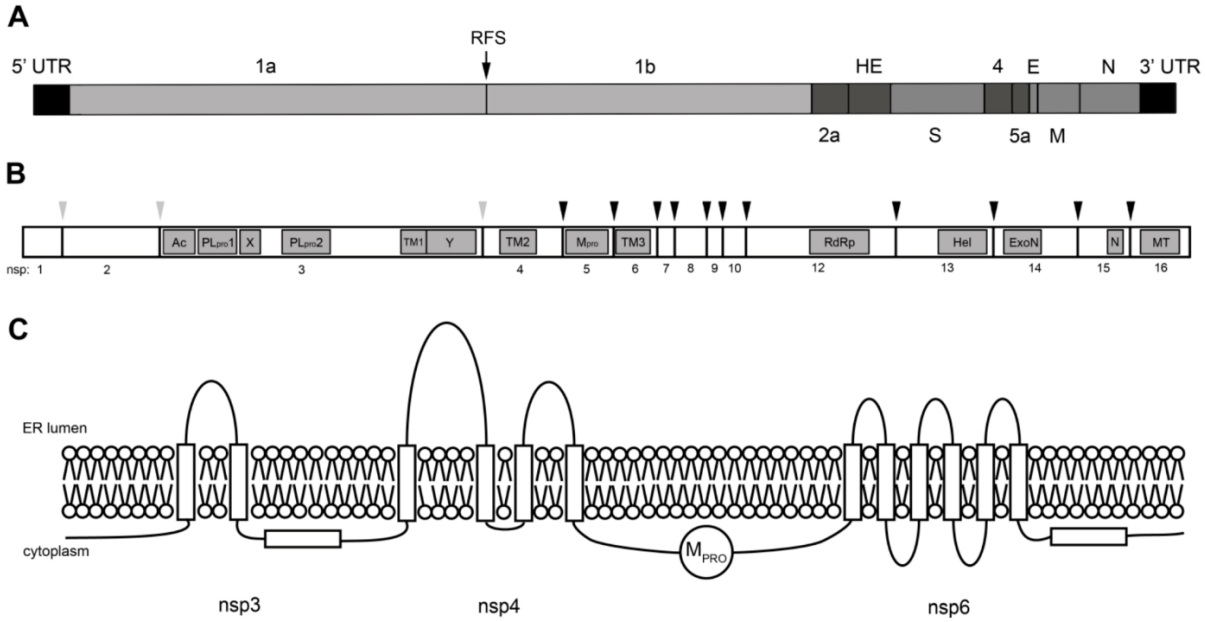

Figure 1.1. Schematic representation of the coronavirus MHV genome, nonstructural proteins, and membrane topology of nsps 3-6. **(A)** Representation of the 32-kB genome of MHV, including two open reading frames and genes encoding structural and accessory proteins. **(B)** Representation of pp1ab, with cleavage sites for virally encoded proteases PLpro1 and PLpro2 indicated by grey arrowheads, and cleavage sites for Mpro indicated by black arrowheads. Transmembrane domains (TM1, TM2, TM3 in nsp3, 4, 6) as well as domains for enzymatic activities such as RNA-dependent RNA polymerase (RdRp, nsp12), helicase (Hel, nsp13), exonuclease (ExoN, nsp14), endonuclease (N, nsp15), and methyltransferase (MT, nsp16). **(C)** Membrane topology of the membrane-spanning regions of the polyprotein. Figure was adapted from reference [80].

The CoV structural proteins are translated from a nested set of subgenomic RNAs. Structural proteins include spike (S), envelope (E), membrane (M), and nucleocapsid (N) and in some CoV the hemagglutinin esterase (HE) protein. The S protein is an ~150 kDa glycoprotein which creates the characteristic projections from the virion which constitute the crown (hence, the name *corona*-virus). S interacts with the receptor on the host cell, mediating the fusion and entry of the virus[56], [60]. M protein is the most abundant protein in the virion envelope, and it contains three hydrophobic transmembrane domains. M protein is extremely important in the formation of the virus particle, including through homotypic interactions with M, and interactions with E, S, and HE[81]. The E protein is a small transmembrane protein that in addition to structure is known as a viroporin[82], [83]. N, or nucleocapsid protein, is expressed in the greatest amounts of any viral protein, and its main role is to bind RNA[81]. While N does not have any transmembrane domains, it is often found in close association with membranes, including those of the replication

complexes[84], [85]. The HE protein is a membrane protein that is incorporated into virus envelopes of group 2 CoV, though its expression appears to be optional as it is not expressed in all MHV strains[86]. Structural proteins, along with newly synthesized genomic RNA are packaged together into coronavirus virions. CoV particles are generally spherical and pleomorphic, of approximately 100 nm diameter, and are visually characterized both in the cell and in negative stain by the presence of the large "corona" of spike proteins projecting from their surface (Figure 1.2)[87], [88]

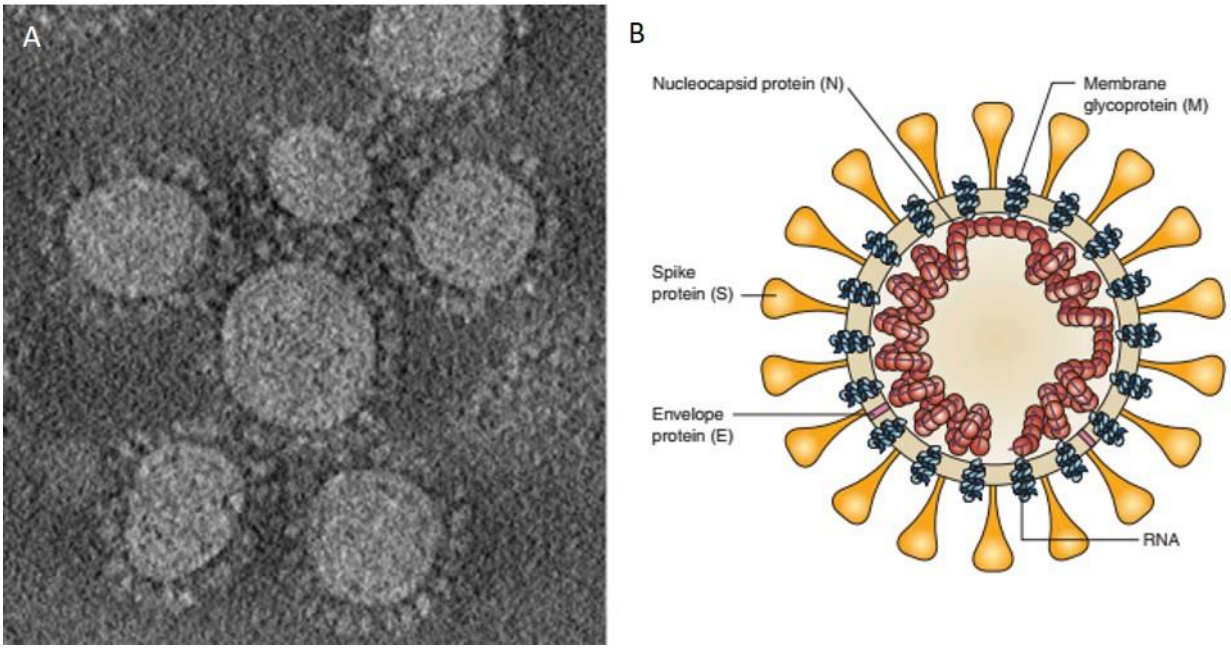

Figure 1.2. The coronavirus particle. **(A)** Virtual slice through a cryo-tomogram of MHV particles, adapted from reference [88]. **(B)** Representation of a coronavirus virion with the spike protein (orange), membrane protein (blue) and envelope protein (pink). The nucleocapsid-RNA complex is shown in the interior of the virion in red. This panel was adapted from reference [89].

1.3.3 Coronavirus lifecycle

The lifecycle of CoV within its host cell is diagrammed in Figure 1.3. Entry begins with the interaction between the S protein and a cellular receptor. The variation in S protein as well as the receptors which it binds to are the main distinguishing features which determine host-species specificity as well as tissue and cell specificity of CoV infection. Of note, SARS-CoV, SARS-CoV-2, and HCoV-NL63 all utilize angiotensin-converting enzyme 2 (ACE2) as their receptor[90]–[92]. MERS-CoV uses dipeptidyl-peptidase 4 (DPP4)[93] and MHV uses CEACAM1[94], [95]. Receptor-spike interaction facilitates attachment and fusion of the virus

and cellular plasma membrane by two sequential cleavages of S protein. The second cleavage exposes a fusion peptide which inserts into the membrane. This fusion occurs in endosomes for most CoV, but at the plasma membrane in MHV[60], [96], [97], which allows the release of the viral genome.

In the cytoplasm, the mRNA-sense genome is directly translated into the two polyproteins pp1a and pp1ab, which are cleaved by the viral proteases into sixteen nsps. Many of the nsps assemble into the replication-transcription complex (RTC). Within this complex, synthesis of genomic and sub-genomic RNAs takes place. The RTC itself is associated with modified membrane structures such as double membrane vesicles (DMVs) and convoluted membranes (CM)[27], [39]–[41], [98], [99]. These structures are formed by the actions and interactions of three nsps: nsp3, 4, and 6, and will be discussed in greater detail in the next section[78]. Translation of the nested set of sgRNAs produces the structural proteins, which are inserted into the ER and then processed through the secretory pathway. The initial site of assembly and budding of virus particles is the ER-Golgi intermediate compartment (ERGIC)[98], [100], [101], while late in infection, the ER becomes the major site of budding[101]. Virus particles mature via post-translational modifications of the structural proteins as virions proceed through the secretory pathway[81]. Viruses are believed to exit the cell via exocytosis in large smooth vesicles[81].

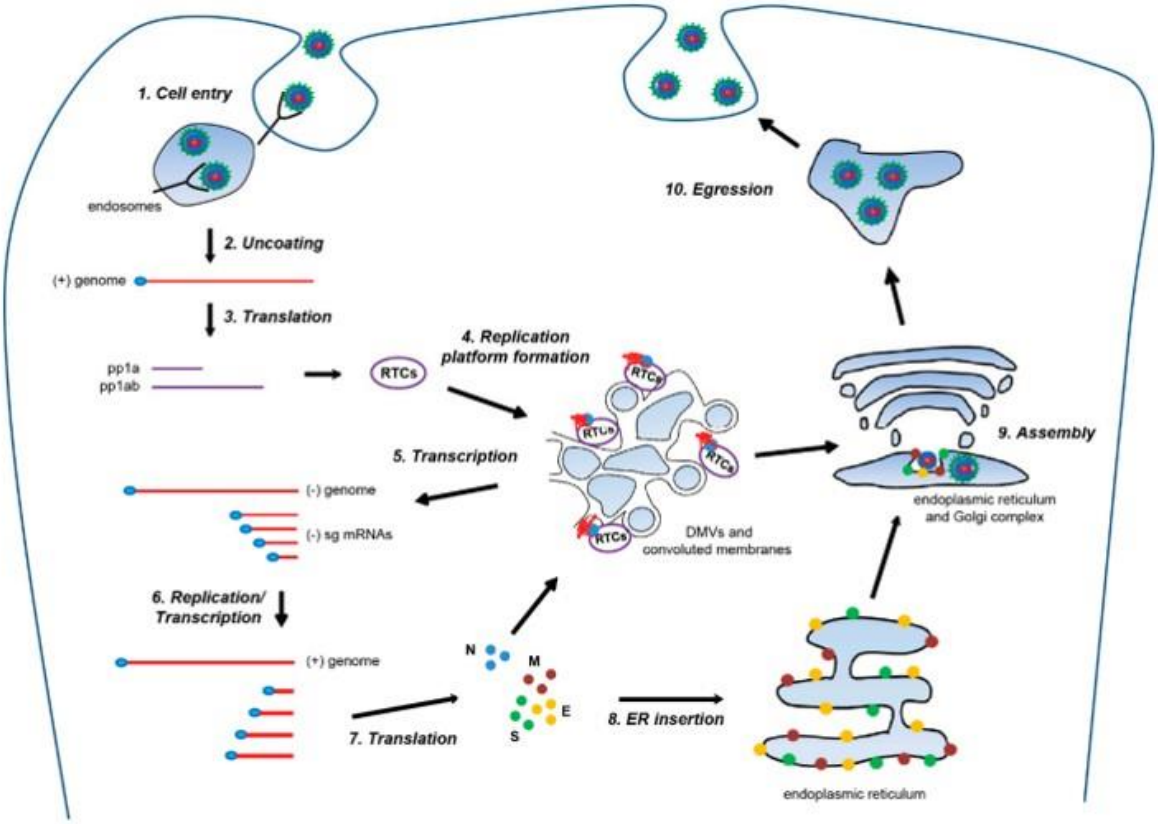

Figure 1.3. Coronavirus general lifecycle in a host cell. Entry occurs via interaction of the spike protein with the cell receptor, followed by internalization by receptor-mediated endocytosis (step 1). Viral RNA is released into the cytoplasm, where two ORFs are directly translated into 2 polyproteins which are cleaved into the 16 nonstructural proteins (steps 2-3). Nsps form the replication transcription complex as part of the reticulovesicular network of DMVs and CMs (step 4). Full length negative strand RNA and subgenomic (sg) negative strand RNA is synthesized (step 5) for use as a template to produce full-length genomic RNA and the positive-strand sgRNAs which are translated into the structural proteins S, E, M, and N (steps 6-7). Structural membrane proteins are inserted into the ER and processed through the secretory pathway for virion assembly in the ER, ERGIC and Golgi (steps 8-9). Viruses are released from the cell in vesicular packets (step 10). Figure adapted from reference [102].

1.3.4 Membrane rearrangements in coronavirus infection

Mouse hepatitis virus (MHV) is a Coronavirus which induces two main membrane rearrangements, termed double membrane vesicles (DMVs) and convoluted membranes (CMs), collectively referred to as the reticulovesicular network based on 3D electron tomography [27], [40], [41]. DMVs and CMs appear upon infection and are the location of the components required for replication, specifically newly synthesized RNA, viral nonstructural proteins (nsps) comprising the replication machinery, and the replicative intermediate double stranded RNA (dsRNA)[27], [40], [41]. While it is clear that DMVs and CMs are involved in replication, the precise location

of active replication and the mechanism by which it occurs are not well understood. Fluorescence microscopy data shows that nascent RNA colocalizes with both dsRNA and nsps early in infection, but colocalization is weak later in infection, suggesting that some structures containing dsRNA and nsps are involved in active viral RNA replication, while others are not [80]. Live-cell fluorescence microscopy reveals that replication structures can be divided into two classes based on size and mobility[103]. Coronavirus DMVs are believed to be derived from the ER, although they exclude traditional ER markers[27], [99], [104]–[109]. In fact, the only cellular markers found in association with DMVs are markers of the ER-associated degradation (ERAD) tuning pathway. These include EDEM1, Os-9, and LC3-I [109]. In their main functions in ERAD, EDEM1 and Os-9 function as luminal proteins which detect misfolded proteins that should be destroyed through ERAD [110]–[113]. These ERAD regulators must be tightly regulated themselves, as excess concentrations could lead to destruction of proteins still in the process of folding. ERAD tuning, therefore, is the process by which ERAD regulators are sequestered LC3-I containing vesicles and trafficked to lysosomes for degradation[114]–[116]. These vesicles are named EDEMosomes, and are morphologically identified as single-membrane vesicles which have been visualized in the process of budding from ER membranes[114]. Because CoV DMVs are double membrane vesicles, the precise morphological mechanism by which ERAD tuning leads to their formation is unknown.

1.4 Alphaviruses

1.4.1 Alphaviruses and their diseases

Alphaviruses are enveloped, positive-sense RNA viruses which infect a variety of vertebrates and invertebrates, including some viruses which cause human disease. Alphaviruses typically cause fevers, arthralgia, and encephalitis[117]. Chikungunya virus (CHICKV) can cause polyarthritis and rash in humans and other primates[118], [119]. Three encephalitic viruses include Venezuelan encephalitis virus (VEEV), Western encephalitis virus (WEEV), and Eastern encephalitis virus (EEV), which cause disease in humans and horses[120], [121]. Sindbis virus (SINV) and Semliki forest virus (SFV) are two of the earliest known and most commonly studied among the alphaviruses[122]. Alphaviruses are arboviruses and as such are transmitted by mosquitoes, most

commonly *Aedes aegypti* and *Aedes albopictus*[123]. While no vaccines or anti-viral treatments have been approved for use in alphavirus infection, research is ongoing in both arenas[124]–[128].

1.4.2 Alphavirus taxonomy and genome

Alphaviruses make up the *Alphavirus* genus in the *Togaviridae* family. The other genus in *Togaviridae* is *Rubivirus*, which contains only one virus, Rubella virus. There are 31 alphaviruses, each with a positive-sense RNA genome of 11-12 kb size[123]. Alphavirus genomes contain a 5' cap and poly-A tail like mRNA, which allows for direct translation within the host cell [129]. The genome encodes two open reading frames (ORFs) encoding two polyproteins. A schematic of the genome organization and information on nonstructural and structural proteins is shown in Figure 1.4.

The first polyprotein consists of nonstructural proteins (nsPs). Polyproteins P123 and P1234 are translated in differing amounts, are subsequently cleaved by nsP2 into smaller polyproteins, and eventually into the individual nsPs[130]–[132]. The individual nsPs as well as intermediate polyproteins have differing roles. NsP1 is responsible for membrane interactions of the replication complex via an amphipathic helix that associates with the cytoplasmic face of membrane[133]–[135]. This interaction is essential for virus replication[135]. NsP1 also contains methyltransferase and guanylyltransferase domains responsible for capping the genome[136]–[139]. NsP2, as already mentioned, contains protease activity, and it additionally has a helicase activity[140], [141]. The role of nsP3 is less well understood, but it may be involved in negative strand or subgenomic RNA synthesis[142]. The crucial RNA-dependent RNA polymerase resides in nsP4[143], and nsP4 is also involved in polyadenylation of the genome[144].

The structural precursor protein is translated from subgenomic RNA as CP-pE2-6K-E1[145]. This precursor is cleaved into four structural proteins. First, the capsid (CP) autocleaves and remains in the cytoplasm where it interacts with RNA to form the nucleocapsid portion of the virion. The cleaveage of CP uncovers the N-terminal signal sequence in pE2 which initiates translocation of the remainder o fthe polyprotein into the ER[146]. pE2 is folded and processed through the secretory pathway until it reaches the Golgi where it is cleaved by a cellular furin protease into the E2 and E3 glycoproteins[123], [147], [148]. E2 associates with E1 as trimeric E2-E1 heterodimers,

which form the spikes on the final virus particle[149], and E2 is involved with interaction with cellular receptors during virus entry[150]. E3 is not present on virus particles for many alphaviruses, with notable exception of VEEV and SFV[151]–[153]. 6K is a small structural protein that is cleaved from pE2 and E1 in the ER. It is found in low numbers in alphavirus particles[154]–[156]. Its role in virus infection is not fully understood, but 6K does have ion channel activity making it a viroporin[157]–[159], and it is also believed to be important in the transport of glycoproteins and virion assembly[160]. The final structural protein, E1, is the glycoprotein which forms an icosahedral shell over most of the virus envelope. E1 is involved in fusion with endosomes during entry via the pH-dependent exposure of a fusion peptide in E1[161]–[163].

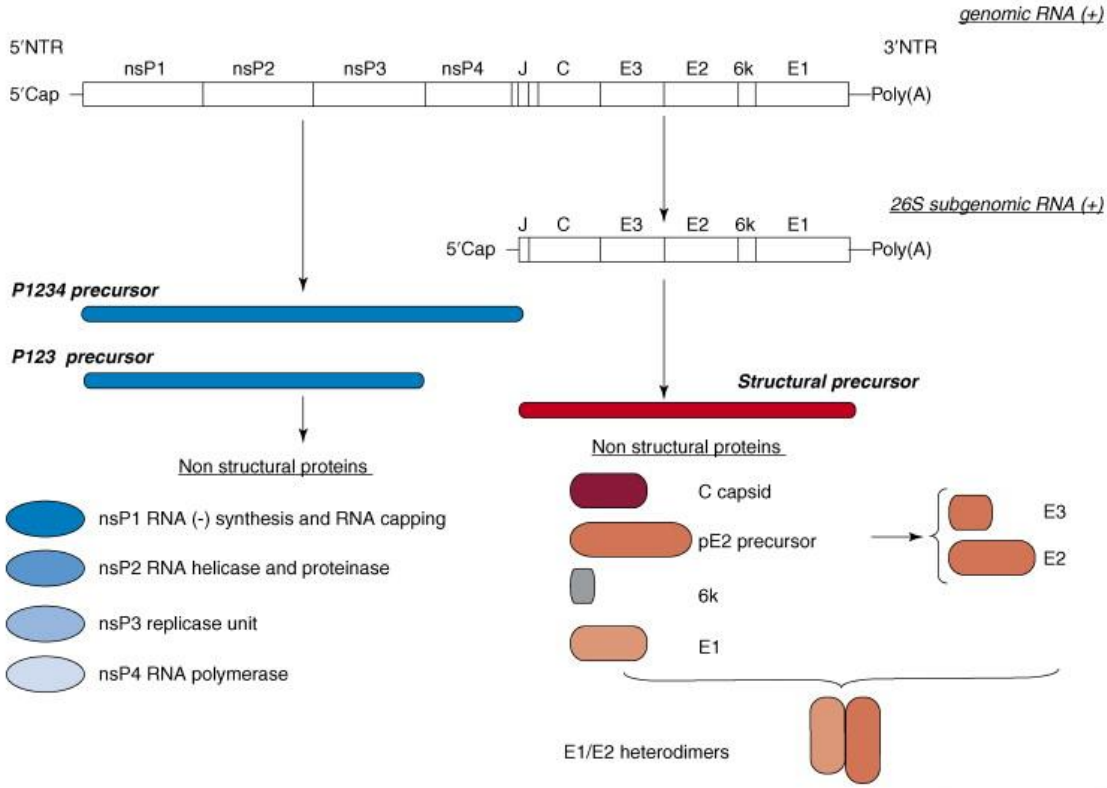

Figure 1.4. Schematic of the alphavirus genome organization, non-structural proteins and their activities, and structural proteins and their processing. Details are provided in section 1.4.2 of the text. Figure was adapted from reference [164].

Alphavirus particles are spherical with diameters of ~70 nm and T=4 icosohedral symmetry. The core consists of an icosahedral nucleocapsid made up of the RNA genome in complex with 240 copies of capsid protein[165]. A virus particle contains 240 copies each of E1 and E2, with smaller

numbers of 6K[123]. E1 and E2 form heterodimers, which associate in trimers to produce a total of 80 spikes per particle. Due to their symmetry, alphavirus particles are amenable to cryoEM reconstruction, and structures have been determined for several alphaviruses (Figure 1.5) [149], [151], [166].

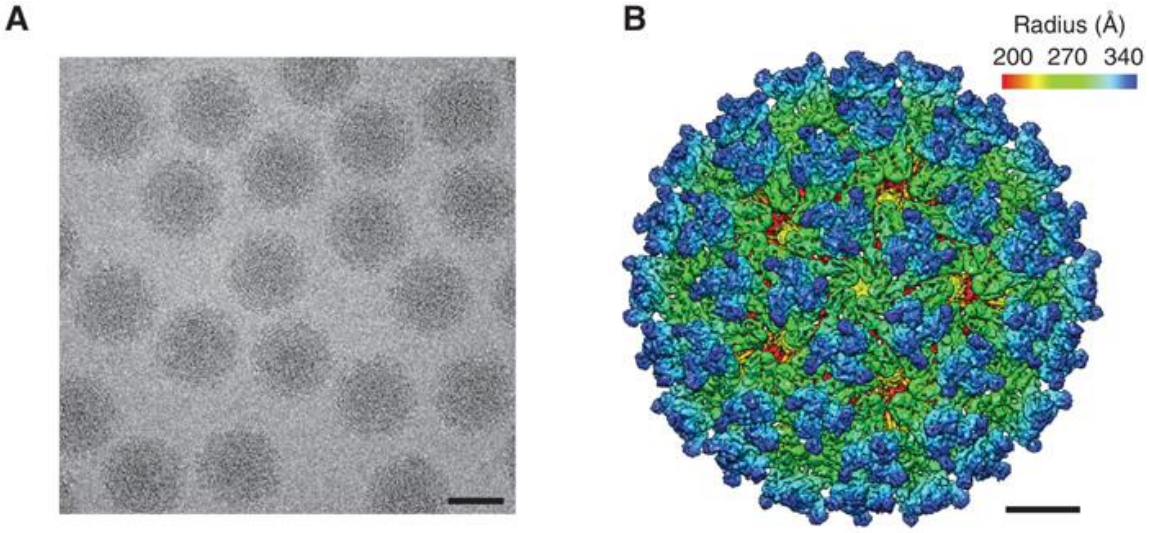

Figure 1.5. The alphavirus particle. (A) A cryo-EM projection image of VEEV strain TC-83 particles embedded in vitreous ice. Scale bar: 50 nm. (B) 3D reconstruction of VEEV strain TC-83, with radial coloring as indicated and a resolution of 4.8 Å. The E1 basal triangle (green) and E2 central protrusion (blue) is visible for each spike. Scale bar: 10 nm. Figure adapted from reference [167].

1.4.3 Alphavirus lifecycle

Alphavirus entry begins with interaction of E2 and the cell receptor. There is not considered to be one cell receptor for alphaviruses. In fact, the vast number of species and cell types which can be infected by this group of viruses suggests either a ubiquitously expressed receptor, or that multiple receptors could be utilized[150]. The virus is internalized by clathrin-mediated endocytosis[168], [169]. At low pH, the E1-E2 heterodimer undergoes a conformational change, revealing a fusion loop which causes fusion of the viral envelope with the endosomal membrane. The nucleocapsid is released into the cytoplasm and quickly disassembled to release the RNA genome[170], [171]. The mRNA-sense genome can be directly translated utilizing the host cell's ribosomes. The translation and subsequent processing of the two nonstructural polyproteins initiates replication, which occurs in relation to spherule structures on the plasma membrane or on the surface of vesicles of endo-lysosomal origin[34], [35], [37]. Endosomal structures with spherules are termed cytopathic vacuole type I (CPVI) [172]. These spherules are associated with replication of the

genomic and subgenomic RNA. Subgenomic RNA is translated into a polyprotein which is subsequently processed into the structural proteins. The capsid protein autoproteolytically cleaves itself from the structural polyprotein, revealing a signaling sequence on pE2 which translocates the remaining polyprotein to the ER for folding and processing through the secretory pathway[146]. Capsid protein assembles with genomic RNA into a nucleocapsid (NC) in the cytoplasm through an unknown mechanism[173]. Budding of new virus particles occurs at the plasma membrane. When the NC comes into contact with regions of the plasma membrane that have assembled glycoprotein spikes in a lattice, the capsid protein can interact with the glycoproteins to curve the membrane and bud out[174]. A cartoon of the alphavirus lifecycle is shown in Figure 1.6.

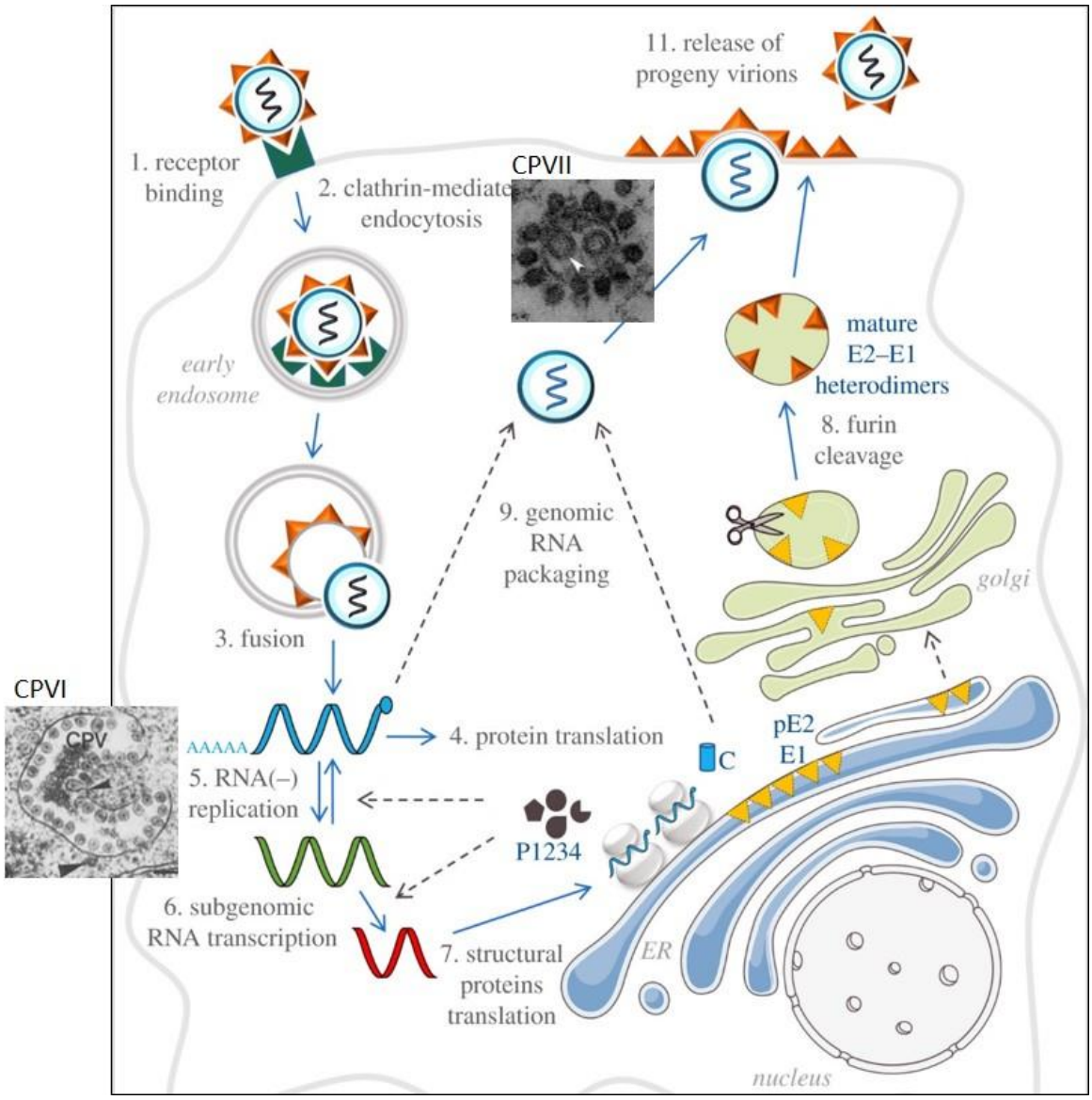

Figure 1.6. Alphavirus general lifecycle in a host cell. Entry occurs via interaction of the spike protein with the cell receptor, followed by internalization by clathrin-mediated endocytosis (steps 1-2). Viral RNA is released into the cytoplasm, where the genome is translated into a polyprotein (P1234) which is cleaved into the 4 nonstructural proteins (steps 3-4). NsPs form the replication transcription complex as part of spherules on CPVI. Full length negative strand RNA is synthesized for use as a template to produce full-length genomic RNA, and sgRNA is translated into the structural prolyprotein (steps 5-7). After the autoproteolytic cleavage of capsid (C), the remaining polyprotein is translocated into the ER and processed through the secretory pathway, including final cleavage of glycoproteins (step 8). Capsid is packaged with newly synthesized genomic RNA and the resulting nucleocapsids are transported to site of budding at the plasma membrane, at least partially via CPVII. (steps 9-11). Figure adapted from references [34], [174], [175].

1.4.4 Membrane rearrangements in alphavirus infection

As with other +RNA viruses, alphaviruses modify cellular membranes to carry out their lifecycle. As was mentioned previously, CPVI are the site of replication and are large endosomal structures of 1-2 μm in diameter. CPVI are readily recognized under the electron microscope by the presence of regularly-sized, approximately 50 nm diameter spherules. Spherules are located inside the outer surface of the vacuole, and open to the cytoplasm via a narrow neck[34]. Based on their structure, spherules may provide a degree of protection from host cell detection of viral RNA, but they are open to the cytoplasm in order to release the products of replication. Spherules initially form on the plasma membrane, and in the case of SFV, SINV, and VEEV, they are endocytosed into CPVI. In CHIKV, the spherules remain on the plasma membrane[35]–[37].

Cytopathic vacuole II (CPVII) are smaller than CPVI (0.2-1.5 μm) and are vesicles characterized by the presence of nucleocapsids (NC) bound to their membrane. CPVII are not visualized in the earliest stages of infection, but appear to be a later stage structure[172], [174], [176]. CPVII are heterogeneous in appearance and have been observed as uni- or multi-lamellar forms, some with fully enveloped virions inside or other vesiculo-tubular membranes[172], [174]. The binding of NC to CPVII membranes is enabled by the interaction of capsid protein with E2 in the membrane[177]–[179]. Early studies suggested a medial or trans Golgi origin for CPVII based on morphology[180], [181]. CPVII are thought to be involved in co-transport of NC and E1/E2 glycoproteins to the plasma membrane for efficiency of budding[174], [180], [182]. The process and precise role of CPVII are not fully understood.

CHAPTER 2. CORONAVIRUS INFECTION INDUCES PROGRESSIVE RESTRUCTURING OF THE ENDOPLASMIC RETICULUM INVOLVING THE FORMATION AND DEGRADATION OF DOUBLE MEMBRANE VESICLES

A version of this chapter has been submitted for publication.

Coronaviruses rearrange host cell membranes to form a reticulovesicular network (RVN) of double membrane vesicles (DMVs) and convoluted membranes (CMs) associated with viral replication. The RVN is connected to the endoplasmic reticulum (ER), and DMVs form via the ER-associated degradation (ERAD) tuning pathway. ERAD tuning vesicles, termed EDEMosomes, bud from the ER and are rapidly trafficked to lysosomes for degradation. Unlike EDEMosomes, DMVs are surrounded by two lipid bilayers, are connected to the ER via the RVN, and accumulate within the cell. While electron tomography has been performed on small portions of the RVN, the full extent of the RVN is not known or how RVN formation affects ER morphology. Additionally it is not known how DMVs form from the ER or whether DMVs evade the degradative fate of EDEMosomes. In this work, we examined coronavirus-infected cells at multiple timepoints during infection using serial-section electron tomography. We provide a comprehensive 3D analysis of the ER and RVN, including nearly 700 DMVs. We show that DMVs have a life cycle consisting of formation by budding from the ER, separation from the RVN, and degradation in lysosomes. The RVN breaks down late in infection, concurrent with the ER becoming the main budding compartment for new virions. This analysis provides a broad perspective on the ultrastructure of the RVN and provides insight into the formation of DMVs as well as the first evidence for their degradation. This work raises new questions about the dynamic involvement of cellular organelles and pathways in coronavirus infection.

2.1 Introduction

Coronaviruses (CoV) are members of the *Coronaviridae* family of enveloped, positive-sense RNA viruses which include human pathogens Severe Acute Respiratory Syndrome Coronavirus (SARS-CoV), Middle East Respiratory Syndrome Coronavirus (MERS-CoV), and the recently emerged Severe Acute Respiratory Syndrome Coronavirus 2 (SARS-CoV-2). Like other positive-sense

RNA viruses, CoV rearrange host cell organelle membranes to form neo-organelles involved in viral replication (reviewed in [10]). In CoV infection, replication takes place in connection with a virus-induced reticulovesicular network (RVN) consisting of double membrane vesicles (DMVs) and convoluted membranes (CM)[27], [39], [41], [98], [99]. The RVN lacks traditional ER markers, but is continuous with the ER which is believed to be the membrane source of these structures[27], [99], [104]–[109]. The RVN has been described by electron tomography as DMVs, CMs, and ER which are connected via small membranous connections[27]. The size of an individual tomogram has limited the analysis to less than 10 partial DMVs[27]. However, large numbers of DMVs have been observed in infected cells, and the RVN is understood to be quite extensive. The full extent of the RVN and how its formation affects ER morphology is not known.

DMV biogenesis is believed to occur via the ER-associated degradation (ERAD) tuning pathway. DMVs contain markers of ERAD tuning, including EDEM1, Os-9, and LC3-I[109]. EDEM1 and OS-9 are luminal ER proteins which help in detection of misfolded proteins for ERAD[110]–[113]. Levels of these ERAD regulators are tightly controlled by ERAD tuning. In this process, EDEM1 and OS-9 are sequestered into LC3-I containing vesicles, termed EDEMosomes, which bud from the ER and are trafficked to lysosomes for degradation[114]–[116]. Unlike EDEMosomes, CoV DMVs are bounded by two membranes, are connected to the ER via the RVN, and accumulate within the cell over the course of infection[27], [40], [41]. It is not understood precisely how DMVs are formed from the ER or how infection tethers DMVs to the RVN to evade the degradative fate of EDEMosomes.

In addition to host cell membranes' involvement in CoV replication, they also play a role in assembly and budding of new virus particles (VP). VP obtain their envelopes by budding into the lumen of the organelles of the secretory pathway. While the ER-Golgi intermediate compartment (ERGIC) is the major budding compartment, assembly of virus particles on the Golgi and ER has also been observed [101], [183]. Tooze, et al. suggested that the budding compartment changes over time and that the ER becomes the major budding compartment late in infection[101]. This observation predates the discovery and description of the RVN. The involvement of the ER membranes in both RVN formation and late stage envelopment raises questions as to how the ER houses both processes and how its morphology may change to reflect those disparate roles.

To address these questions of RVN and ER morphology and DMV formation during CoV infection, a high-resolution, large volume imaging technique was needed. To date, large-scale ER structure in mammalian cells and yeast has been visualized using focused-ion beam milling scanning electron microscopy (FIB-SEM), serial block face SEM (SBF-SEM), or electron tomography (ET)[184]–[187]. Three-dimensional analysis of small portions of the CoV RVN showed that the high resolution of electron tomography (ET) enabled visualization of double membranes as well as small membrane connections within the RVN[27]. This resolution was required for our study. In order to achieve a large volume by ET, we utilized both a montage image collection and collected tomograms on serial sections. The resulting volumes we refer to as large volume tomograms (LVT).

In this work, we used large volume ET to perform a comprehensive morphological analysis of the RVN and ER at two distinct timepoints in the CoV Mouse Hepatitis Virus (MHV) infection. We show that DMVs have a life-cycle consisting of budding from the ER, separating from the RVN, and trafficking to lysosomes for degradation. The final step occurs through ERAD tuning, and accounts for the breakdown of the RVN late in infection. The dynamic nature of the RVN over the course of infection occurs concurrently with a shift in virus assembly from the ERGIC to the ER. Together, these data reveal the highly dynamic nature of CoV infection within the cell, in particular in its varied interaction with the ER.

2.2 Materials and Methods

2.2.1 Virus and Cells

Murine 17Cl-1 fibroblasts[188] were cultured in Dulbecco's modified Eagle's medium (DMEM) supplemented with 5% fetal bovine serum (FBS), 10% Tryptose phosphate broth, and Pen/Strep at 37 ^{o}C in a 5% CO_2 atmosphere. Cells were infected with mouse hepatitis virus strain A59 [189](MHV-A59) at multiplicities of infection (m.o.i.) between 0.1 and 10 as indicated. MHV-A59 expressing green fluorescent protein as a fusion with the replicase protein nsp3 (MHV-Δ2-GFP3[190]) was used for fluorescence imaging.

2.2.2 Immunofluorescence microscopy

17Cl-1 cells were grown on glass coverslips and infected with MVH-A59 or MHV-Δ2-GFP3 at an m.o.i. of 0.1. At various times post infection between 4 and 16 hours, cell monolayers were washed in phosphate buffered saline (PBS), fixed with 100% methanol for 15 minutes at -20 ^{o}C, washed in PBS, and blocked overnight at 4 ^{o}C in 0.2% cold water fish skin gelatin in PBS. Cells were incubated with primary antibodies for 2 hours at room temperature, followed by washing, incubation in secondary antibodies for 1 hour, and final washes. Coverslips were mounted on glass slides using FluorSave reagent (Calbiochem) prior to imaging. Primary antibodies used were mouse monoclonal anti-M J1.3[191], rabbit polyclonal anti-calreticulin and rabbit monoclonal anti-Golgin-97 (Cell Signaling Technology). Goat anti-mouse FITC and goat anti-rabbit Texas Red (Invitrogen) were used as secondary antibodies. Confocal imaging was performed on a Nikon A1RMP laser scanning confocal microscope equipped with 488 nm and 561 nm lasers, using a 60x oil immersion objective with numerical aperture 1.4. Multi-channel imaging was performed sequentially for each laser, with line averaging of 2, utilizing the full 4k x 4k pixel CCD. NIS Elements software (Nikon) was used for data collection, and Fiji ImageJ was used for image cropping, channel overlay, and line intensities[192], [193].

2.2.3 Preparation of cells for electron microscopy and tomography

At the timepoints indicated in the text, MHV-A59-infected 17Cl-1 cells were washed with PBS, then incubated for 5 min. with 0.25% Trypsin-EDTA (Corning). Cells were pelleted at 500 x *g*, resuspended in a cryoprotectant of 20% bovine serum albumin in DMEM, and pelleted again. A small volume (2-3 μl) of the resulting cell pellet was loaded into the well of a 1.5 mm x 0.1 mm membrane carrier (Mager Scientific) and cryo-fixed using the EM PACT2 high pressure freezer (Leica). Cryo-fixed cells were processed by freeze substitution (FS) using an AFS2 automated freeze substitution unit (Leica). Briefly, frozen cell samples were incubated at -90 ^{o}C in a solution of tannic acid in acetone, followed by slowly warming to room temperature in a solution of uranyl acetate and osmium tetroxide in acetone (chemicals from Electron Microscopy Sciences). Over 30 cell preparation conditions were tested before choosing a cell line, FS chemical mix, and FS warming protocol which gave optimal preservation of virus-derived membrane rearrangements and membrane staining suitable for electron tomography. After FS, samples were infiltrated with

Durcupan ACM resin (Sigma-Aldrich), and blocks were polymerized at 60 ^{o}C. Ultrimicrotomy was performed using an UC7 ultramicrotome (Leica).

For CQ treatment, cells were infected as described above with MHV-A59 at m.o.i. 10. At 7 hpi, 5 µl of cell media was removed and replaced by a 20 mM solution of chloroquine diphosphate (Sigma-Aldrich) in DI water. The total CQ concentration was 100 µM. After 5 hours of CQ treatment, cells were cryofixed at 12 hpi and processed for EM.

2.2.4 Electron microscopy of thin sections

Thin sections (90 nm) were used for screening and quantitative analysis of cell cross sections in 2D. Sections were collected on formvar-coated copper slot grids and contrasted with 2% aqueous uranyl acetate and Sato's lead. Imaging was performed on a Philips CM-100 microscope operating at 100 kV or a Tecnai T12 microscope operating at 80 kV, both equipped with a Gatan Orius CCD camera. For quantitative analysis, 25 cross sections of infected cells were imaged. For each infected cell, a series of overlapping images were collected covering the entire cell cross section at a magnification high enough to identify DMVs and virus particles. Images were montaged together using the MosiacJ plugin of ImageJ[194], and the montage of each cell was imported into IMOD[195]. The plasma membrane and nucleus were hand traced as single contours, and the locations of DMVs and virus particles were marked using point objects. Cytoplasmic area was determined by subtracting the area inside the nuclear trace from the area inside the plasma membrane trace. DMV density was determined as the number of DMVs counted per μm^2 of cytoplasmic area. Statistical significance between groups was determined using the Wilcoxen rank sum test.

2.2.5 Large volume electron tomography

Serial sections of 250 nm thickness were collected on LUXFilm coated 2 x 1 mm copper slot grids (Luxel). Sections were contrasted with 2% aqueous uranyl acetate and Sato's lead before carbon coating and overlaying with 10-nm colloidal gold particles (Sigma) for use as fiducial markers. Grids were screened on the Philips CM100 or Tecnai T12 microscope for representative cells. LVT were collected using a Titan Krios TEM (FEI) operating at 300 kV at room temperature. Tilt

series were collected with automation using SerialEM[196]. First, a low magnification image montage of the entire grid was created to use as a map for marking regions of interest. The area of interest in a cell was visualized and marked on consecutive serial sections. At each section, a tilt series was collected. For each tilt series, images were collected at tilts from + 60 to - 60 degrees in 2 degree increments. To increase the area imaged, a 2x2 image montage was collected at each tilt. The datasets for the 7 hpi and 12 hpi timepoints were collected on different cameras due to the replacement of the CCD camera with a direct electron detector by the Purdue Cryo-EM facility between the collections of the two datasets. Every effort was made to collect as similar datasets as possible; however, differences in image size and collection parameters, as well as reconstruction, were unavoidable, and are described below.

The 7 hpi dataset was collected using a 4k x 4k pixel UltraScan 4000 CCD camera (Gatan). Montage images were collected at a magnification corresponding to 1 nm/pixel at the specimen level. Final image dimensions were 7800 x 7800 pixels due to the 200 pixel overlap of the montage. Eight serial sections of a region of a cell were imaged. Images were aligned using cubic interpolation and tomograms reconstructed by weighted back projection using IMOD.

The 12 hpi dataset was collected on the K2 direct electron detector (Gatan) operating in linear mode at 95% of the maximum dose rate. Montage images were collected at a magnification corresponding to 0.8 nm/pixel at the specimen level. Final image dimensions were 7296 x 7040 pixels. Five serial sections of a region of a cell were imaged. Images were binned by 2 and aligned using linear interpolation. Reconstruction of tomograms was done in IMOD using 30 iterations of SIRT.

For each dataset, serial tomograms were aligned and joined in z to produce reconstructed volumes with dimensions 7.8 x 7.8 x 2 µm (7 hpi) and 5.8 x 5.6 x 1.25 µm (12 hpi). DMVs were segmented by hand tracing using IMOD's Drawing Tools and Interpolator, and 3D surface models were generated by meshing. Virus particles and budding virus were approximated by placing a sphere with a radius corresponding to a diameter of 90 nm at the center of each virus particle density. The ER and Golgi were segmented via semi-automated methods using Microscopy Image Browser[197]. A combination of watershed segmentation using superpixels and the "Membrane

Clicker" tool were used to delineate membranes of interest. Model data was transferred into IMOD, smoothed and meshed to produce 3D models.

2.3 Results

2.3.1 Characterization of RVN and ER changes through the course of MHV infection

To establish a broad view of virus-related structures through the course of infection, confocal microscopy was performed on MHV-infected 17Cl-1 cells at timepoints between 4 and 16 hours post infection (hpi). To monitor the development of the replication-associated RVN, MHV strain A59 expressing GFP as a fusion with nsp3 (MHV-Δ2-GFP3[190]) was utilized. Nsp3 is one of three nonstructural proteins most directly involved in producing RVN-like membrane rearrangements, specifically through membrane pairing and proliferation[78]. Faint punctate fluorescence was observed at 4 hpi, located perinuclearly. Over time, the number of puncta as well as the fluorescence signal increased, with extensive RVN formation visible by 7 hpi (Figure 2.1A). Nsp3 puncta did not appreciably coincide with the ER marker calreticulin. The ER itself appeared web-like and morphologically typical despite the presence of the RVN (Figure 2.1A). As infection progressed, infected cells were increasingly present as multi-nucleate syncytia (Figure 2.1A, 12 hpi). Syncytia formation is initiated by expression of the S (spike) glycoprotein on the cell surface, which allows infected cells to fuse with one other[198]. By 12 hpi, nearly all infected cells were present in syncytia and the punctate fluorescence of the RVN had increased in intensity (Figure 2.1A). The RVN remained distinct from the ER throughout infection. At 12 hpi and beyond, brighter globular regions of ER were observed in addition to the typical ER structure (Figure 2.1B, 12 hpi). These regions colocalized with viral M protein, the major membrane glycoprotein of MHV particles[199]. The presence of virus particles in the ER was only observed late in infection. At earlier timepoints, M protein showed strong Golgi localization (Figure 2.1B and Figure 2.2).

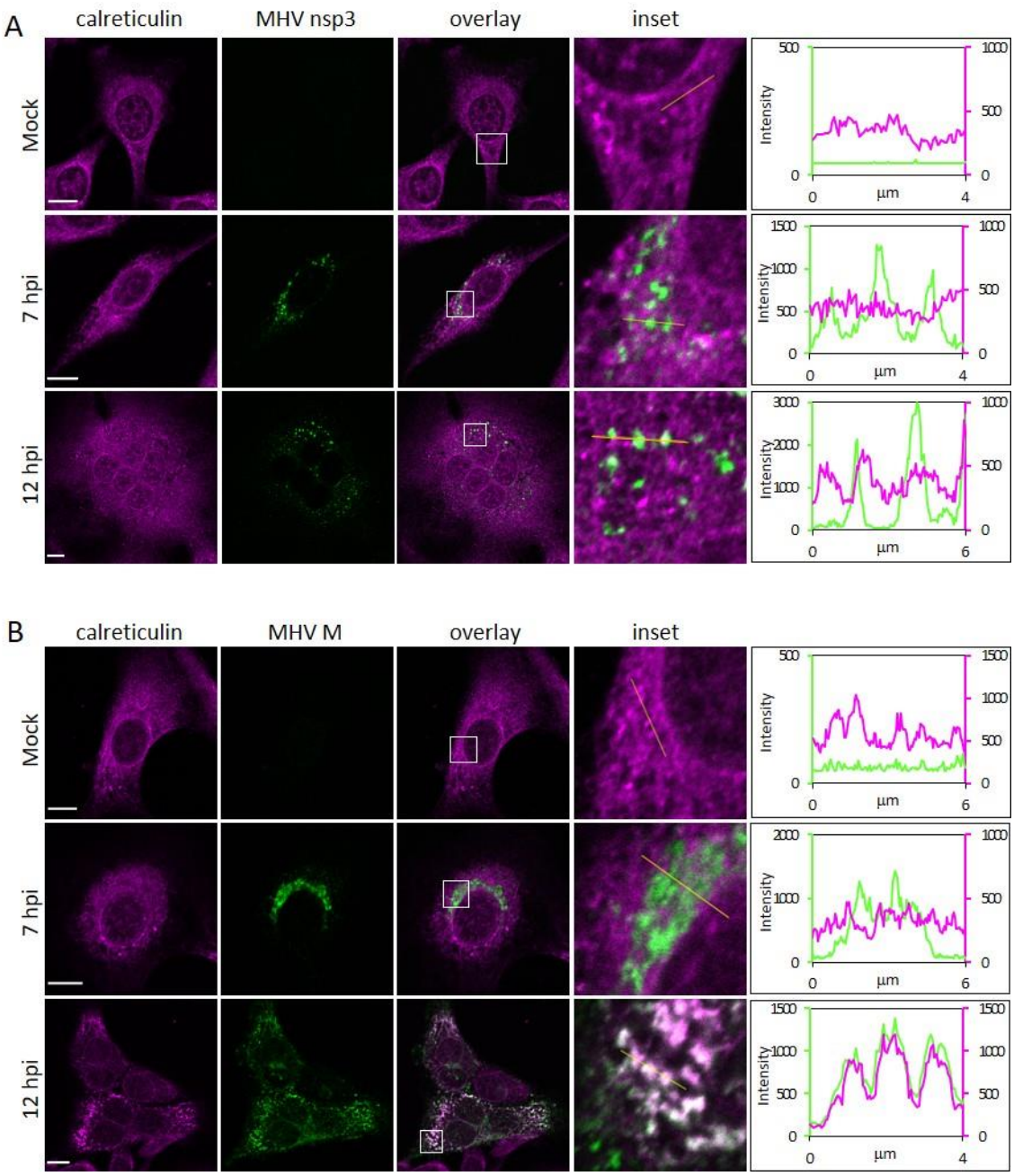

Figure 2.1. Visualization of MHV proteins and the ER through the course of MHV infection. **(A)** 17Cl-1 cells were mock infected or infected with MHV-Δ2-GFP3 at an m.o.i. of 0.1, fixed at various timepoints, and processed for immunofluorescence detection of calreticulin as an ER marker. Nsp3 puncta remain independent from the ER throughout infection. At 12 hpi, cells are present as multi-nucleate syncytia and the ER exhibits increased punctation. **(B)** 17Cl-1 cells were mock infected or infected with MHV-A59, fixed at various timepoints, and processed for dual-labeled immunofluorescence detection of viral M protein and calreticulin. At 7hpi, M is mostly confined to the Golgi (see also Figure 2.2). At 12 hpi, M and calreticulin have a high degree of colocalization in certain larger punctate regions. **Scale bars:** 10 µm.

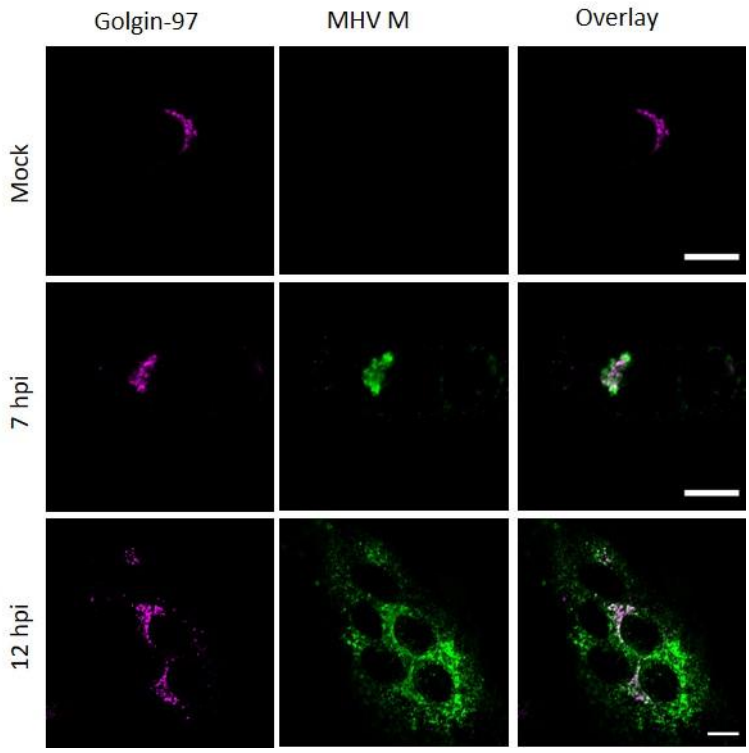

Figure 2.2. Colocalization of MHV M protein with Golgi through the course of MHV infection. 17Cl-1 cells were mock infected or infected with MHV-A59, fixed at various timepoints, and processed for dual-labeled immunofluorescence detection of viral M protein and Golgin-97. **Scale bars:** 10 μm.

Based on the confocal data, samples were prepared for thin section electron microcopy through the same range of infection timepoints (4, 7, 10, 12, and 16 hpi). At 4 hpi, most cell cross-sections showed no signs of infection, but individual DMVs or small DMV clusters were occasionally observed (Figure 2.3A-C). A distinct inner density was visualized in DMVs (Figure 2.3B-C) which we attribute to sample preparation by cryofixation and freeze substitution. In the literature to date, CoV DMVs appear empty unless prepared by these methods[27], [28], [40], [41], [98], [99], [200]. Excellent preservation and staining of the double bilayer (Figure 2.3C arrowhead) and other organelles was also achieved by these methods. At 7 hpi, the most apparent change from 4 hpi was the large number of DMVs present in many cells (Figure 2.3D-E). Additionally, virus particles (VP) were occasionally observed in Golgi cisternae and small membrane-bound compartments (Figure 2.3F arrowheads). Overall, the number of DMVs and virus particles increased up to 10 hpi, consistent with the quantitative analysis by Ulasli, et al[41]. By 12 hpi, VP were present in large numbers in the ER lumen (Figure 2.3G-I) and assembling on the ER membrane (Fig. 2I arrowheads), while the RVN was present but less apparent (Figure 2.3H

arrowheads). At 16 hpi, the major characteristic of infected cells remained the ubiquitous presence of VP inside the ER; however, cells were fragile due to the advanced infection.

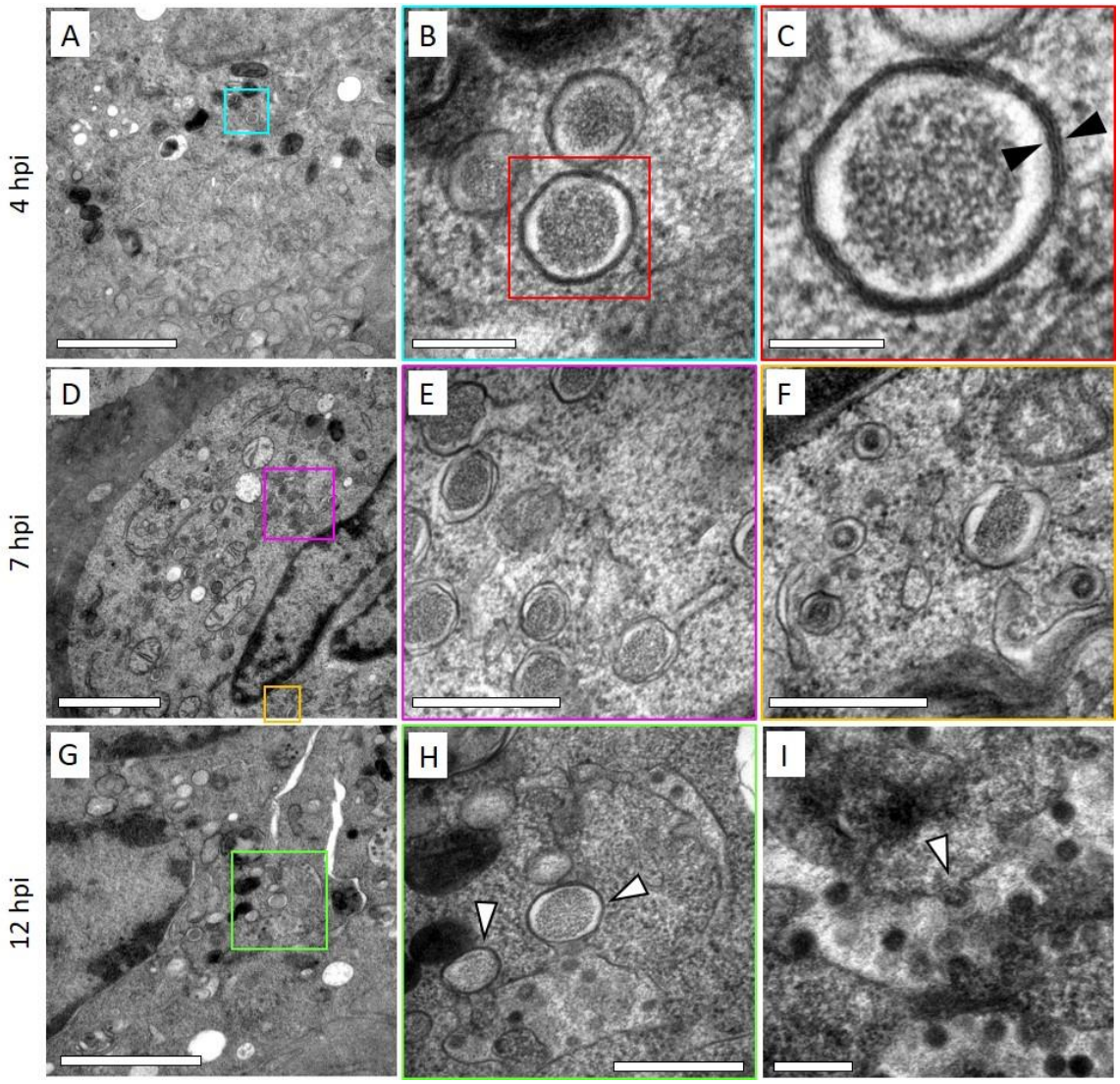

Figure 2.3. Observations of thin sections from three timepoints during MHV infection. 17Cl-1 cells were infected with MHV-A59 at an m.o.i. of 10 for the stated times, followed by HPF and FS. Images are from 90-nm sections. **(A-C)** Early in infection (4 hpi), perinuclear DMVs and small clusters of DMVs are occasionally observed. Note the preservation of DMVs including the interior density as well as a double bilayer identified by three layers of stain (arrowhead in C). **(D-F)** At 7 hpi, large numbers of DMVs are observed throughout the cytoplasm, and enveloped virus particles in small vesicular structures is occasionally observed (arrowheads in F). **(G-I)** Late in infection (12 hpi), in addition to DMVs, virus particles are observed extensively in the ER lumen, including assembling particles on the cytoplasmic side of the ER (arrowhead in I). **Scale bars:** 2 µm (A, D, G), 200 nm (B, I), 100 nm (C), and 500 nm (E, F, H).

2.3.2 Collection of LVT and 3D characterization of RVN structures

Based on the confocal and ultrastructural time course analysis, we chose 7 hpi and 12 hpi as timepoints for further investigation into RVN structure, changes, and interaction with the ER over time. At 7 hpi, we observed extensive RVN, and the rate of RVN formation is expected to be high[41]. Therefore we planned to use this timepoint to analyze RVN large-scale morphology, ER morphology changes in response to RVN formation, and look for evidence of DMV biogenesis. At 12 hpi, we observed extensive virus assembly in the ER, and we planned to explore how that late-stage assembly affects the RVN and determine how extensive ER assembly is. In order to address these questions we collected serial-section large volume tomograms (LVT) of MHV-A59-infected 17Cl-1 cells cryofixed at 7 hpi and 12 hpi.

For the 7 hpi timepoint, we identified a cell which showed representative characteristics of the timepoint through several serial sections. The cellular area chosen included large numbers of DMVs, ER, and some VP. The area spanned the nucleus and the plasma membrane. A TEM image of one 250-nm section of the 7 hpi cell is shown in Figure 2.4A with the area of collection outlined. A LVT was produced by a tilt series acquisition combining montaged imaging at each tilt with collection of tomograms on serial sections. The final tomogram volume had dimensions of approximately 8 x 8 x 2 μm (Figure 2.4B). Montaging and serial sectioning allowed the volume of the LVT to be approximately 32 times the volume of a single tomogram collected at this magnification.

First, to morphologically describe the RVN, we analyzed the structure of DMVs and CM. A total of 659 DMVs were identified within the volume, defined as approximately spherical vesicles with an outer double bilayer, electron lucent layer, and a distinct inner density (Figure 2.4C-D). A representative DMV was modeled by segmentation of the membranes and a threshholded isosurface of the inner density (Figure 2.4D). Each DMV was segmented and its volume calculated. DMV volumes formed a unimodal distribution ranging from 1.4×10^5 nm^3 to 2.0×10^7 nm^3, equivalent to a diameter range of 64 to 334 nm, assuming spherical morphology. The mean DMV size was 6.5×10^6 nm^3 (225 nm diameter) (Figure 2.4E). Altogether, DMVs occupied 4.4 μm^3, approximately 3.4% of the 128 μm^3 tomogram volume. DMVs had membranous connections with CM, ER, and other DMVs. CM were identified as densely curved membranes, often with DMVs

surrounding and connected to them (Figure 2.4F-G). Close examination of the CM structure on 2-nm thick virtual slices revealed short stretches of paired membrane which were difficult to trace in subsequent slices due to the high curvature (Figure 2.4H arrowheads). An attempt at modeling the CM was achieved by tracing short double membrane segments on each slice using a tube (represented in IMOD as spheres). No regularly occurring pattern was visible in the 3D structure, but the highly curved, densely packed nature of the CM membranes was further established. A clear connection between the CM and ER and three DMVs was established for this CM (Figure 2.4I).

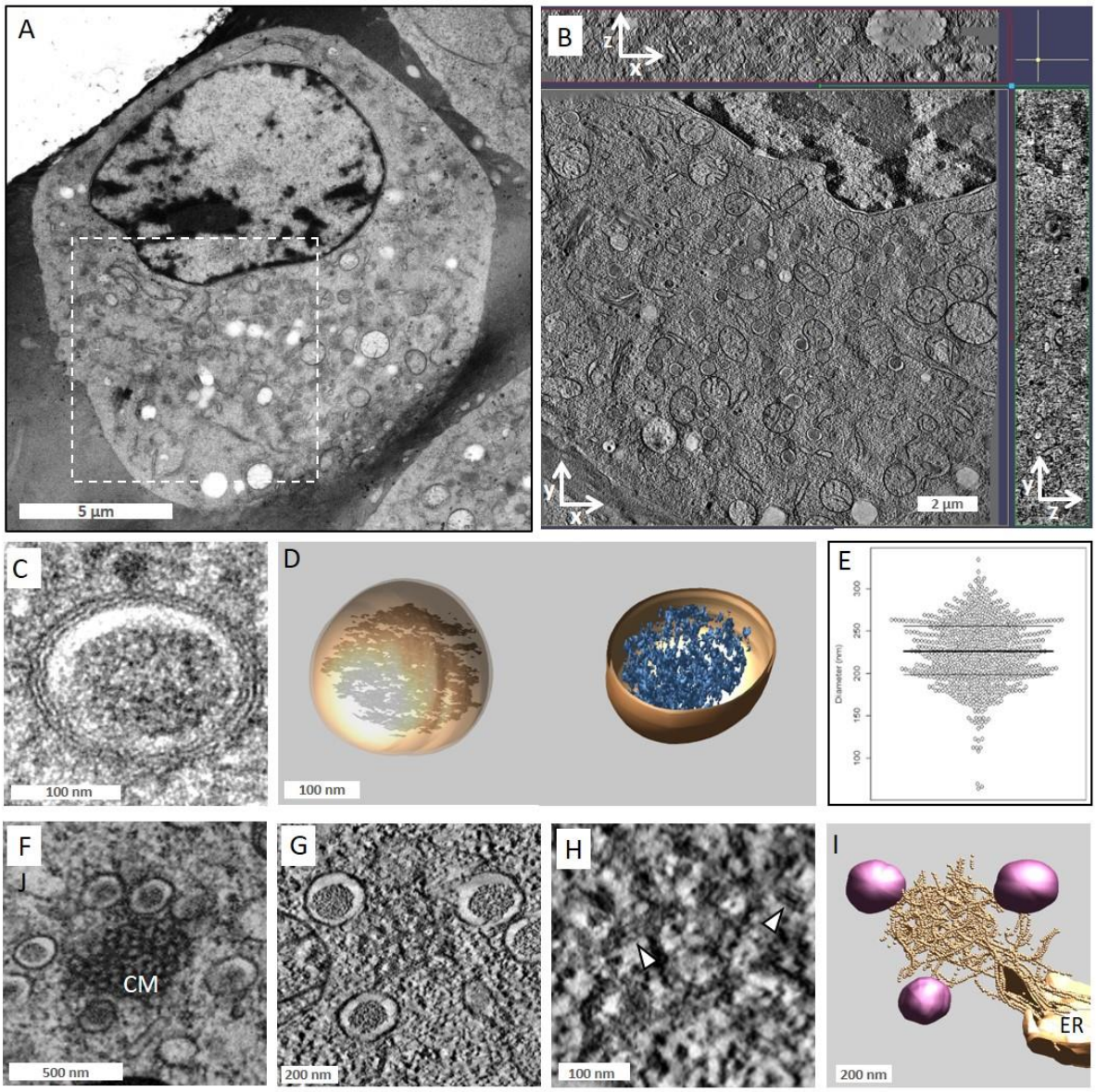

Figure 2.4. Large volume tomography of an MHV-infected 17Cl-1 cell at 7 hpi. **(A)** TEM image of a 250-nm section collected on the Titan Krios at 300 kV. The cell used for LVT is shown with the outline of the approximate area for the tomogram collection. **(B)** Slices through the reconstructed LVT with the z-depth along the x and y axis shown along the top and right side, respectively. **(C)** TEM image of a 90-nm section of a DMV, clearly illustrating the double membrane, electron lucent ring, and electron dense core. **(D)** 3D visualization of a DMV from the LVT, with outer membrane (dark brown), tightly apposed inner membrane (light brown) and threshholded density of the inner core. **(E)** Plot of the distribution of DMV diameters calculated from segmented volumes. Thin lines represent the first and third quartile, and the thick line represents the mean value. **(F)** A TEM image of a 90-nm section containing convoluted membrane (CM) surrounded by DMVs. The section thickness allows the web-like structure to be observed. **(G)** A 2-nm tomogram slice of CM with paired membrane nature shown in the higher magnification image in **(H)**. **(I)** Segmenting the CM was attempted by drawing tubes (consisting of a series of spheres) along visible membrane segments on each slice. The membranes are continuous with DMV outer membranes as well as the ER.

2.3.3 The RVN at 7 hpi is an interconnected network of DMVs which bud from the ER

In order to further describe the RVN and look for clues to RVN formation, we next examined the connections within the RVN. Because DMVs are believed to originate from the ER, we began with the DMVs most directly connected to the ER. Some DMVs had their outer membrane clearly continuous with the ER such that the inner DMV membrane contacted the lumen of the ER (Figure 2.5A). These DMVs appeared to be fully enclosed vesicles budding out of ER cisterna to obtain their second membrane (Figure 2.5A). They were observed budding from the face of cisternae (Figure 2.5Aiv black arrowhead) and cisternal edges (Figure 2.5Aiv, white arrowhead). Budding DMVs accounted for 126 of the 659 DMVs (19.1%). They were located throughout the imaged volume and were not found preferentially in any region of the cell or ER. Interestingly, no single membrane vesicles were observed in the ER lumen which appeared to represent earlier steps in DMV formation.

A second category of DMVs also had outer membranes continuous with the ER; however, the membranes were pinched together to form a small paired region at the point of contact (Figure 2.5B, especially Bii-arrowhead). Similar pinching connections were observed between two DMVs and between DMVs and CM (Figure 2.5C). Altogether, 173 DMVs (26.2%) had pinching connections with ER, CM, or DMVs. A small number of DMVs (21, 3.2%) had two inner vesicles within a shared outer membrane, referred to as twins (Figure 2.5D). Nearly one-third of DMVs had two or more connections to the RVN, with DMVs having up to six total connections. In addition to contacting ER and RVN structures, 46 DMVs (7%) had outer membranes which contacted other organelle membranes including mitochondria and endo-lysosomal vesicles. Surprisingly, 126 DMVs (19%) had no visible connections to the ER, RVN or any other membrane, and thus were called “free” DMVs. This is the first observation of free DMVs in CoV infection. An example is given showing nine virtual slices spaced at 20-nm intervals (Figure 2.5E-F). No membrane structure comes within approximately 50 nm of the DMV in x, y, or z directions. The 3D view in Figure 2.5G shows segmentation of the closest nearby structures, including the ER, a DMV, a microtubule, and two mitochondria. The full tabulation of DMV connections is provided in Table 2.1.

Altogether, this analysis of the RVN at 7 hpi reveals that DMVs have various degrees of connection to the ER, ranging from the entire outer membrane being continuous, to a large class of DMVs with no connections at all. These observations provide visual evidence of the morphologically earliest form of a DMV and ideas about formation by budding of the 2nd membrane. The presence of free DMVs opens up the possibility that DMVs are trafficked through the cell individually.

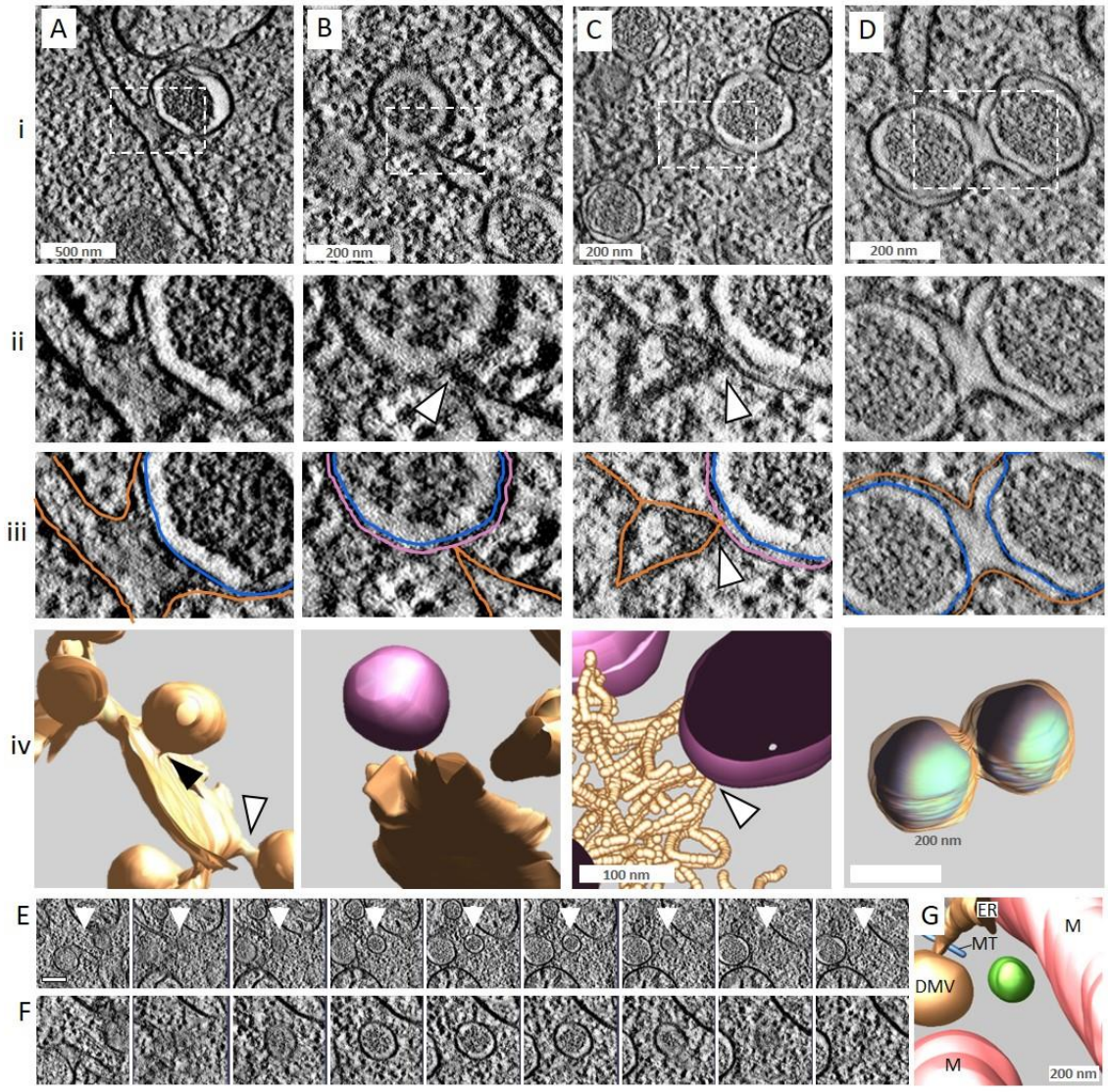

Figure 2.5. LVT analysis of the RVN at 7 hpi. **(A-D)** Representative examples of the commonly observed membrane connections with DMVs, including budding DMVs with outer membrane continuous with the ER (A), Pinching DMV contacting the ER (B) or CM (C), and a DMV "twin" consisting of two inner vesicles which share an outer membrane (D). **(E-F)** Serial tomogram slices with 20 nm spacing, illustrating the ability to detect DMVs which are not connected to any other membranes or organelles. Scale bar: 200 nm. **(G)** 3D model of the DMV shown in E-F in green, showing clear 3D separation from the nearest surrounding structures, including the labeled DMV, ER, mitochondria (M) and microtubule (MT).

Table 2.1. Categorization of DMV connections from the 7 hpi large volume tomogram

Category			Number	% of total
All DMVs			659	100
	Free		126	19.1
	Connected		533	80.9
		Single connection	320	48.6
		Budding - ER	126	19.1
		Pinching - ER	78	11.8
		Pinching - CM	41	6.2
		Pinching - DMV	54	8.2
		DMV “twin”	21	3.2
		Multiple connections	213	32.3
		2	165	25.0
		3	38	5.8
		4	8	1.2
		5	1	0.2
		6	1	0.2

2.3.4 ER in MHV-infected cells is remodeled by membrane pairing and budding DMVs

While the RVN represents an extensive addition to and remodeling of the ER, we observe areas of morphologically typical ER, so we examined the endogenous ER specifically for changes. The rough ER from approximately half of the LVT was segmented using semi-automated methods, and a 3D model was produced (Figure 2.6A-C). The ER of the infected cell exhibited largely typical continuous, cisternal morphology; however, as reflected in the 3D view, many budding DMVs were observed on the faces and edges of cisternae (Figure 2.6C arrowhead and Figure 2.5Div arrowheads). Another infection-induced change in the ER was the presence of paired membranes, including large cisternal regions with no detectible luminal space (Figure 2.6D-G). Overall, much of the morphology of the cisternal ER was preserved at 7 hr post infection, despite the plentiful budding of DMVs of relatively large size. The extensive RVN thus seems to form from and remain mostly distinct from the endogenous ER.

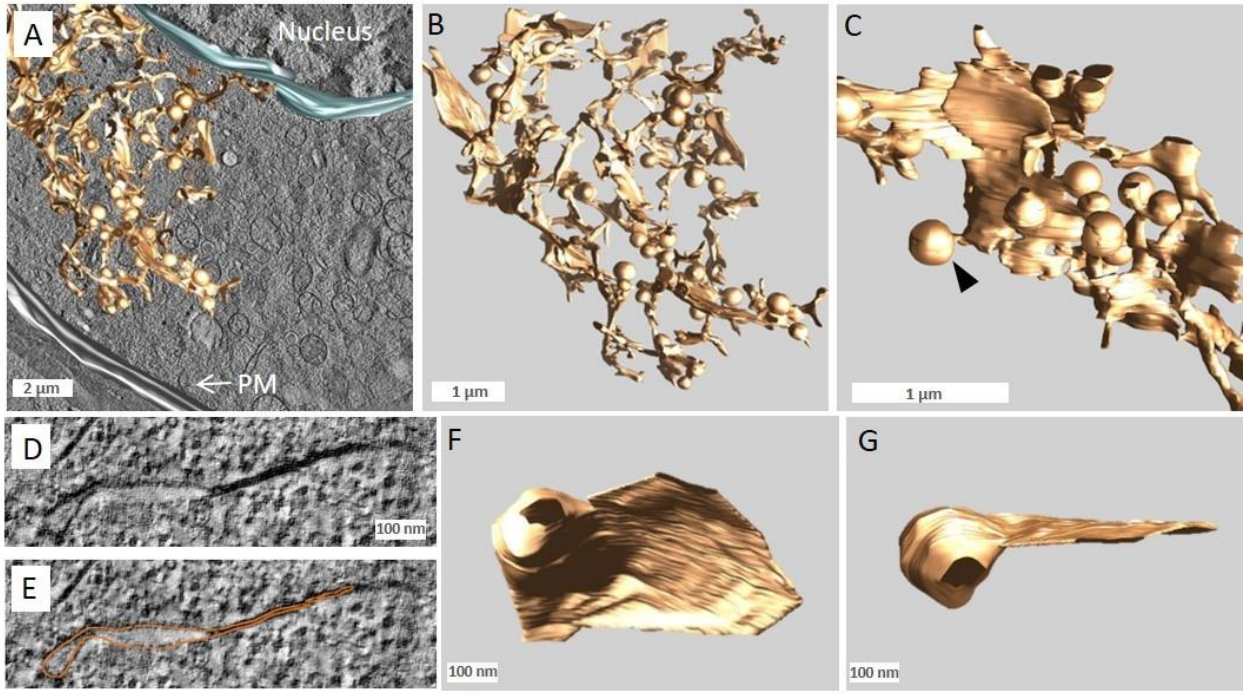

Figure 2.6. ER remodeling at 7 hpi **(A-B)** 3D model of the ER produced by segmentation of approximately half the ER volume from the LVT. **(C)** A region of ER which illustrates the cisternal ER as well as DMVs with outer membranes continuous with the ER membrane (arrowhead). **(D)** Tomogram slice showing a region of cisternal paired ER, with segmentation trace shown in **(E)**. **(F-G)** 3D models of the paired cisternal ER from (D).

2.3.5 ER structure is disrupted late in infection by virus assembly

After establishing the morphological characteristics of the RVN and ER at 7 hpi, near peak replication in the virus infection, we performed similar analysis at a late stage in infection, when the ER has obtained a new role as a membrane source for newly forming VP. It was unknown how this new role affects the RVN or ER morphology. To address this, we collected an LVT from an MHV-A59-infected 17Cl-1 cell fixed at 12 hpi. A representative cell syncytium from this timepoint was selected, and a region of the cell was chosen which contained extensive areas of ER and RVN, showed VP in the ER lumen, and encompassed the nucleus and plasma membrane (Figure 2.7A-B). A representative portion of the ER was segmented and visualized in 3D (Figure 2.7C-E). While at 7 hpi, the ER maintained its cisternal morphology (Figure 2.6A-C), at 12 hpi, the ER was swollen and globular and filled with VP (Figure 2.7D). The globular regions were smaller than entire cisternae indicating that the cisternae are not only expanded to accommodate lumenal VP, but the cisternae are broken into smaller compartments as well (Figure 2.7E). VPs

were present in all regions of the ER lumen ranging from the outer nuclear membrane to the periphery of the cell (Figure 2.7F). New VP were frequently observed assembling on the cytoplasmic surface of the modified ER and budding into the ER lumen (Figure 2.7G-I, arrowheads).

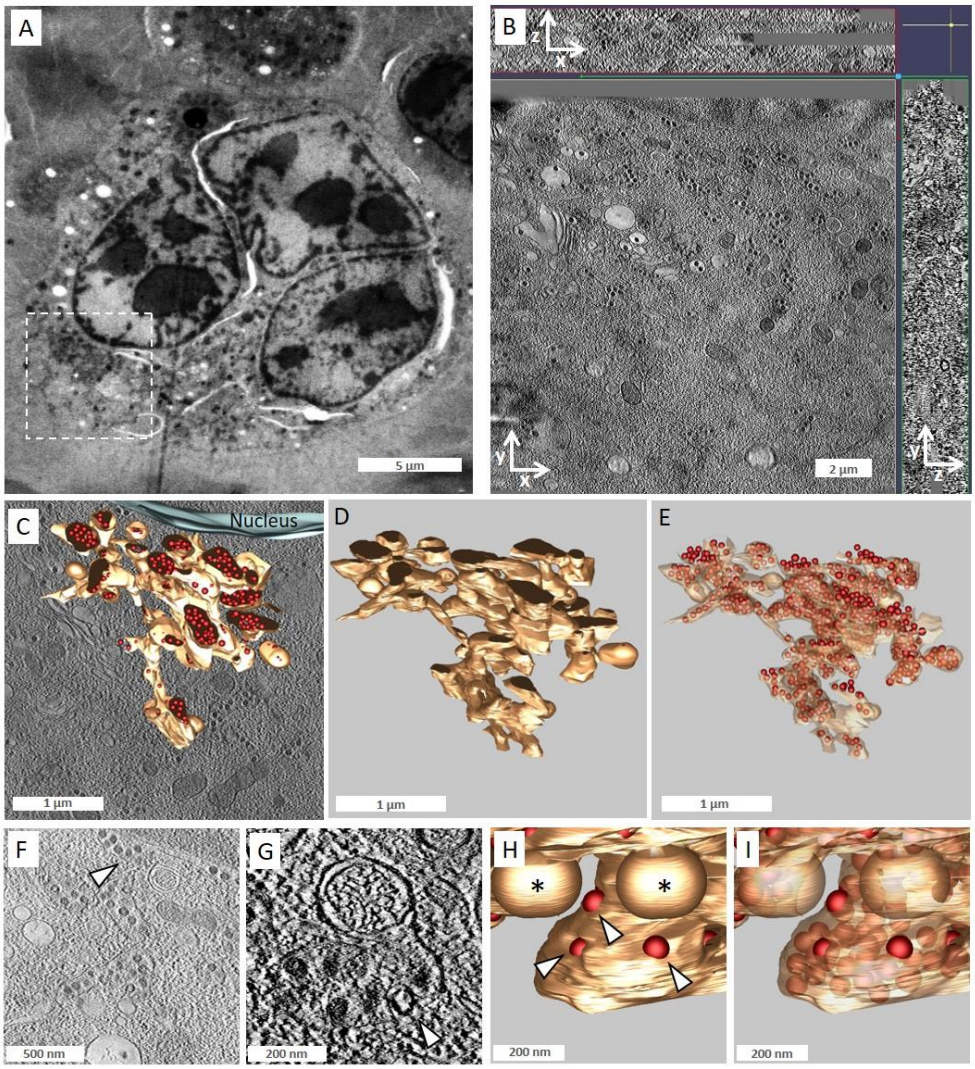

Figure 2.7. ER morphology changes late in infection. **(A)** TEM image of a 250-nm section collected on the Titan Krios at 300 kV. MHV infected 17Cl-1 cells were fixed at 12 hpi and processed for ET. The cell (syncytium) chosen for LVT is shown along with the outline of the approximate area for the tomogram collection. **(B)** Slices through the reconstructed LVT with the z-depth along the x and y axis shown along the top and right side, respectively. **(C)** 3D model of a segmented portion of ER with enveloped VP (red), superimposed on a slice from the tomogram. **(D)** View of the globular ER structure without the virus particles. **(E)** Transparent view of the ER displaying the dense packing of VP within its lumen. **(F)** A tomogram slice demonstrating the presence of VP in the ER, including the nuclear envelope (arrowhead) and globular regions of ER. **(G)** Tomogram slice showing a region of ER with a budding DMV and inner budded VP as well as an assembling VP (arrowhead). **(H-I)** 3D model views of the region of ER shown in (G) with budding DMVs (asterisks) along with assembling VP (arrowheads).

2.3.6 The RVN is broken down late in infection

In addition to changes in the ER, distinct changes in the RVN were observed between 7 and 12 hpi. No CM were present in the 12 hpi volume. DMVs were segmented and their number, size and connections were analyzed as previously. The number of DMVs decreased prominently from the 7 hpi to the 12 hpi LVT. At the earlier timepoint, 5 DMVs were present per cubic micron of the LVT, while at the late timepoint, only 0.7 DMVs/μm^3 were present. In both LVTs, DMVs were distributed throughout the ER and cellular volume (Figure 2.8A-B). The types of connections within the RVN also changed over time, most notably free DMVs increasing from 19.1% to 46.9% of the total (Figure 2.8C and Table 2.2). Additionally, DMVs with multiple connections decreased from 32% to 6% of the total, and at 12 hpi no DMVs with more than 2 connections were observed. Thus, between 7 and 12 hpi, the RVN breaks down in terms of number of DMVs, their connections, and loss of the CM structure. Although every effort was made to choose representative areas of the cells for LVT collection, it was necessary to verify this RVN breakdown using a statistically relevant sample of thin sections. For each timepoint, DMV profiles from 25 cells were counted and cytoplasmic areas of the cells were calculated. From 7 to 12 hpi, the number of DMVs per cytoplasmic area decreased from 0.47 DMV/μm^2 to 0.24 DMV/μm^2 ($p = 0.009$). This verification of the RVN breakdown provides further evidence that the RVN is a more dynamic structure than previously believed.

Table 2.2. Categorization of DMV connections from the 12 hpi large volume tomogram

Category	Number	% of total
All DMVs	32	100
Free	15	46.9
Connected	17	53.1
Single connection	15	46.9
Budding - ER	8	25.0
Pinching - ER	7	21.9
Pinching - CM	0	0
Pinching - DMV	0	0
DMV “twin”	0	0
Multiple connections	2	6.3
2	2	6.3

2.3.7 DMVs are trafficked to lysosomes for degradation

In order to investigate RVN breakdown, we next looked at host cell involvement in CoV infection. It has previously been shown that CoV DMVs contain cellular markers for ER-associated degradation (ERAD) tuning, namely EDEM-1, OS-9, and LC3-I[109]. The vesicles involved in ERAD tuning are single membrane vesicles which bud from the ER and are rapidly trafficked to lysosomes for degradation[114]–[116]. Therefore, we hypothesized that ERAD tuning could play a role in the breakdown of the RVN. Because of the unique morphological characteristics of the DMV, we examined thin sections and the LVTs for visual evidence for lysosomal degradation of DMVs. We observed several examples of potential fusion events between a DMV and lysosome (Figure 2.8D-E), as well as DMV-like objects present within lysosomes (Figure 2.8F-G). Two potential mechanisms were also observed: both bilayers may fuse with the lysosomal membrane (Figure 2.8E arrowheads), or the outer membrane alone may fuse leaving a single membrane vesicle inside the lysosome (Figure 2.8G). DMVs were also observed associated with microtubules as would be expected of trafficking. The microtubule dependence of DMV movement has already been established; however, the interpretation was that DMVs were trafficking toward the RVN rather than away from it[103]. In the 7 hpi volume, 15% of DMVs were located within 50 nm of a microtubule, and evidence of potential connections were observed (Figure 2.8H-J).

To further test the hypothesis that CoV DMVs are degraded by ERAD tuning, the fusion of vesicles with lysosomes was blocked using chloroquine (CQ). CQ inhibits turnover of ERAD tuning proteins[116]. 17Cl-1 cells were infected with MHV-A59 and the infection was allowed to proceed for 7 hours in order to allow the RVN to form. At 7 hpi, CQ was added to a final concentration of 100 μM. At 12 hpi, cells were cryofixed and processed for EM. DMV numbers from 25 cell cross sections were compared to data from untreated cells at 7 hpi and 12 hpi. In untreated cells, the number of DMV/μm^2 decreased from 0.47 to 0.24 from 7 to 12 hpi. CQ treated cells at 12 hpi contained 0.64 DMV/μm^2, nearly three times the number of DMVs present without treatment ($p=0.001$, Figure 2.8K). Together these results reveal that trafficking of DMVs to lysosomes for degradation contributes to the breakdown of the RVN late in CoV infection.

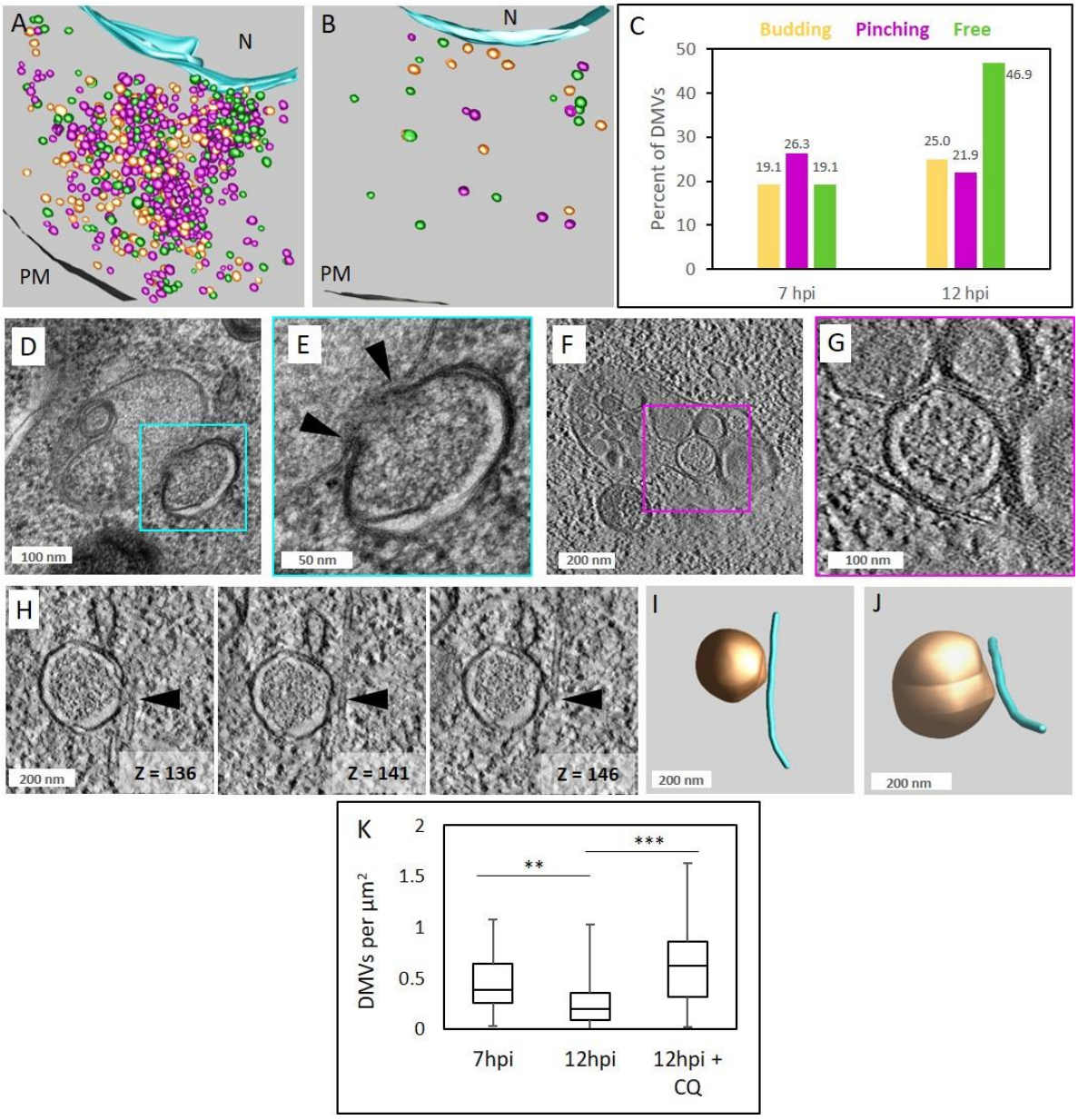

Figure 2.8. The RVN is broken down late in infection and DMVs are trafficked to lysosomes. **(A-C)** Overview of the segmented DMVs present at 7 hpi (A) and 12 hpi (B) which are color-coded based on their classification as budding (yellow), pinching (magenta) or free (green). The nucleus (N) is shown in blue and the plasma membrane (PM) in grey. The proportion of DMVs in each of the classifications is shown graphically in (C). Only DMVs with single connections or no connections were included. **(D-E)** Thin section TEM images of a DMV fusing with a lysosome. Both membranes appear to be merging with the lysosomal membrane at two distinct points indicated by arrowheads in E. **(F-G)** Tomogram slices showing a single-membrane vesicle with otherwise DMV-like morphology present within a lysosomal compartment. **(H)** Tomogram slices at various z-heights showing a DMV with a microtubule trajectory nearby. **(I-J)** 3D model of the DMV and microtubule in H. **(K)** Box plot comparing number of DMVs per cytoplasmic area of the cell from a population of 50 cells for each group. Cells in the "12 hpi +CQ" group were treated with 100 µm chloroquine for the last 5 hours of infection. Statistical significance was determined using the Wilcoxen rank sum test. **, $p \leq 0.01$. ***, $p \leq 0.001$.

2.3.8 The MHV budding compartment shifts through the course of infection

After observing the major changes that occur in the ER and RVN late in infection, we next examined the concurrent changes occurring in virus assembly. Earlier in this study, we established that the M protein localizes with the Golgi early in infection, and late in infection becomes distributed throughout the cell, including partial colocalization with the ER (Figure 2.1B and Figure 2.2). In the LVTs, four distinct membrane structures containing VPs were observed at both timepoints. Rough ER (Figure 2.9A) and Golgi cisternae (Figure 2.9B) were easily identifiable by morphology. VP were also found in the lumen of small smooth vesicles assumed to be ERGIC (Figure 2.9C) [101], [183]. Larger electron-lucent vesicles often containing many VP and other structures of varying morphology were also observed (Figure 2.9D) [41]. VP were mostly found fully enveloped in the lumen of organelles, while a small proportion were in the process of assembly and/or budding (Figure 2.7G-H). The organelle association of each VP in the two LVTs was tabulated. In the 7 hpi volume, a total of 391 VPs were identified (3.1 VP/μm^3). The majority of VP (70%) were located in small vesicles (ERGIC), 15% in the Golgi, 12% in large vesicles, and 2% in the rough ER (Figure 2.9E and G). In the 12 hpi LVT, 3202 virus particles were present (59.3 VP/μm^3), a nearly 20-fold increase in density from the earlier timepoint. The majority of VP were in the lumen of the ER (89%), followed by the Golgi (5%), small vesicles (4.5%), and large vesicles (1%) (Figure 2.9F-G). These numbers show that the period of MHV infection between 7 and 12 hpi involves a surge in VP assembly and envelopment, largely taking place on ER membranes. Overall, the Golgi and large vesicles are minor membrane sources for MHV envelopment throughout infection. The major budding compartment shifts from the ERGIC to the ER as infection progresses. This dynamic use of organelles for virus assembly occurs concurrently with the shift from formation of replication-associated DMVs to the degradation of the RVN.

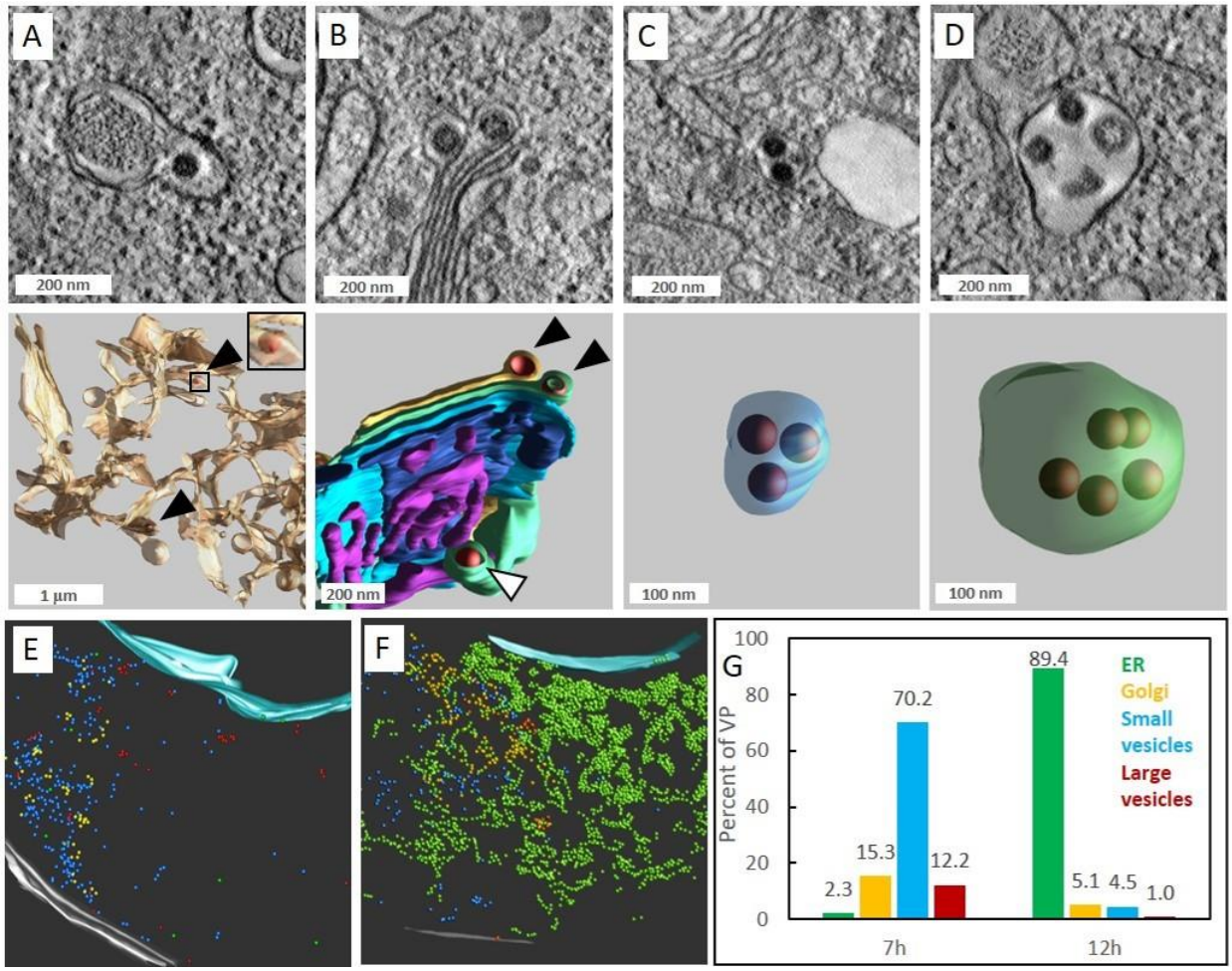

Figure 2.9. Analysis of the virus budding compartment through the course of MHV infection. LVT from both 7 hpi and 12 hpi reveal enveloped VP within the interior of rough ER **(A)**, Golgi **(B)**, small vesicles **(C)** and larger electron lucent vacuoles **(D)**. The location of each VP within the 7 hpi volume **(E)** and the 12 hpi volume **(F)** is indicated, color-coded based on the compartment in which they are found: ER (green), Golgi (yellow), small vesicles (blue) and large vacuoles (red). **(G)** Comparison of the percentage of VP in each group at the two timepoints.

2.4 Discussion

In this work, we provide a comprehensive 3D ultrastructural analysis of the coronavirus RVN as well as a new perspective on its dynamic nature throughout infection. Utilizing large volume electron tomography, we first characterized the RVN as a vast network of DMVs, CMs, and ER which accumulates throughout infection and is broken down late in infection. We described the morphological changes in the ER as well. We provide evidence that DMVs are not static structures, but have a life-cycle consisting of budding from the ER and trafficking to lysosomes for degradation. Finally, we show that in addition to the changing nature of the RVN, virus assembly

takes place preferentially in the ERGIC early in infection and the ER late in infection. Taken together, these analyses provide a broader view on the interaction of a coronavirus with its host cell organelles.

One long-standing question about CoV DMVs is the morphology of their formation. In this study we maximized our chances of observing formation intermediates by collecting a volume with nearly 700 DMVs at a timepoint where the DMV formation rate is expected to be at its maximum[41]. Although we observed large cisternal areas of paired ER, we found no evidence that paired regions wrap around to form DMVs, as in the biogenesis of autophagosomes[201], [202] and DMVs from the Arterivirus Equine Arteritis Virus (EAV)[30]. The earliest stage of DMV observed was DMVs with fully formed inner vesicles, budding out from the ER to obtain their second bilayer. We found no morphological evidence of formation of the inner vesicle or accumulation of the inner density, indicating that the early steps in DMV biogenesis may be a rapid process. In contrast, budding intermediates for ERAD tuning vesicles have been captured by EM, and thus ERAD tuning may govern the second, observable budding step for DMVs[114]. We conclude that DMV formation is most consistent with a double-budding model where the inner vesicle forms completely within the ER lumen before budding out to obtain the outer membrane[203], [204].

While our work is in agreement with previous studies that show that DMVs are largely connected within the RVN[27], we show that nearly 20% of MHV DMVs are bona-fide vesicles which are separate from the RVN, and that DMVs are trafficked to lysosomes for degradation. DMVs thus appear to follow the ERAD tuning pathway in its entirety. While the connection of the formation of DMVs to the ERAD tuning pathway has been established[109], it has been assumed that the increase in DMV numbers over time indicates that the virus stalls or stops the ERAD tuning pathway[41], [109]. Our work challenges that notion by looking at later timepoints in infection. By 12 hpi, the decrease in the number of DMVs is noticeable. By 16 hpi, it is difficult to find a single DMV, let alone a cluster of DMVs, suggesting that this degradative process continues through infection.

The separation and trafficking of DMVs is consistent with live cell imaging indicating that MHV nsp2-labeled structures are present in two distinct populations, one of which was of smaller size

and mobile, and the other which were larger in size and immobile[103]. While the ultrastructures corresponding with the two populations were not visualized, it was assumed that the small structures were individual DMVs traveling toward the perinuclear DMV/CM clusters where they become immobilized. While this directionality is possible, our data indicates DMVs are trafficking away from the RVN toward lysosomes. Similar dynamics of ER-derived replication complexes in hepatitis C virus (HCV) have been observed by live cell imaging, but movement has been tied to formation and achievement of localization of the replication complexes without investigating trafficking for degradation[103], [205]. In EAV, dsRNA is used as a marker for DMVs and the amount of dsRNA decreases during the last two-thirds of the observed infection[206]. EAV DMVs also form from the ERAD tuning pathway[206], so it is tempting to speculate that they have a similar degradative fate as those of MHV. It is possible that this degradation of replication proteins and RNA may be a theme in other viruses as well, as the role of ERAD proteins has also been established for a flavivirus[207] and a coxsackievirus[208].

The fact that DMVs are disposed of also reiterates questions about DMV function within infection. Because of the presence of dsRNA and viral nonstructural proteins in and around DMVs, it was initially hypothesized that DMVs are the site of CoV replication[27], [40]. Evidence is growing that DMVs are not the sole site of active replication, and involvement with replication may be transient. Various replicase proteins do not colocalize throughout infection[209], [210], and newly synthesized viral RNA colocalizes with dsRNA early but not late in infection, indicating that dsRNA may not solely represent the replicative intermediate in active replication[211]. With temperature sensitive MHV mutants, it was shown that the size and number of DMVs does not correlate to viral fitness, thus further uncoupling DMVs from replication[212]. Along with our data, these literature support a model where any involvement of DMVs in replication occurs transiently sometime before the DMVs are degraded. Perhaps that involvement or loading of DMVs occurs during the formation of the inner vesicle, a rapid morphological process that has yet to be visualized.

In addition to the formation of the RVN, the ER plays a role in MHV assembly. Because both replication and assembly involve membrane proteins that must be processed through the ER, the processes occur somewhat simultaneously, but involve different morphologies and proteins. Three

virally-encoded nonstructural proteins together form DMVs[78], which we show are produced by budding out from the ER. In contrast, envelopment of new virus particles produces negative curvature of the ER into its lumen, mediated by the structural proteins M, E, and S[81]. These two processes are largely separated in time, with DMV formation being the dominant process in the ER up to around 10 hpi. By 12 hpi, the ER is extensively involved in the assembly process, and DMV formation has slowed or stopped altogether. These observations raise questions as to what governs the switchover in the role of the ER. Is it controlled by the cell or by the virus? Does replication slow late in infection, allowing the ER to be used for assembly? Or does the translation of vast quantities of structural proteins in effect edge out the nonstructural proteins, causing DMV production to slow? Or do the structural proteins and thus the assembly process "back up" into the ER due to the virus particles budding downstream in the secretory pathway? Additionally, the large capacity of the ER compared with the ERGIC and Golgi raises questions about the logistics of processing such large numbers of viruses through the remainder of the secretory pathway. Perhaps many of the ER-budded VP are not released from the cell or perhaps CoV utilize a non-conventional pathway from the ER out of the cell.

Overall, this work provides morphological definition to the dynamic rearrangements of the ER by a coronavirus. We show that DMVs have a lifecycle consisting of formation of the inner vesicle through an unknown mechanism, budding from the ER, association with the RVN, separating from the RVN and trafficking to the lysosome for degradation (Figure 2.10). The formation and degradation rates are such that through the infection, the number of DMVs increases early in infection, followed by a dramatic decrease between 10 and 12 hpi. Concurrent with the RVN breakdown, virus assembly on the ER is increasing rapidly, necessitating major structural changes to the organelle. While our work here is based on ultrastructural imaging, it opens up a multitude of questions that can be addressed by other techniques. Future understanding of what controls the DMV degradation rate, or what causes the ER to suddenly begin assembling thousands of new virions could provide the basis for new strategies to combat coronavirus infection.

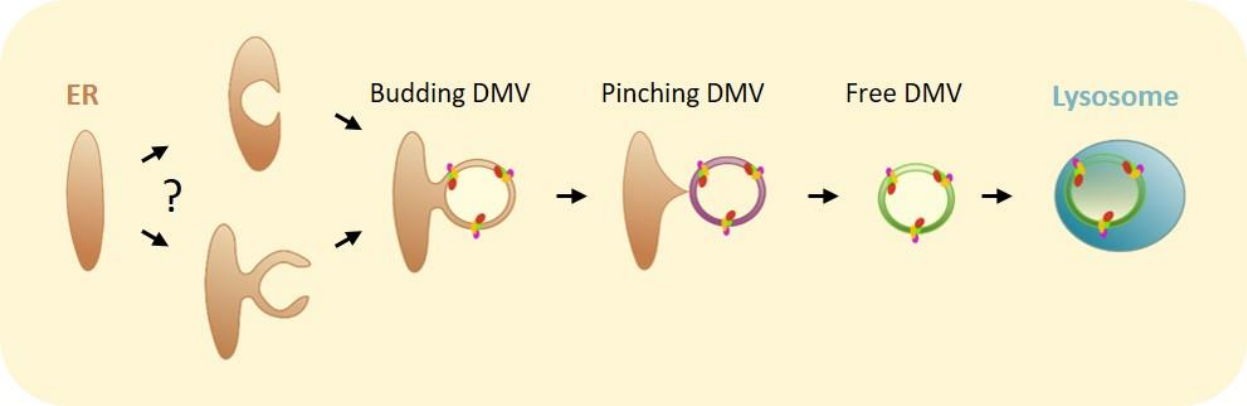

Figure 2.10. Morphological model of a DMV life-cycle. Our model proposes that first, the inner DMV vesicle is formed within the ER by one of several possible topologically-equivalent processes, followed by budding out of the ER to obtain a second membrane. DMVs may remain connected to the ER and the RVN via pinching connections for some time before separating to become free DMVs. Free DMVs are trafficked through the cytoplasm on microtubules and merge with the lysosome for degradation. Together these steps describe a morphological birth, lifetime, and death of a DMV.

CHAPTER 3. ALPHAVIRUS-INDUCED MORPHOFUNCTIONAL CONVERSION OF THE HOST GOLGI APPARATUS

A version of this chapter has been submitted for publication. This work was done in collaboration with Dr. Ranjan Sengupta.

Venezuelan equine encephalitis virus (VEEV), like other alphaviruses, induces the formation of prominent cytopathic vacuoles known as CPVII that are thought to be involved in virus egress. However, the origin and significance of CPVII remain poorly understood. We employed electron tomography (ET) in combination with peroxidase-based localization to demonstrate that the host cell Golgi apparatus is directly remodeled into CPVII in VEEV-infected mammalian cells. Appearance of CPVII is preceded by vacuolization and concurrent bending of the Golgi cisternae. The latter mechanism of cisternal bending produces double lamellar CPVII with membrane-bound nucleocapsid cores (NC) trapped within. We provide 3D-ultrastructural evidence that internal NC can undergo envelopment within the lumen of these CPVII and consequently reaches the plasma membrane along with the other forms in large clusters. Overall, tomographic imaging of multiple Golgi stacks in morphological transition reveals a model for the pathogenic transformation of an organelle into vesicles that ferry viral NC and intracellular budded virions to the plasma membrane, the primary site for alphavirus egress.

3.1 Introduction

In a eukaryotic cell, membrane-bound organelles over their life-time transition through multiple morphofunctonal states[213], [214]. In addition to endogenous events, morphological remodeling of organelles is also observed during virus infection of the host cell. These remodeled organelles cradle the viral replication machinery and are thought to shield it from host immune surveillance[14], [19], [21], [26], [215]–[217]. In addition to this, a major restructuring of the host-cell secretory system has also been observed associated with virus maturation ad egress. However not much is known about the morphological steps involved in the organelle remodeling and biogenesis of these virus induced structures[218]. One such virus family that makes use of remodeling of host organelles are the alphaviruses[172], [176], [180], [181].

Alphaviruses are enveloped, icosahedral (~700 Å dia), positive-strand RNA viruses that include significant human pathogens such as Chikungunya virus (CHIKV) and encephalitic members like Venezuelan equine encephalitis virus (VEEV), eastern equine encephalitis virus (EEEV) and western equine encephalitis virus (WEEV) that causes high mortality in both human and equines. Their genomic RNA is encapsidated by capsid proteins to form a nucleocapsid core (NC). The NC (~40nm in diameter) comprises of 240 copies of capsid protein arranged around the viral RNA [151], [219]. The virion envelope consists of a host-derived lipid bilayer in which 240 copies of glycoproteins, E1 and E2 are embedded[220]. The NC interacts with the host membrane via its interaction with the carboxy-terminal domain of E2 (cdE2) [177]–[179]. The E1 and pE2 (precursor to the E3 and E2 proteins prior to furin cleavage) glycoproteins are assembled as heterodimers in the endoplasmic reticulum (ER). E3 is cleaved from pE2 by furin in the Golgi, and the resultant E1–E2 heterodimers are then transported to the plasma membrane[221]. The mechanism of transport of these glycoproteins to the site of budding at the PM is not well understood.

Two types of vacuolar systems, namely cytopathic vacuole type I and type II (CPVI and CPVII), have been morphologically identified and associated with early and mid-to-late stages of alphavirus infection respectively. While CPVI has been shown to house the alphavirus replication complex, not much is known about biology and significance of CPVII [34], [35], [176], [222]**.** Early studies have implicated the GA as the progenitor of CPVII but to date there are no specific marker studies, and identification is based solely on morphology[180], [182].They are described as pleomorphic vesicular structures, 0.2-1.5 μm in diameter, with nucleocapsid cores (NC) bound to its membranes [172], [174], [176]. They exist as a milieu of uni- and bi-lamellar forms that, curiously, sometimes contain enveloped virions in their lumen [172]. However, in the absence of any direct evidence for intracellular budding, these CPVII structures are thought be endocytosed virions. The association of NC with CPVII is mediated by the capsid-E2 interaction, potentially bringing the key viral structural proteins necessary for virion budding onto one membrane platform [177]–[179]. This notion makes CPVII an attractive candidate for co-transporting E2 and capsid (NC) to the plasma membrane, the primary site of budding of alphavirus in mammalian cells[174], [223]. Despite this, the origin, biogenesis and the significance of these unique vacuolar structures continues to be one of the enduring mysteries of this highly researched family of virus.

In this work, using collective evidence gathered from 2D EM screening, high-resolution Golgi marker study and finally serial-section electron tomography, we put forth a 3D morphological model for how the host Golgi apparatus is remodeled into CPVII during alphavirus infection. ET of large, complex vesiculo-cisternal intermediates revealed details of at least two different mechanism by which the Golgi is converted into the various forms of CPVII. This study also provides the first direct structural evidence for the intracellular envelopment of an alphavirus in mammalian cells. Further, by extending our 3D analysis to the edge of the cell, we show that CPVII form clusters and accumulate at the plasma membrane. Our findings thus provide direct and conclusive structural evidence for conversion of the GA *en bloc* into containers for intracellular envelopment and transport via which alphavirus nucleocapsid cores reach the plasma membrane.

3.2 Materials and Methods

3.2.1 Cell culture and virus infection

Baby hamster kidney cells (BHK-21, ATCC) were cultured in Dulbecco's modified Eagle's medium (DMEM) supplemented with 10% fetal bovine serum (FBS) at 37 ^{o}C in a 5% CO_2 atmosphere. BHK cells were infected with the vaccine strain (TC-83) of Venezuelan equine encephalitis virus at a multiplicity of infection (MOI) of 20. At various timepoints (3 hr, 6 hr, and 12 hr), infected cells were released from Nunc UpCell dishes non-enzymatically. Cell sheets were pelleted, resuspended in 20% BSA (Sigma) as a cryoprotectant, and pelleted again for cryo-fixation and preparation for electron microscopy (described below).

3.2.2 Localization of horse radish peroxidase (HRP)-tagged Golgi marker, mannosidase-II

BHK cells were transfected with mannosidase-II-mCherry-HRP (Golgi FLIPPER[224]) 8 hours prior to infection. Infection was carried out as described above, followed by pelleting and fixation with 2% glutaraldehyde for 30 min, washing 3x for 5 min with 0.1% sodium cacodylate buffer and 1x with cacodylate buffer containing 1 mg/ml 3,3′-diaminobenzidine (DAB) (Sigma-Aldrich). Pellets were then incubated for 30 min in a freshly made solution of 1 mg/ml DAB and 5.88 mM hydrogen peroxide in cacodylate buffer, pelleted and washed 3x for 5 min each in cacodylate buffer. Cell pellets were then resuspended in DMEM containing 15–20% BSA, pelleted again and

cryofixed by HPF. Samples were prepared for electron microscopy as described below. For further experimental details on the CryoAPEX method see Sengupta et al., 2019 [225].

3.2.3 Sample preparation for electron microscopy and tomography

Cell pellets in cryoprotectant solution were loaded onto membrane carriers (Mager Scientific) and cryo-fixed using the EM PACT2 high pressure freezer (Leica). Cryo-fixed cells were processed by freeze substitution using an AFS2 automated freeze substitution unit (Leica). Briefly, frozen pellets were incubated at -90 ^{o}C in a solution of tannic acid in acetone, followed by slowly warming to room temperature in a solution of uranyl acetate and osmium tetroxide in acetone. Samples were infiltrated with Durcupan ACM resin (Sigma) and blocks were polymerized at 60 ^{o}C. Thin sections (60-90 nm) were cut using the UC7 ultramicrotome (Leica), post-stained with 2% aqueous uranyl acetate and Sato's lead, and imaged on a Tecnai T12 microscope (FEI) operating at 80 kV. Thicker 250-nm sections were screened on a 200 kV (CM200 Philips) microscope. Samples from all time points were screened in both thin and thick sections. For tomography, serial sections of 250-nm thickness were collected on LUXFilm coated 2 x 1 mm copper slot grids (Luxel), post-stained, carbon coated, and overlaid with 10-nm colloidal gold particles (Sigma) for use as fiducial markers.

3.2.4 Large volume electron tomography data collection

Two large volume EM tomography data sets were collected covering an approximately 45 μm^2 area of a BHK cell through a depth of 2 - 2.5 μm (Fig. 3A-C). Images were acquired using a Titan Krios TEM (FEI) operating at 300 kV at room temperature, outfitted with a 4k x 4k UltraScan 4000 CCD camera (Gatan). Tilt series were collected with automation using the program SerialEM [196]. First, a low magnification image montage of the entire grid was created to use as a map for marking regions of interest. The area of interest in the cell was visualized and marked on consecutive serial sections. At each section, a tilt series was collected. For each tilt series, images were collected at tilts from +60 to -60 degrees in 2 degree increments. To increase the area covered by each image, 2 x 2 montage images were collected at each tilt at 14,000x magnification, corresponding to a 0.65 nm/pixel size at the specimen level. Such montage tilt series were collected through 10 serial sections (Tomogram 1) or 7 serial sections (Tomogram 2). Smaller tomograms

were collected at a pixel size of 0.8 nm, using a similar collection scheme, without serial sectioning or montaging.

3.2.5 Electron tomography data reconstruction and analysis

Tilt series were aligned and tomograms generated by weighted back projection using the eTomo interface of IMOD[195]. Serial section tomograms were aligned and joined in z to produce two reconstructed volumes with approximate dimensions 5 x 5 x 2.5 µm (Tomogram 1) and 5 x 5 x 2 µm (Tomogram 2). Membrane structures of interest were segmented by hand tracing using IMOD's Drawing Tools and Interpolator, and 3D surface mesh models were generated. NCs were segmented by placing a sphere with a diameter of 40 nm at the center of each density. Models for the two large tomograms were joined using cellular landmarks to determine translational and rotational parameters for alignment.

Size measurements for CPVII were obtained from the 3D mesh of the segmentation for each vesicle. The volume inside the mesh for each CPVII was calculated in IMOD, and volume was converted to diameter assuming spherical vesicles, for ease of comparison to existing CPVII measurements. Nearest neighbor distance analysis between each CPVII object and each Golgi object was conducted using the *mtk* program in IMOD. Classification of NCs was achieved by analysis of the radius of curvature on adjacent membranes of Golgi cisternae and Golgi-derived vesicles. The *imodcurvature* command in IMOD was used to identify areas on the segmented model with local radius of curvature between 20 and 60 nm, corresponding to the curvature produced by a budding 40 nm NC. These areas were colored red on the membrane, as shown in Figure S2. NCs adjacent these highly curved membranes were colored red, while NCs adjacent membranes having a radius of curvature greater than 60 nm (represented by no change in color of the membrane) were colored blue.

Details and illustration of lumenal distance measurements in Fig S5 can be found in the figure legend. At least 60 measurements were taken for each group, and the Mann-Whitney U test was used to compare each pair of distributions. Statistical analysis was done using R software [226].

3.3 Results

3.3.1 VEEV infected cells show progressive Golgi apparatus remodeling and associated emergence of pleomorphic cytopathic vesicles

CPVII are thought to originate from the medial/trans Golgi as early as 4 hours post infection[174]. Thus, we hypothesized that the Golgi apparatus goes through a morphological flux that precedes the formation of CPVII. Our TEM screen of 90 nm resin sections from different time points (3 to 24 hrs post infection) revealed that perturbations of the Golgi structure is evident as early as 3 hours post infection (Figure 3.1A, i-iv). Although the Golgi apparatus at this stage retains its typical stacked architecture (i, ii and iv, yellow arrow), distal Golgi cisternae appear distended d (iv, yellow arrow). Most stacks show mild herniations (iv, orange arrow) and are surrounded by various sized discrete vesicular structures of unknown origin (iii, red stars). None of the vesicular structures at this stage exhibit bound NC.

The Golgi architecture at 12 hours post infection, not only exhibited extensive herniations akin to the early time point during infection, but additionally exhibited unstacking and bending (Figure 3.1Bi to iv). At the perinuclear region, multiple Golgi structures manifested intermittent herniations along the length of the cisternae (ii, stack demarcated with a white box). Some Golgi remnants or ministacks (ii, demarcated with orange and blue circles) make sharp bends at various angles (iii, denoted by curved magenta bars). These changes are concurrent with a heavy presence of CPVII and NC in apposition with the Golgi (ii and iv red arrowheads). Many of the CPVII are seen in this micrograph to contain enveloped virions in their lumen (red and yellow arrows).

At six hours post infection, (Figure 3.1C, i and ii) CPVII are very evident in close association with the Golgi complex. TEM of thin resin sections (90nm) limited the sampling volume and is not suited for understanding the large complex organelle structure and the 3D space it occupies. Thus, to gain a better understanding of the size of these clusters and their complexities, thicker, 250 nm serial sections were screened from a 6-hour timepoint instead (Figure 3.1Ci, sections 1 through 20). Two perinuclear clusters of CPVII were followed through twenty, 250 nm sections (Z depth of 5000 nm) from the beginning to the end revealing that these perinuclear clusters of CPVII are all part of a larger vesicular system that could not be appreciated by thin section TEM screening.

Despite the fact that the thick sections stretched the limit of the 200kV TEM, that made the images look darker than thin sections (90 nm) collected at 80kV TEM, these images revealed valuable details on the morphology of the perinuclear CPVII clusters (Figure 3.1Cii areas 1 and Figure 3.1D, i through x).

A close inspection of the clusters (Figure 3.1Di, red and yellow boxes), revealed an intact surface of the CPVII studded with NC (Figure 3.1Dii, magenta arrows). These clusters are seen enmeshed and at times cradled by surrounding cisternae (Figure 3.1Cii and Figure 3.1D iii) exhibiting an "eggs-in-a-nest" arrangement. Further, the pleomorphic nature of the CPVII was also evident. A small cluster of elongated dumb-bell shaped CPVII was also observed indicating that these are perhaps intermediates of the Golgi remodeling pathway (Figure 3.1D iv, marked by an orange box and magnified image in Figure 3.1D v). The NC-studded surface of these structures is evident. Further, perturbation of these Golgi derived structures is evident (Figure 3.1D v to x). Magnified images (Figure 3.1D vii and viii) of areas demarcated by green and blue (Figure 3.1D vi) reveal bending of a Golgi stack into a donut like structure (Figure 3.1D vii) and herniation at ends of the stacks (Figure 3.1D viii, yellow arrow) appear to give rise to oblong and dumbbell shaped vesicular structures (viii, orange arrow). Among other structures also captured in this thick-section screening are herniated trihedral vesicles enmeshed within the Golgi complex (Figure 3.1D ix and x). Besides, the perinuclear region, multiple CPVII clusters were located near the plasma membrane (Figure 3.1E, i to iii). A closer look of this region (Figure 3.1E i, area within green box) by the PM of an infected cell revealed various forms of CPVII (Figure 3.1E iii, blue boxes and 1 through 4) in the mix that contains some with enveloped virions in its lumen (4).

Figure 3.1. VEEV infection induces progressive remodeling of the Golgi apparatus in BHK cells**. (A)** Representative TEM images from 90 nm resin sections showing Golgi stacks in BHK cells infected with VEEV at 3 hours post infection. (i) Low magnification image of a cell with the perinuclear region containing Golgi stacks outlined in blue. (ii) The area from (i) with two Golgi stacks outlined in blue [magnified in (iii)] and red [magnified in (iv)]. Most stacks show mild herniations within intact stack architecture (iii) surrounded by vesicular structures [marked by red stars in (iii)]. Large herniations of cisternae were also frequently observed [yellow arrow in (iv)] alongside the rest of the normal stack [white arrow in (iv)]. **(B)** Cells from 12 hours post infection exhibit disintegration of the structure of Golgi apparatus (i-iv). Section from a representative cell (i), exhibits a number of Golgi stacks [at a higher magnification (ii)] that exhibit both extensive herniation (stack within white box) and cisternal bending and separation clearly observed at a higher magnification [magenta crescents (iii) and (iv)]. Additionally, this stage is marked by the accumulation of CPVII vesicles containing budded virus within [(iii) and (iv), red and yellow arrow heads respectively] situated in close proximity to the Golgi stacks. The size of these vesicle as well as the number of virions inside were seen to vary greatly. To get a better idea of the spatial distribution of the CPVII vesicles in a whole cell, 200 nm thick serial-sections were obtained and a typical cluster of vesicles were followed through the sections [C(i) sections 1 through 20]. Vesicle clusters appearing from section 3 continued until section 17 indicating the large size (~ depth of 3.6 µm) of the vesicular cluster. A representative image from the serial-section stack (section 13, (ii) and magnified images of the area demarcated within white circles (1) and (2) show vesicular clusters enmeshed within the Golgi cisternae giving an "eggs in a nest" appearance (inset 1, blue arrow). At a higher magnification a better understanding of the morphology of the CPVII contained within these thick sections was apparent (D, (i) through (x)). The vesicles showed a "spikey" appearance when the surface membrane was intact indicating the presence of a dense complement of NCs on the surface [magenta arrows, (ii)]. These CPVIIs were a mix of spherical, oblong (I, II and iii) and even dumbbell shaped [(iv) and (v)]. A higher magnification screen of the Golgi stacks showed Golgi herniated ends of the Golgi cisternae breaking off to into dumb-bell shaped elongated vesicles [(vi) area within green box magnified in (viii)]. Some cisternae were also seen to be folding upon itself into a "donut-like" structure [(vi) area with blue box magnified in vii)]. Further, more complex modifications of the Golgi cisternae [(ix) and magnified image of the a complex intermediate (x)] provide definite evidence for Golgi remodeling. Besides the perinuclear region these CPVII clusters were also prevalent by the plasma membrane [E, (i) area with green box, magnified in (ii). Further magnified view of this cluster (iii) show the presence of 4 primary classes of CPVII [vesicles demarcated by blue boxes in (iii) and magnified view of the 4 types (1 through 4].

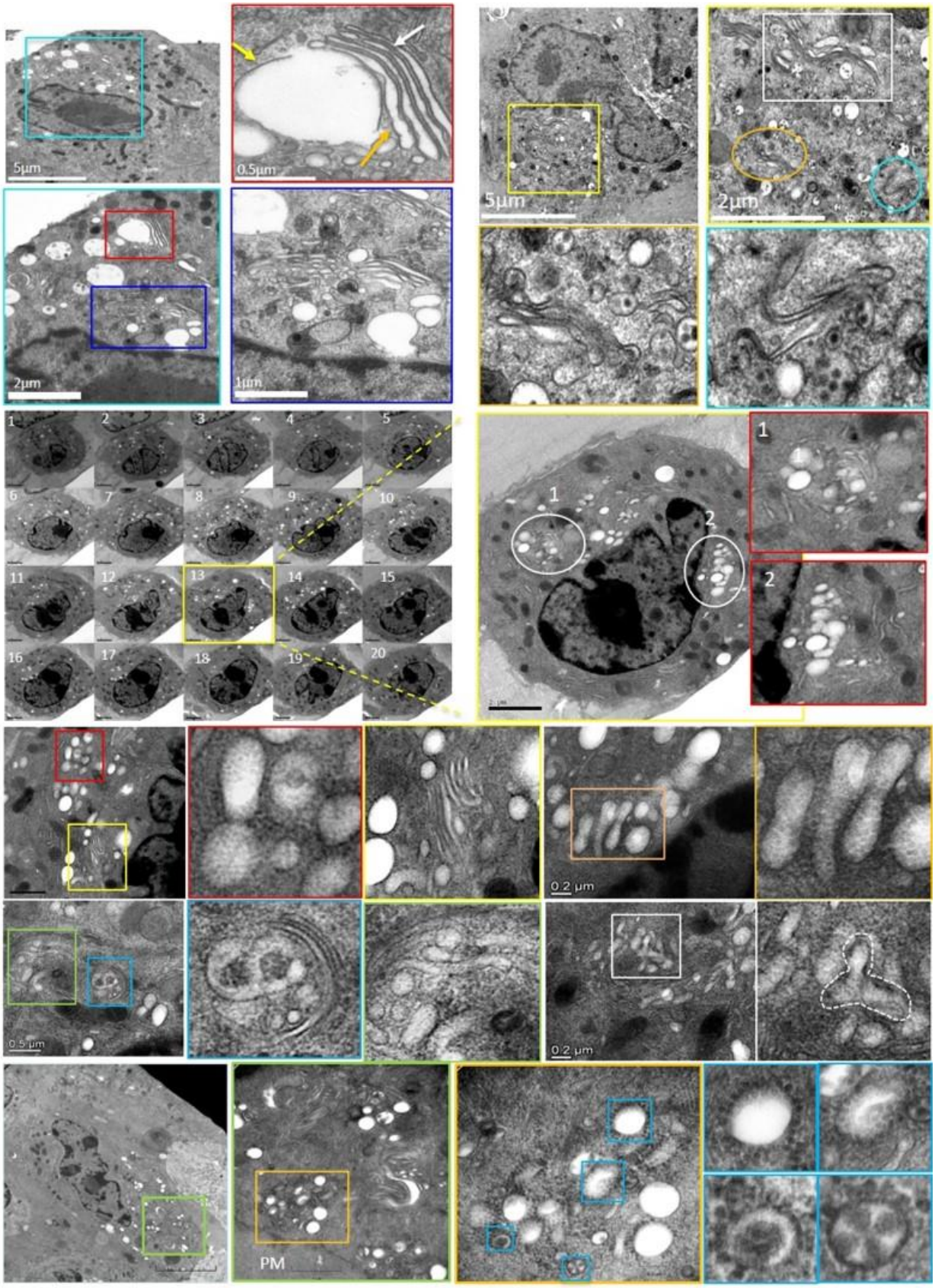
5μm
0.5μm
2μm
1μm
5μm
2μm
1
2
0.2 μm
0.5 μm
0.2 μm
PM

3.3.2 Modified CryoAPEX method reveals vacuolization of the Golgi cisternae

A recently published method for superior sample preservation post diaminobenzidine (DAB)-peroxidase staining for localization of APEX2 tagged proteins[225], [227] was modified for HRP-tagged α-mannosidase-II (Golgi FLIPPER[224]). The goals of these experiments were to determine the distribution of the ectopically expressed Golgi marker, α-mannosidase-II in VEEV infected cells. Infected cells were first fixed chemically with glutaraldehyde followed by incubation with DAB and hydrogen peroxide and then cryofixed via high-pressure freezing at 6 and 12 hours post infection, respectively. At 6 hours post infection, low magnification screening of 90 nm sections showed staining primarily localized at the perinuclear region (Figure 3.2A i, region demarcated with yellow box). A high magnification screen of this region revealed stained Golgi stacks (Figure 3.2A iii-v, blue arrowheads), and large vesicles (~200 -500 nm) associated with the stacks (Figure 3.2A ii, yellow arrows) that are evidently derived from the Golgi apparatus. Further, large cisternal herniations giving rise to distended vesicular structures that were still connected to the Golgi stack were observed (white and magenta arrows, Figure 3.2A iii to v). These distended cisternae were seen to originate from both the outer periphery of the stacks (white arrows, Figure 3.2A ii and iv) as well as from the middle of the stack (magenta arrows, Figure 3.2A iv and v). At this 6 hour time point, discrete vesicles carrying the MANII-HRP stain were detected at the plasma membrane (PM) (Figure 3.2A vi, yellow arrows).

The samples from 12 hours post infection revealed CPVII carrying the ManII-HRP stain at a high concentration at the perinuclear regions but also scattered throughout the cytoplasm leading up to the plasma membrane. Image of the representative section show stained vesicular structures at the perinuclear region (area demarcated with red box in Figure 3.2B i). Images of this region at a high magnification exhibit clusters of CPVII (Figure 3.2B ii, denoted by red arrows). A closer look at these vesicles revealed a mix of various morphological forms (Figure 3.2B iii, arbitrarily indicated with lower case alphabets, a, b and c). A dense complement of NC were observed associated with the cytopathic vesicles at these clusters. Free NC not apparently associated with vesicles were also observed associated with these clusters. However, it was not clear from thin sections whether they are indeed free cytoplasmic NC or they are bound to membrane below the plane of section

indicating that serial sectioning and/or 3D reconstruction would be better suited to conclusively determine that.

Figure 3.2. Pleomorphic CPVII in the perinuclear region and by the plasma membrane is of Golgi origin. A CryoAPEX method was optimized to detect the HRP-tagged α-mannosidase-II, a Golgi membrane marker, in VEEV infected BHK cell at 6 and 12 hours post infection [A (i)- (vi) and B (i)-(vi) respectively]. TEM images of 90nm resin sections at 6 hours show the manII-HRP Golgi marker localizes predominantly at the perinuclear region. Successive magnified views [(ii) through (v)] of the perinuclear region [(ii) demarcated with a yellow box in (i) and color coded henceforth] show herniated cisternae within the existing Golgi stacks (blue arrow heads) ballooning up (white arrows, iii, iv and v) and the area around littered with vesicle of similar sizes (that carries the Golgi marker substantiating our data from TEM screening presented in figure 1. These herniations and were not restricted either to the *trans*- or the *cis*- face but was seen to occur from cisternae in the middle of the stacks [white arrows,(iii) through(v)]. Progressive conversion of the cisternae into large vesicles and the replacement of a stacked structure with a cluster of vesicles is apparent (iv). These Golgi derived vesicles [(vi,) yellow arrows] were also found in small clusters at the plasma membrane ([(vi,) demarcated with white arrows].(B) Images of from 12 hours post-infection is usually predominated with all different classes of cytopathic vesicles (CPVII). Image of the section from the representative cell shows a similar distribution of CPVII as in the 6-hour time-point (i) with a higher density at the perinuclear region. High magnification this region [(ii), demarcated with a red box, in (i)] show the absence of stacked Golgi structures but a predominance of CPVII with detectable nucleocapsid cores (NC) associated with the vesicles [(ii), red arrows]. Some NC was also detected in free space within these clusters [(iv), white arrowheads] but could not be concluded if they were freely occurring in the cytoplasm or are indeed attached to CPVII excluded from the thin section during sectioning. Three classes of vesicular structure was observed namely, a crescent shaped structure with higher density towards the inner curved side indicating the presence of NC, a typical round vesicular structure with NC on the cytoplasmic surface, vesicle with enveloped virus within and NC on the outer surface [(iii) a, b and c respectively]. Magnified views of these predominant types of CPVII are also presented [(iv) and (v)]

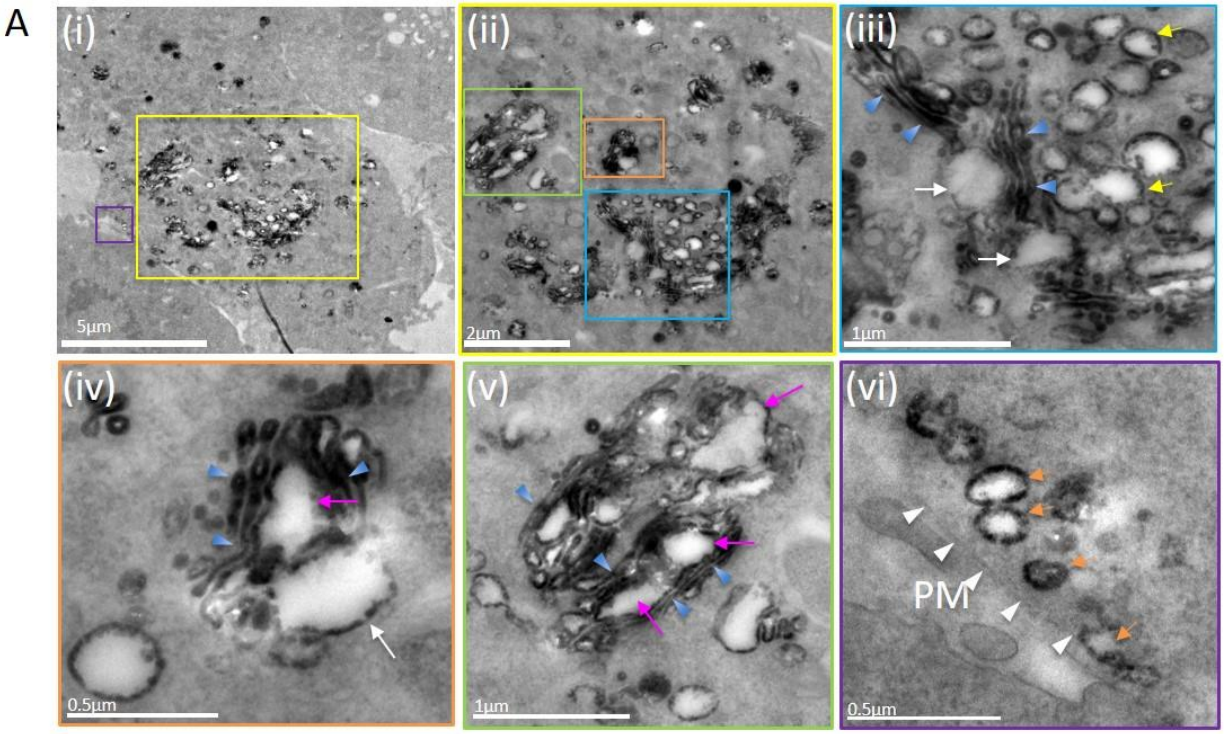
A
(i)
5µm
(ii)
2µm
(iii)
1µm
(iv)
0.5µm
(v)
1µm
(vi)
PM
0.5µm

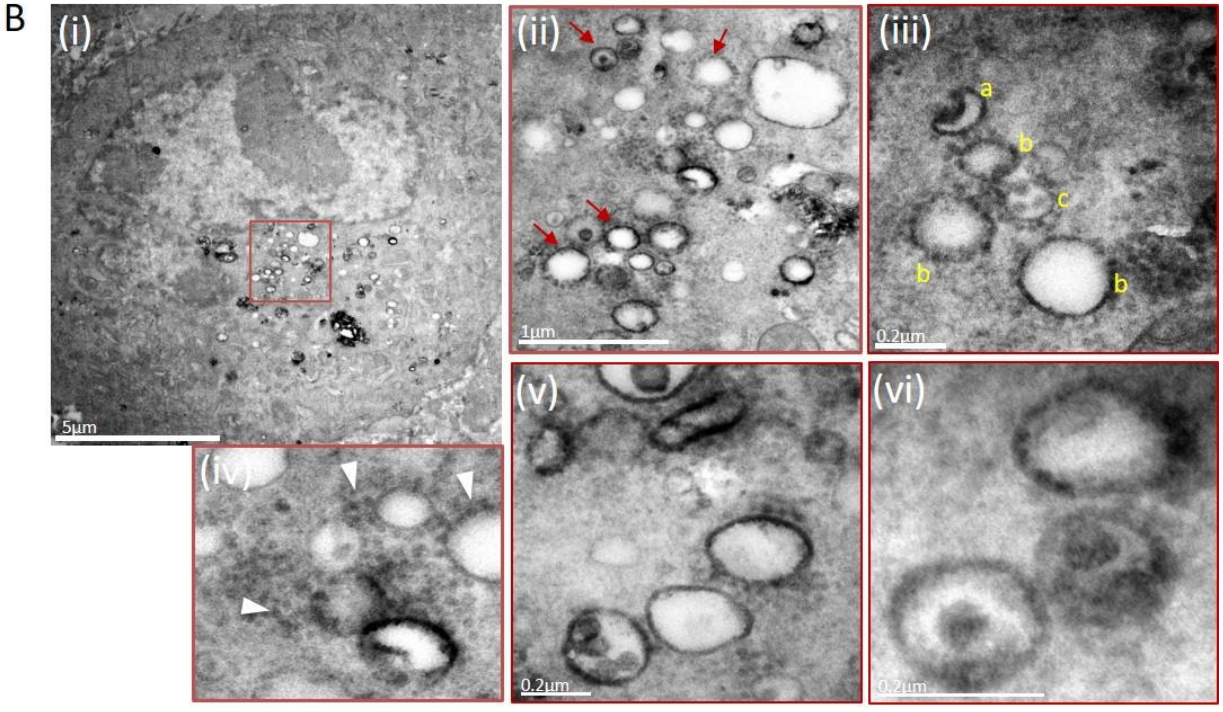
B
(i)
5µm
(ii)
1µm
(iii)
a
b
c
b
b
0.2µm
(iv)
(v)
0.2µm
(vi)
0.2µm

3.3.3 Large volume electron tomography reconstruction of a representative cell infected with VEEV

The 2D screening of infected cells at different time points post-infection and the Golgi marker study revealed several key aspects of Golgi remodeling during VEEV infection. First, changes in Golgi morphology begin early in infection and continue through late stages. Second, the Golgi is converted into vesicular structures, some of which seem to form as a result of Golgi cisternal herniations. Third, serial-section screening revealed that CPVII are present in large clusters extending through a large volume of the cell. CPVII exhibit multiple distinct morphologies, for which the mechanisms of formation are not immediately apparent. Finally, all forms of CPVII carry the Mann-II marker. This includes the CPVII which contain enveloped virions within their lumen, indicating that intracellular envelopment of VEEV in mammalian cells occurs on membrane derived from the Golgi apparatus.

Based on these observations, a 3D view of the Golgi during VEEV infection was required to further investigate the morphological changes and remodeling of this large and intricate organelle. In order to obtain a high resolution, 3D view, we collected electron tomograms of a large volume of a VEEV-infected cell. First, cells were infected with VEEV strain TC-83 at a multiplicity of infection of 20. At 12 hours post infection, the cells were fixed by high pressure freezing, followed by freeze substitution and embedding in resin. 250-nm thick sections of cells were collected and screened on a 200 kV microscope for cells with multiple Golgi stacks and CPVII visible. Such a cell was identified that spanned several consecutive sections on the EM slot grid. A tilt series was collected on each serial section using a Titan Krios operating at 300 kV at room temperature. A projection image of one of the cell sections with the two areas selected for imaging is shown in Figure 3.3A (blue and red outlines). To produce the two volumes, tomograms were reconstructed and serial sections were stitched together in z, such that each volume covered an approximately 5 x 5 µm area with depths of 2.5 µm and 2 µm, respectively (Figure 3.3B-C).

The two volumes overlap to together span the perinuclear region to the plasma membrane (Figure 3.3A). Segmentation of the structures of interest provided 3D snapshots of five Golgi stacks, with three undergoing significant morphological perturbations. We were also able to sample hundreds of CPVII including possible transitional forms. An overview of the segmented structures,

including Golgi (green), CPVII (gold), and the plasma membrane (grey), are shown in Figure 3.3D. These volumes and segmented objects form the basis for subsequent analysis.

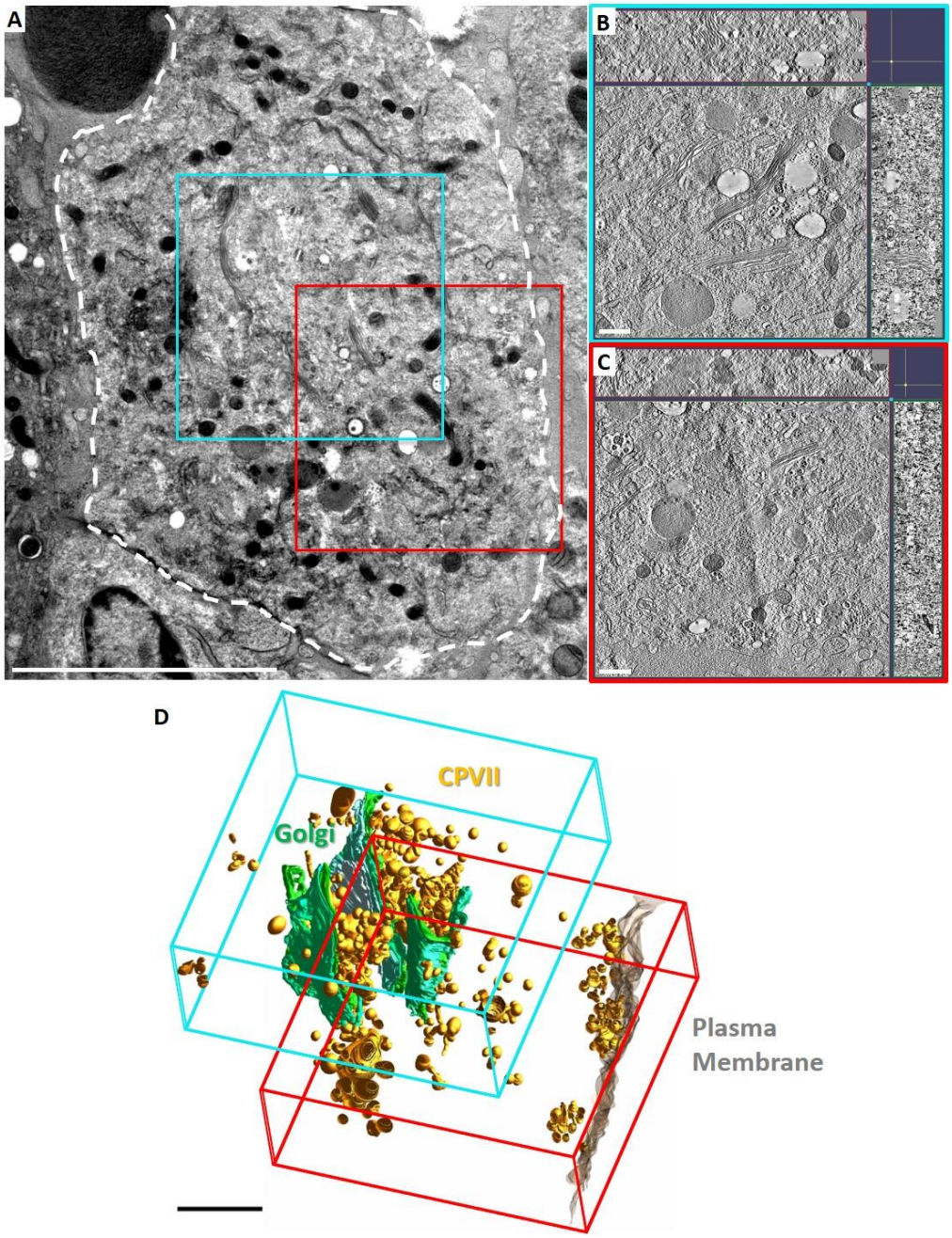

Figure 3.3. Large volume tomogram of a VEEV-infected cell. **(A)** TEM image collected at 300 kV of a 250-nm thick section of a TC83-infected BHK cell at 12 hours post infection (outlined in white). The approximate areas of this section and 8-10 subsequent serial sections used to collect tomograms are indicated by the blue and red squares. **(B-C)** A 3-nm thick virtual section from tomogram 1 **(B)** and tomogram 2 **(C)** with the z-depth along the x and y axis shown along the top and right side, respectively. **(D)** 3D visualization of the combined tomogram volume with segmentation of Golgi (green), CPVII (gold) and plasma membrane (translucent grey), and approximate tomogram boundaries in blue and red. **Scale bars:** (A) 5 μm, (B-C) 500 nm, and (D) 2 μm.

3.3.4 Identification and three-dimensional analysis of four morphological forms of CPVII

To date, published ultrastructural data on CPVII has been obtained via two-dimensional EM studies. Due to the complex morphologies and 3D nature of CPVII, we undertook a comprehensive three-dimensional study of the CPVII in our large volume tomogram. As previously mentioned, a CPVII is defined as a vesicle with NCs bound to its membrane. NCs are easily identified in EM as electron-dense spheres with an approximate diameter of 40 nm [151]; thus CPVII are also readily identified. In the large volume tomogram, we observed 353 discrete vesicles that can be categorized as CPVII, as well as amorphous vesicular structures with bound NC (discussed later). After segmentation and 3D visualization of each CPVII, we identified four distinct morphological forms of CPVII. First, class 1 CPVII were defined as single membrane vesicles with NC bound to their cytoplasmic surface (Figure 3.4). Class 2 was comprised of vesicles containing an invagination with NC bound to the membrane in the invaginated space (Figure 3.4B). Class 3 contained double membrane vesicles, with NC bound to the inner membrane and variably present on the outer membrane (Figure 3.4C). Finally, class 4 vesicles were defined as single-membrane vesicles with enveloped virus particles inside and NC variably present on the outer membrane (Figure 3.4D).

The four classes of CPVII were next analyzed for spatial distribution, size, and distance from the nearest Golgi stack. Figure 3.4E depicts the 3D segmentation of each CPVII, color-coded by class and shown with the *trans*-most Golgi cisternae of the relevant Golgi stacks and the plasma membrane for spatial reference (see also Figure 3.5). CPVII were found predominantly near the *trans*-Golgi, with several clusters of CPVII present throughout the cytoplasm and near the plasma membrane. Of the 353 CPVII, class 1 were the most abundant at 145 vesicles (41%), followed by class 3 (90, 26%), class 4 (78, 22%) and class 2 (40, 11%) (Figure 3.4E). The sizes of classes 1, 3, and 4 were also analyzed by calculating the volume of the segmented volumes for each vesicle using IMOD [195], and converting volume measurements to diameter assuming a spherical shape (Figure 3.4F). For class 3, the outer membrane was used for size calculations. CPVII in classes 1, 3, and 4 had similar diameter distributions for the interquartile range, with means of 326, 340, and 286 nm, respectively.

Class 1 had a notably broad distribution with diameters ranging from 22 to 1667 nm, although few extremely large vesicles were observed. Class 3 had no vesicles smaller than 214 nm, and a fairly narrow size range up to 662 nm. We also examined the distance of CPVII from the nearest Golgi cisterna, utilizing nearest neighbor analysis of the closest approach of the 3D objects in IMOD (Figure 3.4G). The results of this analysis show that all forms of CPVII are present near the Golgi, as well as at greater distances including in the clusters at the PM (see also Figure 3.4E). Classes 2 and 3 were predominantly present within 500 nm of the nearest Golgi cisterna, and rarely observed at greater distances. Classes 1 and 4 were the two classes found frequently at distances greater than 1500 nm from Golgi, representing many of the CPVII in clusters near the plasma membrane. Class 1 also contained a large number of vesicles in close proximity (< 1000 nm) to Golgi, while Class 4 was the only class that was not present with increased abundance near the Golgi. These collective observations of the variability in morphology, size, and distribution of CPVII raises questions as to their mechanisms of formation from the Golgi as well as their functions in virus infection.

Figure 3.4. Identification and three-dimensional analysis of four morphological forms of CPVII. **(A-D)** A representative vesicle from each of the four CPVII classes observed in the large volume tomogram are shown in three views: 3-nm thick virtual sections (top image), full 3D models made partially transparent (middle image), and 3D cutaway models (bottom image). NC **(C, arrowhead)** are distinguishable from fully enveloped virus particles **(D, arrowhead)**. **(E)** Spatial distribution of segmented CPVII forms in the combined tomographic volume are shown in reference to the *trans*-most Golgi cisternae (green) and the plasma membrane (translucent grey). CPVII are color-coded by class: class 1 (blue), class 2 (red), class 3 (gold) and class 4 (lavender). The pie chart in the upper left shows the fraction of vesicles in each class. **(F)** For the three classes of roughly spherical CPVII, the volume of each vesicle was calculated from the segmented mesh, and a diameter was approximated for each vesicle. Size distributions for class 1, 3, and 4 CPVII are represented as a box plot with outliers representing data points beyond 1.5 times the interquartile range. **(G)** Plot of the distance to the nearest Golgi cisterna for each CPVII, separated by class. **Scale bars:** 100 nm (A-D) and 1 μm (E).

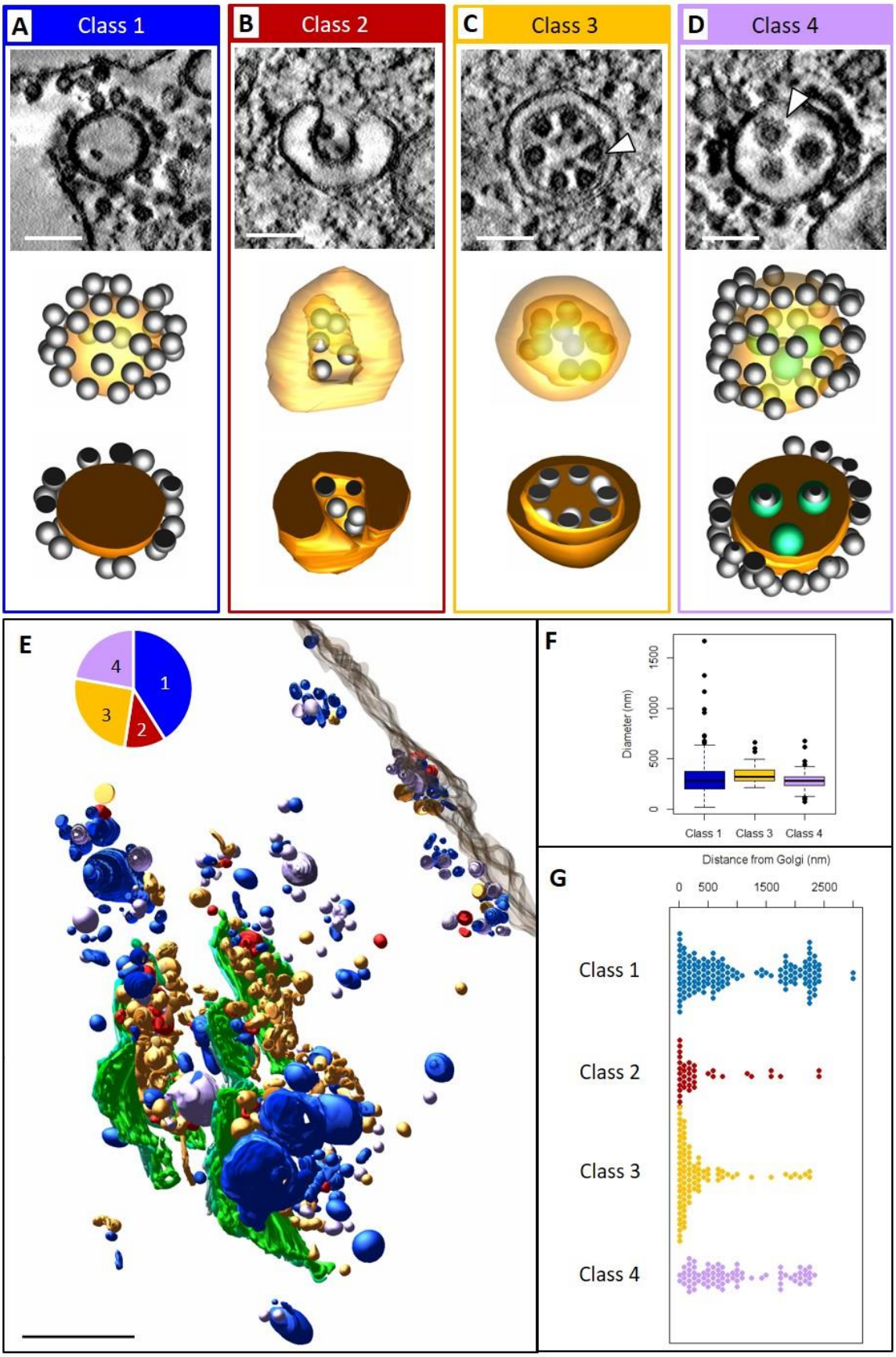
A
Class 1
B
Class 2
C
Class 3
D
Class 4
E
4
1
3
2
F
Diameter (nm)
0
500
1000
1500
Class 1
Class 3
Class 4
G
Distance from Golgi (nm)
0
500
1500
2500
Class 1
Class 2
Class 3
Class 4

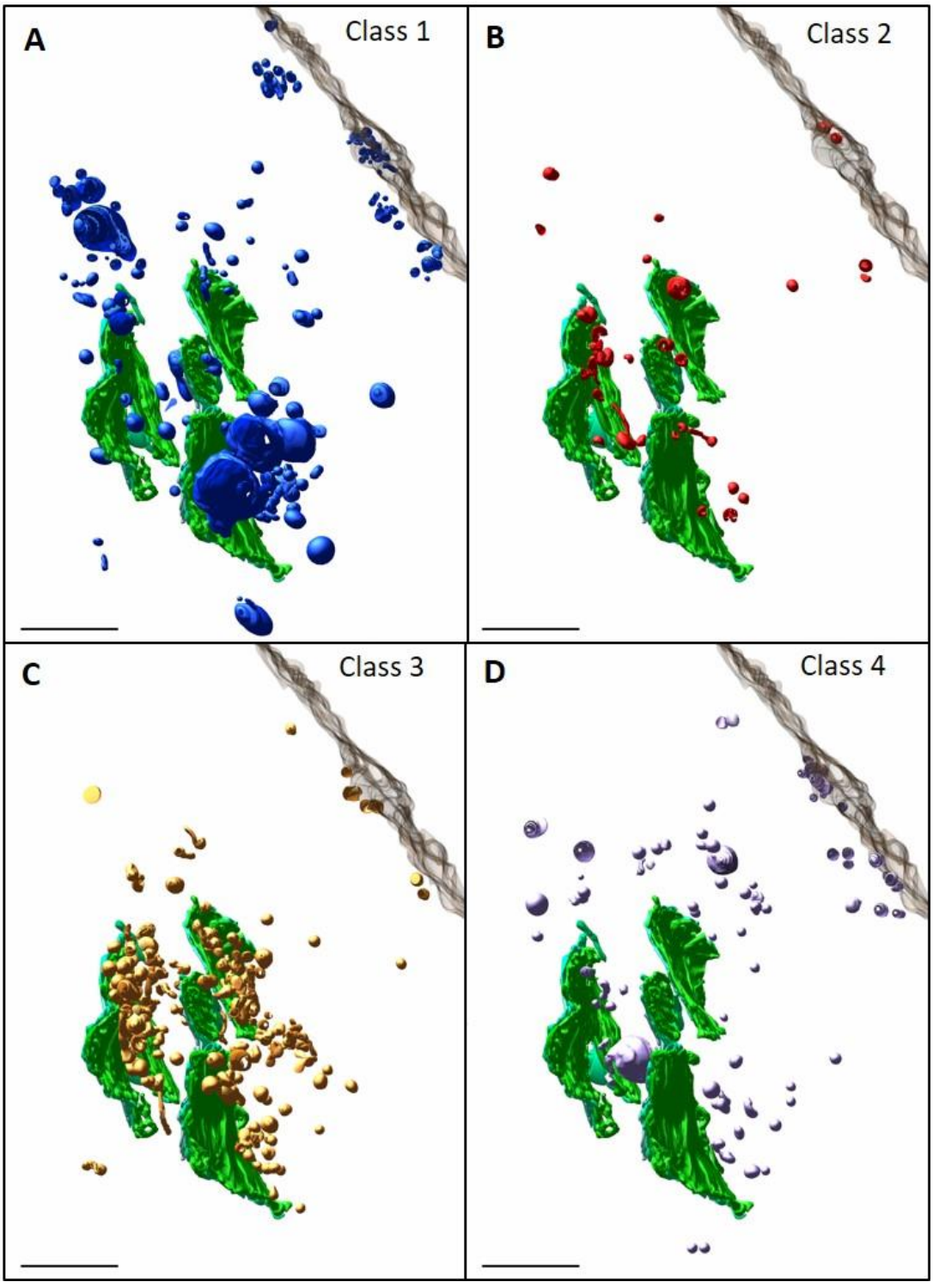

Figure 3.5. Distribution of the four classes of CPVII. Segmented CPVII forms in the combined tomographic volume are shown in reference to the *trans*-most Golgi cisternae (green) and the plasma membrane (translucent grey). The distributions for class 1 **(A)**, class 2 **(B)**, class 3 **(C)** and class 4 **(D)** are shown separately, from the same view as that in Figure 3.4E.

3.3.5 Three-dimensional analysis of a vesiculating Golgi

Since we have shown that CPVII have considerable morphological complexity, and that all forms of CPVII originate from the Golgi, we next examined the Golgi stacks present within our large volume tomogram in order to look for evidence of CPVII formation. One of the Golgi stacks had closely-associated large vesicles, reminiscent of those observed at earlier timepoints by 2D EM, and shown to be of Golgi origin (Figure 3.6A, compare to Figure 3.1A and Figure 3.2A). While the presence of NC on the vesicles in 2D was either not observed (at early timepoints) or perhaps not visualized, the large vesicles in the tomogram clearly have large numbers of NC bound to their cytoplasmic surfaces, giving them technical classification as CPVII. In particular, one large irregularly shaped vesicle of approximately 1.5 µm diameter came into close apposition with the *trans*-most Golgi cisterna of the stack (Figure 3.6B-C). This vesicle was separated from the cisterna by a single layer of NC which contacted both the CPVII and the Golgi membrane simultaneously (Figure 3.6C-E). Segmentation and 3D visualization of this vesicle and cisterna revealed increased NC density in the region where the vesicle was bound (Figure 3.6F-G).

The visible deformation in the Golgi cisterna where the CPVII was positioned further confirmed the tight association of the CPVII with the Golgi (Figure 3.6G). Examination of the immediately surrounding region revealed several additional large, irregularly shaped CPVII, as well as closely associated smaller class 1 and class 3 CPVII (Figure 3.6H). Vesicles were apparently connected into a large cluster by NC bivalently bound to two or more vesicles (Figure 3.6C black arrowheads). While most of the vesicles in the cluster fell within the typical size range of CPVII, it is noteworthy that the three large vesicles in this cluster were the three largest CPVII found in the volume, classified as type 1, but distinct outliers in terms of size (Figure 3.6I, circled data points). The vesicle highlighted in Figure 3.6F and found in closest apposition with the Golgi is the largest CPVII of the 353 analyzed in this volume. From our observations from the marker study as well as these rare large CPVII in the tomogram, it is tempting to interpret these large CPVII as portions of herniated Golgi cisternae. It is unknown whether these large irregularly shaped vesicles persist, or are unstable intermediates that may break down into the smaller, more spherical shaped class I CPVII observed throughout the volume.

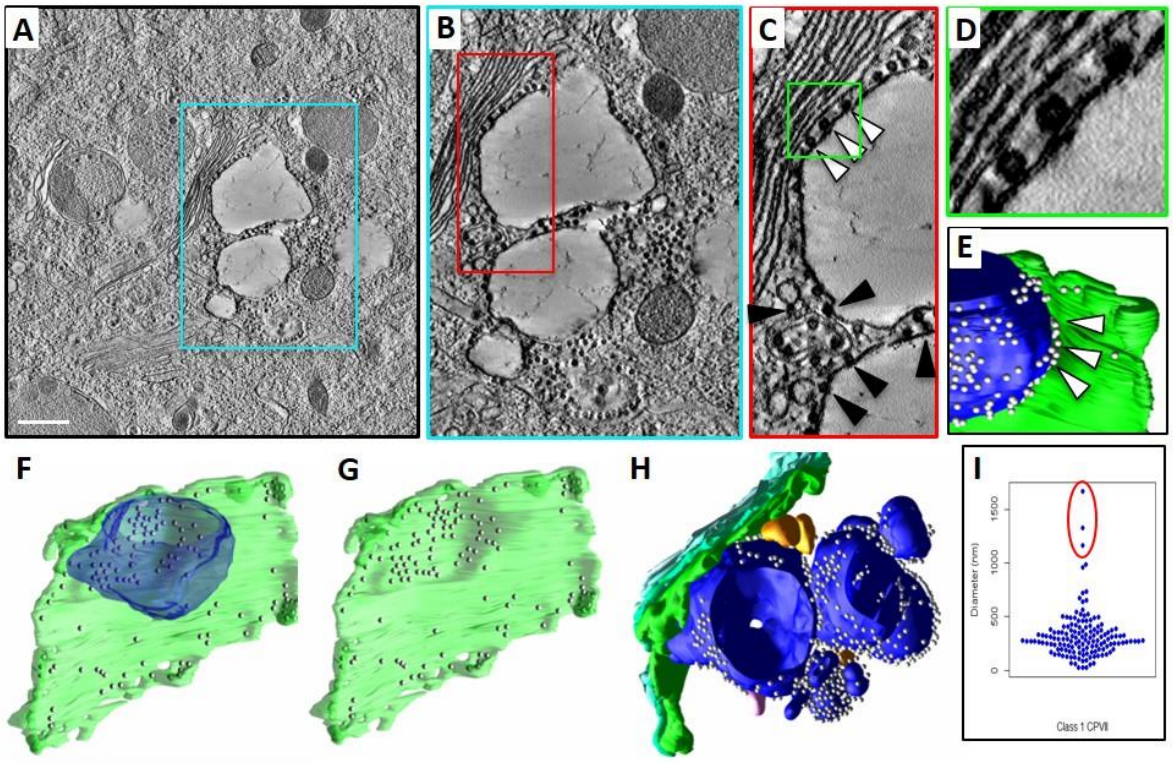

Figure 3.6. Three-dimensional analysis of a vesiculating Golgi**. (A-D)** A 3-nm thick virtual section from tomogram 1 showing a large CPVII abutting the intact *trans*-most cisterna of a Golgi stack, with increasing magnification of the region of interaction presented in the color-coded outlined areas in A-D. NC can be observed making contact with both the intact cisternal membrane and the vesicular membrane (**C** white arrowheads and **D**), as well as between multiple CPVII in the cluster (**C** black arrowheads). **(E)** A 3D view of the segmented CPVII region shown in C-D (blue), with NC (white spheres) filling much of the gap between the vesicle and the Golgi (green), indicated by arrowheads. **(F-G)** A 3D view depicting the entire *trans*-most cisternae shown in A-E with **(F)** or without **(G)** the large CPVII. A concentration of NC is seen on the Golgi at the interface with the CPVII, as well as an indentation in the Golgi where the vesicle was located. **(H)** 3D segmented view of the cluster of CPVII surrounding the large vesicle depicted in F, consisting of variably sized class 1 CPVII (blue) and their associated NC, and a few class 3 CPVII (gold), all in close physical proximity with the Golgi stack (green shades). The three largest class 1 CPVII in the volume are found in this particular cluster, as indicated on the plot of vesicle diameters for this class (**I**, circled in red). **Scale bar:** 500 nm (A)

3.3.6 Golgi cisternal rims exhibit bending in regions in contact with NC

In addition to the NCs bound to the Golgi simultaneously with the large class 1 CPVII, we also observed NC bound singly to the face of the intact *trans*-most Golgi cisternae. Many of these NC were bound to the cisternal rims as illustrated for Golgi 1 and Golgi 2, and we observed various degrees of cisternal bending away from the plane of the stack at the locations where the NCs were bound (Figure 3.7A-H). While membrane bending at the point of NC contact was often observed,

the bending was not indicative of virus envelopment or budding within the Golgi lumen as is observed in many intracellularly enveloped viruses. Rather, examination of the bent edges of the cisternae revealed that the cisternae bent around NC largely retained the narrow intra-luminal distance of cisternae present in a Golgi stack (Figure 3.7I-L). Multiple bending events were observed as tight cisternal curvature at the cisternal rims (Figure 3.7M-P). In order to visually clarify the membrane bending, we chose to highlight any bending that was possibly associated with envelopment by selecting NCs located on membrane which had a local radius of curvature between 20 and 60 nm, corresponding to the 40 nm radius of a NC (Figure 3.8). These NC were considered to be potentially budding, and were colored red in the 3D model. NCs located on membrane with radius of curvature greater than 60 nm were colored blue and were considered not budding. Bending of membrane was present clearly in regions of both "potentially budding" and "not budding" NC, and many of the "potentially budding" NC were likely not budding despite high curvature of the surrounding membrane (see Figure 3.7I-L)

In addition to the common observation of curling of the cisternal rims, a single large cup-like transformation of a Golgi cisterna was observed (Figure 3.7Q-S). This formation consisted of a largely intact cisternal structure curving away from the plane of the Golgi stack, with one edge closing up to form a vesicle-like structure (top-down view in Figure 3.7S). This form essentially represents a transitional intermediate between a flat Golgi cisternae and a double membrane vesicle. A high concentration of NCs are present on the inner membrane of this intermediate, but only 14 out of 97 NCs show membrane curvature indicative of potential budding events (red spheres in Figure 3.7S). This intermediate largely retained the characteristic intra-luminal distance of a Golgi cisterna (15-19 nm).

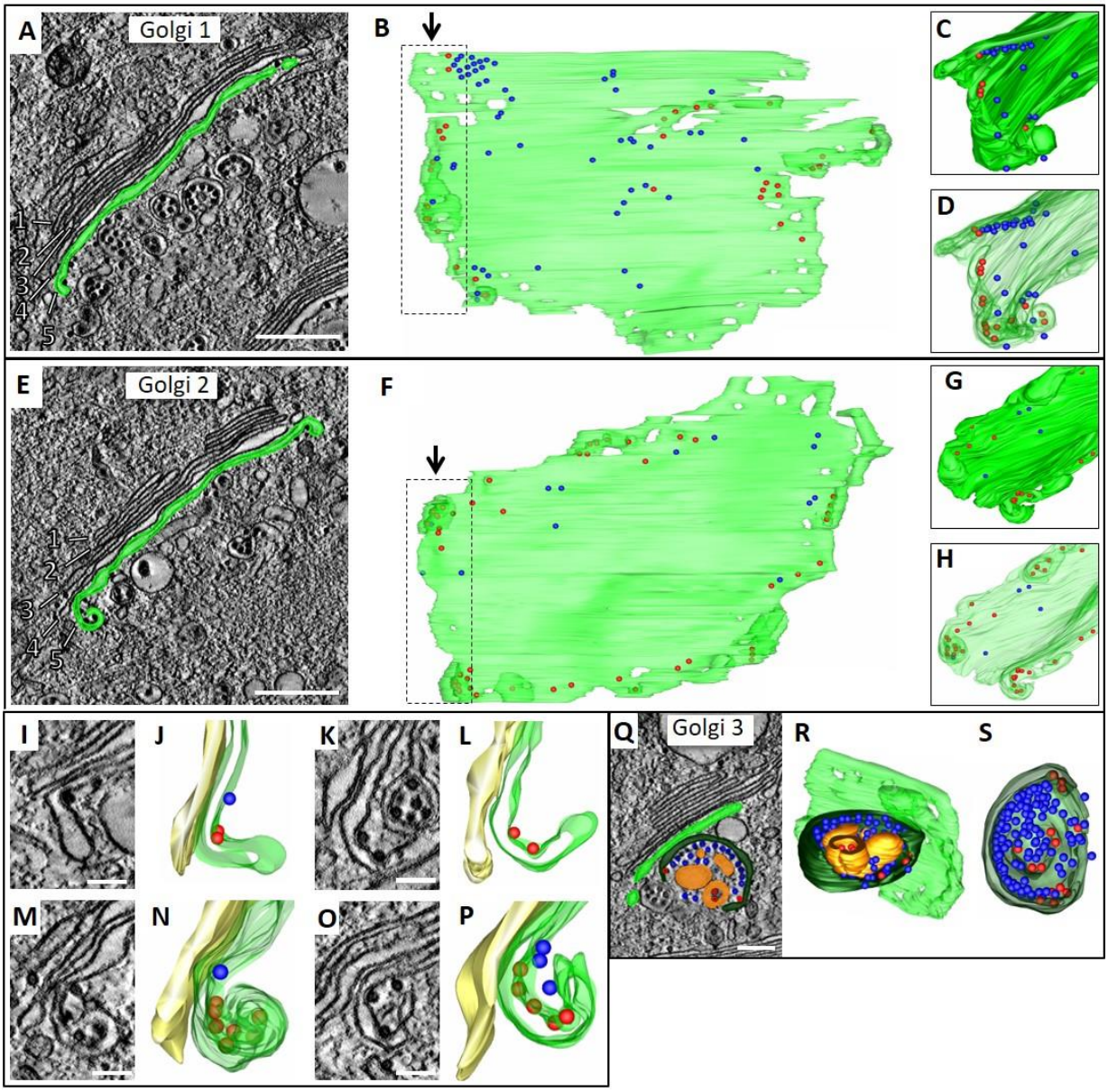

Figure 3.7. Golgi cisternal rims exhibit bending in regions in contact with NC**. (A)** 3-nm thick virtual section from tomogram 1, showing a Golgi stack ("Golgi 1") with the final intact cisterna colored green. Five cisterna are visible. **(B)** Three-dimensional rendering of the cisterna through the entire 2.5 μm depth of the reconstructed volume. Colored spheres represent NCs in contact with the Golgi membrane, colored blue or red based on the radius of curvature on the adjacent membrane as shown in Figure 3.8. **(C-D)** The curled edge of the cisterna viewed from the top down the cisternae in the direction of the arrows in panel B. **(E-H)** Similar views as A-D of a second Golgi cisterna through the depth of tomogram 1. **(I-P)** Edges of the cisternae (green) exhibit various degrees of curling away from the next cisterna in the stack (yellow). **(Q-S)** A third Golgi stack with a large portion of a cisterna (dark green) bending away from the adjacent intact cisterna (light green). The tomographic slice **(Q)** and 3D renderings **(R-S)** of this cupped cisterna which is bound with NC (red and blue) and encloses double-membrane CPVII (gold). **Scale bars:** 500 nm (A,E), 100 nm (I,M,K,O), and 200 nm (Q).

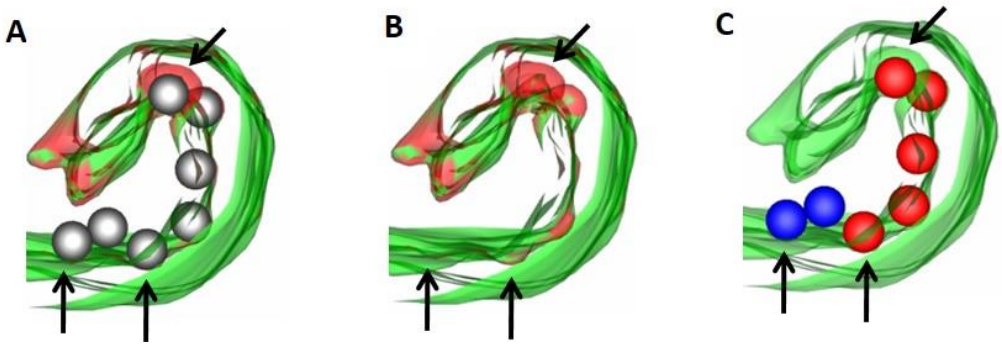

Figure 3.8. Color-coding of NC based on radius of curvature of the membrane to which they are bound The *imodcurvature* command in IMOD was used to identify areas on the segmented model with local radius of curvature between 20 and 60 nm, corresponding to the curvature produced by a budding NC (radius 40 nm). **(A)** The curled edge of a Golgi cisterna (green) with the Golgi membrane colored red in areas of radius of curvature between 20-60 nm. **(B)** The same view of the Golgi as A, without NC drawn. **(C)** NC were colored red in areas adjacent to highly curved membrane, while NC in areas with radius of curvature greater than 60 nm were colored blue.

3.3.7 Pleomorphic membrane structures with bound NC are fragmented Golgi cisternae

Immediately adjacent to the *trans*-face of Golgi 1, large pleomorphic membrane bound structures were observed (shown as 3D segmented model in Figure 3.9A). The structures closest to the Golgi stacks appeared to be discrete structures in single slices through the tomographic volume (Figure 3.9B, dark green and brown), but 3D segmentation revealed that they were partially intact Golgi cisternae still somewhat aligned with the stacked cisternae (Figure 3.9C-D). The central part of the structure shown in Figure 3.9C (area containing bound blue NC) retained flat cisternal morphology and maintained contact with the preceding cisterna in the stack (Figure 3.9B, arrowhead), whereas the outer edges exhibit a fenestrated morphology (Figure 3.9C arrowheads). Two small double-lamellar vesicular structures surrounding small groupings of NC were also present (Figure 3.9C, inset). The next closest cisternal structure, in brown, exhibits more vesicular structure than the previous, with long tubular elements connecting the vesicular formations (Figure 3.9D). Moving further from the *trans*-Golgi, pleomorphic CPVII structures were observed to contain combinations of small vesicular formations and tubules with highly varied morphology, with a few of the many observed formations being represented in Figure 3.9E-H. Some of these structures included up to ten connected vesicular formations, resulting in structures resembling bunches of grapes (Figure 3.9E-F). Other structures consisted of a few vesicles with tubular connections (Figure 3.9G), or even simpler, an individual vesicle connected to a single tubular component

(Figure 3.9H). Of note, the vesicular components within these complex membrane structures are all double lamellar in nature (Figure 3.9C-D inset and E-H cutaway views and arrows in tomographic slices). These vesicular formations resemble class 2 and class 3 CPVII and may represent formation intermediates between Golgi cisternae and those forms of CPVII. Of note, all of these structures required 3D imaging in order to appreciate their complex morphologies and connectedness (see 2D slices in Figure 3.9E-H). The CPVII forms reported from 2D studies so far may thus be a combination of discrete vesicles and pleomorphic forms. The pleomorphic forms were located exclusively in close proximity the Golgi, while the majority of CPVII in the volume were present as discrete vesicles, falling clearly into one of the four classes previously described.

Figure 3.9. Pleomorphic membrane structures with bound NC are fragmented Golgi cisternae. **(A)** 3D rendering of Golgi 1 *trans*-most cisterna along with selected pleomorphic CPVII forms closest to the cisterna (dark green, brown, gold) and associated NC (blue and red spheres). **(B)** 3-nm virtual section through Golgi 1, highlighting the intact cisterna (light green) and two large fragmented cisternae (dark green and brown) and their associated NC (blue and red spheres). **(C-D)** 3D renderings of two pleomorphic cisternal forms which are highlighted in dark green **(C)** and brown **(D)** in B. Insets of C and D show double-membrane nature of vesicular formations, with NC inside (red) and outside (blue). CPVII structures of varying pleomorphic shapes include forms with several double-membrane vesicular formations **(E-F)**, as well as vesicular and tubular elements **(G-H)**. Cutaway views in E-H reveal the double-membrane nature of the vesicular forms. 3-nm thick virtual sections from two depths of each form shown in E-H are presented with the segmentation of the structures of interest shown in gold and NC in red. The double-membrane character of the forms (similar to class 2 and 3) is pointed out by white arrowheads. **Scale bars**: 500 nm (B) and 100 nm (E-H)

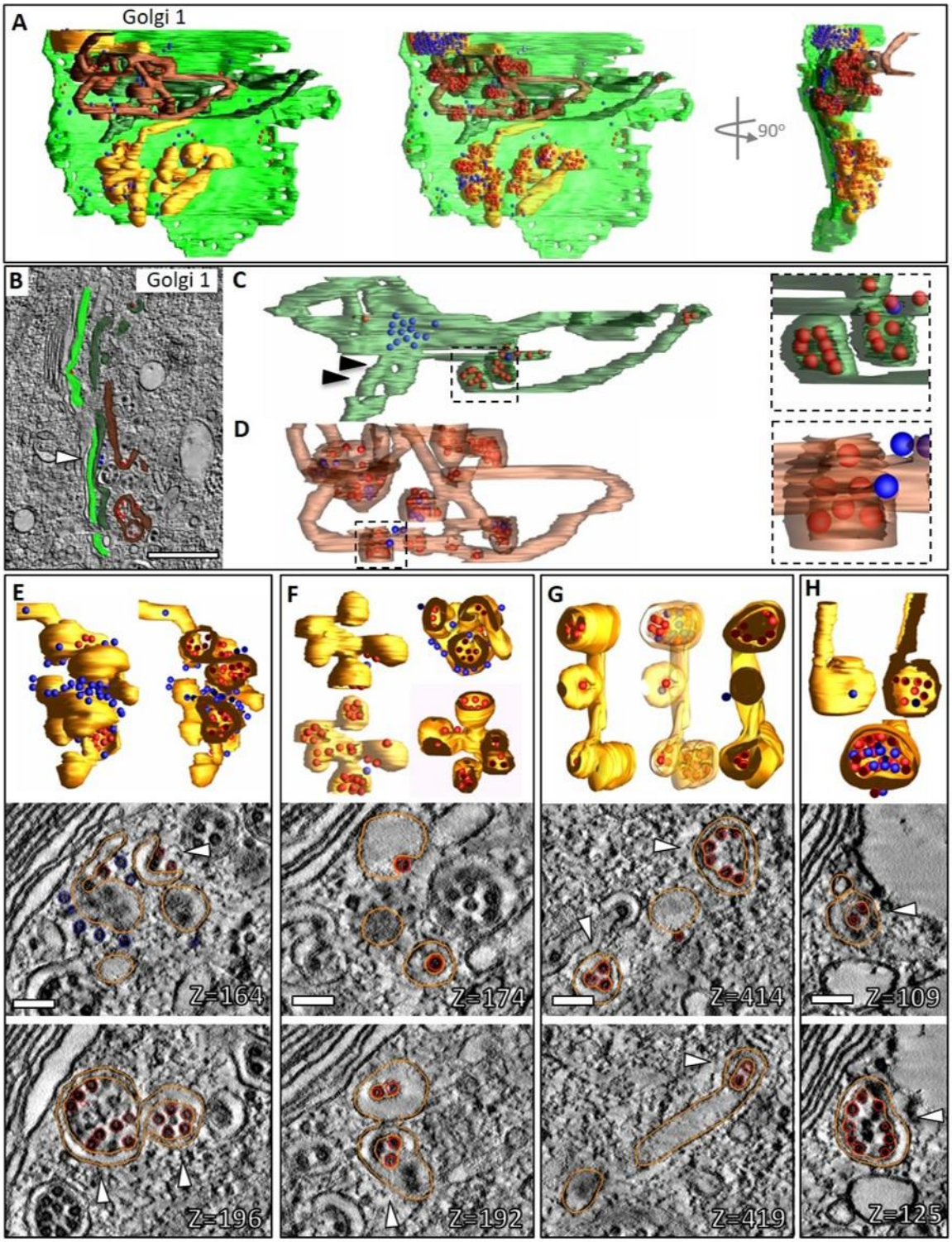
A
Golgi 1
90°
B
Golgi 1
C
D
E
F
G
H
Z=164
Z=174
Z=414
Z=109
Z=196
Z=192
Z=419
Z=125

3.3.8 3D analysis of intermediate forms between classes 2, 3, and 4 reveals a potential maturation pathway

In addition to the Golgi-CPVII intermediates just described, vesicles exhibiting intermediate features between the four defined CPVII classes were also observed. We examined these vesicles for clues about their relatedness. First, vesicles exhibiting characteristics of both class 2 and class 3 were examined. One representative vesicle is shown in Figure 3.10A-G, containing small areas of horse-shoe shaped cross-sections similar to class 2 (Figure 3.10A,C, compare to Figure 3.4B), while the majority of the vesicle cross-section resembled class 3 (Figure 3.10B and D, compare to Figure 3.4C). 3D visualization of the vesicle clarified the largely double-membrane nature of the vesicle, apart from a small pore-like opening from the inner NC-containing compartment to the extra-vesicular space (Figure 3.10E arrowhead). The opening consisted of a narrow channel (Figure 3.10F-G arrowheads) with a single NC present inside the opening (asterisk in Figure 3.10E-G). The described morphological form represents a logical intermediate between class 2 and class 3, and strikingly resembles the predicted "fusion pore" predicted to occur in the formation of the double-membrane autophagosome. The final step in autophagosome formation is predicted to involve the splitting of a continuous bilayer into two independent bilayers via membrane fission, creating two membrane-bound compartments. This fission event is thought to occur at a transient pore that serves as the last connection between the two compartments and provides an opening to the cytoplasm [228]. While the fusion pore form is purely theoretical and has not been observed in autophagosomes, our observation of curved single membrane structures (class 2), double membrane structures (class 3) and a fusion pore intermediate suggests that class 2 CPVII may close up to become class 3 CPVII.

Apparent intermediates between class 3 and class 4 CPVII were also observed and analyzed in 3D. Tomographic slices through one such vesicle revealed slices resembling class 3 double membrane vesicle (Figure 3.10H), other slices with nearly enveloped virus particles resembling class 4 CPVII (Figure 3.10J), and intermediate slices with NC which appear to be budding into the inner membrane of the vesicle (Figure 3.10I). 3D visualization revealed a single inner compartment with many of the NC in various stages of apparent envelopment, but all still connected to the main compartment (Figure 3.10K, arrowheads). The envelopment of NC on the inner membrane of class 3 CPVII became apparent in 3D and upon close inspection was observed in at least one NC

in most of the class 3 CPVII in the volume. This observation suggested that the double lamellar structure may not be the final end product of Golgi remodeling.

A second intermediate between class 3 and 4 is shown in Figure 3.10 L-O. In the 2D tomogram slices, this vesicle appears to be a bona fide class 4 vesicle; however, upon close inspection and 3D segmentation, connections were visualized between nearly all the enveloped NC present inside the vesicle. Only two of the 23 NC were found to be fully enveloped, with continuous membrane surrounding the NC, and no connections to the membrane of other NC (Figure 3.10L). All other NC showed varying degrees of connectedness, including particles with two NC sharing their surrounding membrane to varying degrees (Figure 3.10M-N). In 3D, the single membrane-bound compartment can be clearly visualized as well as the separation of the fully independent virions (Figure 3.10 O, green segmentation and arrowheads). While this intermediate form makes apparent the ability of inner NC to undergo envelopment, it is unknown whether all virions will undergo the full budding process, including scission of the membrane into independent virions.

Figure 3.10. 3D analysis of intermediate forms between classes 2, 3, and 4 reveals a potential maturation pathway. **(A-B)** Tomographic slices through an intermediate between class 2 and class 3 CPVII. Each z-slice is 3 nm in thickness, with the slice number shown in the lower left corner of each image. The fusion pore is indicated by the white arrowhead in A and C. **(C-D)** Tracing of the vesicle membranes (gold) in A-B and a NC (red sphere) near the fusion pore. **(E-G)** 3D rendering of the vesicle shown in A-D with the fusion pore indicated by a black arrowhead. **(H-K)** Tomographic slices at various z-heights of a CPVII which is intermediate between class 3 and class 4, showing various stages of interior NC envelopment, from moderate amounts of budding (H) to nearly complete envelopment (I-J). White dotted lines delineate areas magnified to the right. **(K)** 3D rendering of the vesicle shown in H-J. **(L-O)** Tomographic slices through a class 4 CPVII containing fully enveloped virus particles (L), dual-cored particles (M), and virus particles connected by membrane (N). **(O)** 3D rendering of the vesicle shown in L-N, illustrating the interconnected nature of the partially-enveloped NC. A fully formed virus particle is indicated by the green segmentation and black arrowhead. **Scale bars:** 50 nm (A) and 200 nm (H,L).

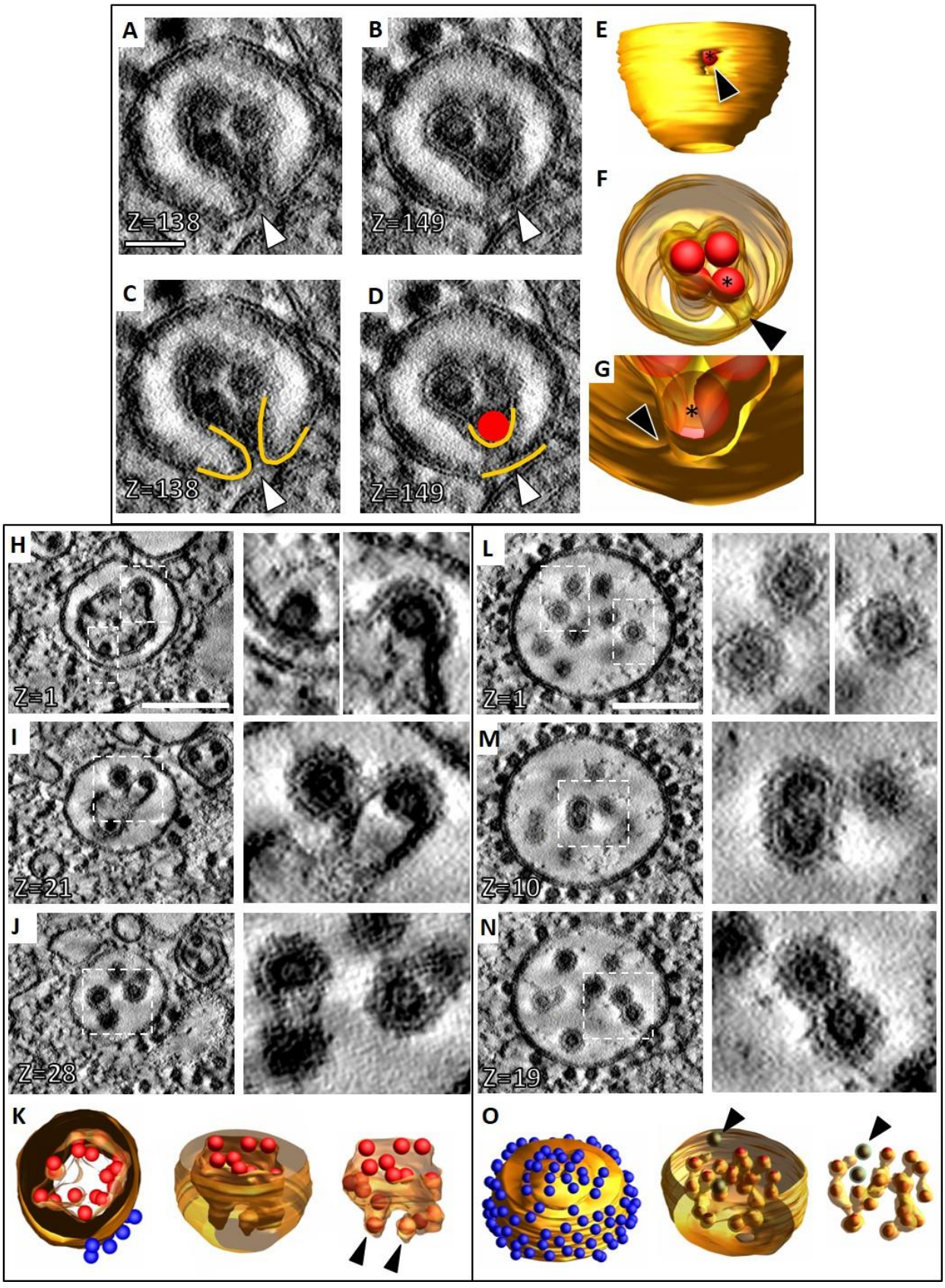
A
B
E
Z=138
Z=149
F
C
D
Z=138
Z=149
G
H
L
Z=1
Z=1
I
M
Z=21
Z=10
J
N
Z=28
Z=19
K
O

3.3.9 All forms of CPVII reach the plasma membrane primarily in clusters

Since our initial 2D screen identified CPVII clusters at the plasma membrane, we collected the second tomographic volume which encompassed the plasma membrane of the cell (Figure 3.3A, red outline). Near the plasma membrane, CPVII are mainly present in clusters (Figure 3.4E and Figure 3.11 A), with two clusters in particular observed in close apposition to the plasma membrane (Figure 3.11 F', H', J). Two representative clusters closer to the Golgi (Figure 3.11B', B-C, and Figure 3.11D', D-E, respectively) and two from the PM (Figure 3.11F', F-G, and Figure 3.11H', H-I, respectively) are shown. Two common features of the clusters stood out regardless of location. First, the clustered CPVII appear to be held together in part if not entirely, by bivalent interactions of NC bound to multiple CPVII (Figure 3.11C, E and G and corresponding insets). This is reminiscent of a similar arrangement of the large CPVII class 1 structures associated with a Golgi cisterna (Figure 3.6C). Secondly, the clusters contain vesicles from all four classes of CPVII, although not in equal numbers. The most abundant classes in these clusters are class 1 (blue) and class 4 (lavender), while class 2 (red) and 3 (gold) vesicles were present more rarely. Compare the visualization in Figure 3.11B,D,F, and H to the graphical representation in Figure 3.4G, with distance from the Golgi being roughly inverse to distance from the plasma membrane.

Next, we searched for any physical contact between the membranes of the CPVII in clusters with the inner leaflet of the plasma membrane. While in this tomogram volume, the clusters came within 50 nm of the PM, none directly made contact (Figure 3.11I, magnification, arrowhead points to the PM, scale bar is 50 nm). Additional small tomograms of the periphery of other cells revealed occasional CPVII that appeared to be in a fused state with the PM (Class 4 CPVII shown in Figure 3.12 A-C). Vesicles were also observed which made direct contact with the PM via a NC bound bivalently to the CPVII cytoplasmic face and the PM (class 3, Figure 3.12 D-F and class 1, G-I). These rare observations provide clues that CPVII, in addition to the widely suspected delivery of NC to the PM for envelopment, may undergo membrane fusion with the PM, consequently delivering the luminal payload of enveloped viruses or even the inner vesicular structures containing NC, to the extracellular space. These morphological observations provide a broad platform from which to ask additional questions and guide further investigation into the function and significance of these CPVII forms.

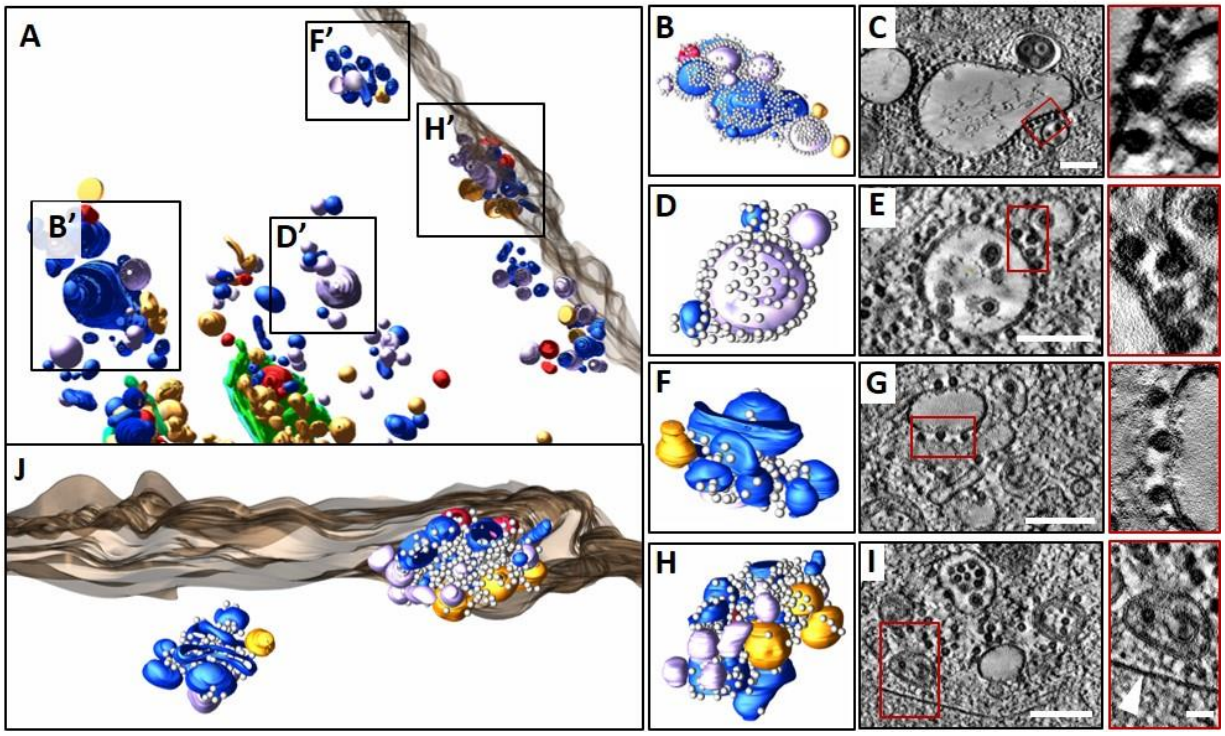

Figure 3.11. All forms of CPVII reach the plasma membrane primarily in clusters. **(A)** Overview of part of the volume near the plasma membrane, with segmented Golgi cisternae (green), CPVII color-coded by class (blue, red, gold, lavender), and plasma membrane (translucent grey). **(B-I)** Segmentation and a tomographic slice through CPVII clusters with locations indicated by B', D', F', and H' in panel A. Magnification of the red outlined regions in C, E, G, and I show the NC at the interface between the vesicles in the clusters. **(J)** Top-down view of CPVII clusters in F and H, showing their proximity to the plasma membrane. **Scale bars**: 200 nm (C, E, G, I) and 50 nm (I inset).

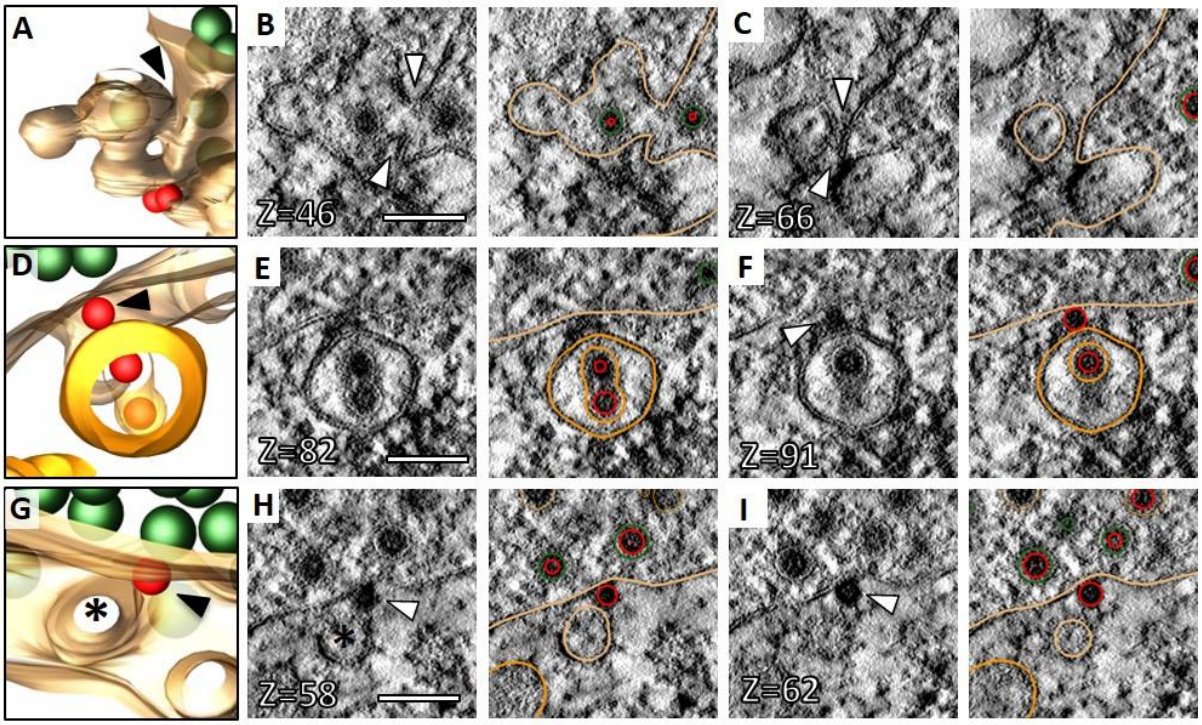

Figure 3.12. CPVII forms involved in potential fusion events at the plasma membrane **(A-C)** 3D rendering and tomographic slices through different z-heights of a CPVII in apparent state of fusion with the plasma membrane. Black arrowhead in A indicates the continuity between the vesicle membrane and the plasma membrane. White arrowheads in B indicate a neck-like area of fusion with the plasma membrane, and in C, the same area at a different z-height where the vesicle and plasma membrane are separated. **(D-F)** A CPVII with a dual-cored virus particle inside, bound to the plasma membrane by an external NC. Arrowheads in D and F show the NC simultaneously bound to the plasma membrane and the CPVII membrane. **(G-I)** A CPVII with an outer NC in the initial stages of budding through the plasma membrane (arrowheads). **Scale bars:** 100 nm

3.4 Discussion

In this work, we outlined a novel morphological pathway of pathogenic conversion of Golgi into cytopathic vesicles by an alphavirus. Results from our work challenge the long standing belief that intracellular budding in alphaviruses is exclusive to arthropod hosts, while in mammalian cells budding takes place only at the plasma membrane. Using high resolution electron tomography and a high resolution marker study, we provide evidence that VEEV, an encephalitic alphavirus, exhibits *bona fide* intracellular budding in mammalian cells. Our 2D EM and marker study established the fact that the fragmented Golgi could be resolved into distinct morphological classes of cytopathic vesicles. Large volume electron tomography revealed the complexities of these

vesicles and that the different classes were in fact intermediates of the same morphological pathway that results in the intracellular budding of nucleocapsid cores.

Prior work in the field employed traditional thin-section EM and was able to identify the unique NC-studded CPVII structure[172], [174], [176]. However, the information obtained from these studies by the discrete and limited sampling of membrane could not establish the direct relationship of the cytopathic vesicles (CPVII) with the Golgi apparatus. We hypothesized that since the CPVII phenomenology is usually identified by the detection of NC-bound vesicles, early perturbation of the Golgi ultrastructure leading up to its formation may have gone undetected. Thus, to detect these putative early changes and to determine the relationship of CPVII with the Golgi apparatus, we carried out HRP-tagged marker studies employing a recently published method for superior sample preservation during localization of peroxidase tagged proteins [225], [227]. Results from this marker assay demonstrated that the prevalent forms of CPVII observed by our 2D screen carried the Golgi marker. However, two things were apparent from our thin-section 2D analysis; first, the Golgi apparatus begins to lose its cisternal architecture via widespread herniations and vacuolization leading to the formation of large pleomorphic vesicles as early as 3 hours post-infection. Second, thicker serial sections showed that CPVII form large clusters that could have extensive connections with each other and may not all be isolated vesicles as previously thought[172], [176]. To this end we employed serial section tomography of a large cellular volume to reconstruct the Golgi complex in flux. Multiple serial sections of cells were screened from a late timepoint (12 hour) and two large (overlapping) tomograms from a representative cell were collected. Montaging was deemed necessary in order to achieve the resolution necessary to detect delicate membrane connections between CPVII intermediates and the Golgi apparatus.

Segmentation and 3D visualization of the first tomogram not only corroborated our observations from the marker study and thin section analysis, but also revealed a number of intriguing observations that were not detectable in our extensive 2D screen. First, almost all CPVII lying in close proximity to the Golgi apparatus were physically connected to it and/or connected to each other. Second, various sections of the Golgi apparatus also exhibited intermediate structures with both cisternal and vesicular characteristics. Based on the 3D data, four morphologically distinct classes of CPVII were identified. To obtain an idea on the subcellular distribution of these four

classes of CPVII, we analyzed the occurrence of each CPVII class as a function of its distance from the Golgi. It was observed that both class 1 and class 4 have considerable presence both at the Golgi and at the plasma membrane. However, as the distance from Golgi increases, the number of class 2 and 3 CPVII observed decreased drastically. While there could be multiple explanations for this result, one intriguing possibility would be that Class 2 and 3 could be precursor forms for class 1 or class 4. We hypothesize that as the intermediates move away from the Golgi over time, they convert to the more mature CPVII.

Thus, the next logical step was to carefully analyze multiple examples of each of these subclasses to look for intermediate forms that show characteristics of two or more classes. The first tomogram covered a large subcellular volume consisting of multiple Golgi stacks that show a systematic disintegration. In order to visualize Golgi remodeling, our analysis progressed outward step by step from *trans*-most intact cisternae. Although the exact players in the biogenesis of these cytopathic vesicles remain unknown, results from the Golgi marker studies indicate direct transformation of Golgi cisternae into vesicles of different sizes occurs via Golgi herniations and vacuolization. This observation was also substantiated by the 3D reconstruction of large CPVII closely associated with the Golgi trans-cisterna (Figure 3.6). The other type of Golgi remodeling distinct from the former, results in CPVII class 2, 3 and 4. We provide structural evidence that this second type originates from the bending and curling of intact Golgi cisternae. Several stages of this transformation were seen. Transitional intermediates of various sizes exhibiting part cisternal and part double membrane vesicular characteristics on the Golgi further substantiates this initial phase of the proposed morphological pathway (Figure 3.10).

Further away from the Golgi apparatus, independent CPVII were analyzed in 3D for putative links. Intriguingly, many of these vesicles that at first appeared to be Class 2, 3 and 4 CPVII were found to exhibit characteristics of two classes simultaneously. The ultrastructural evidence points to Class 2 as the precursor of class 3 (Figure 3.10). A morphological intermediate between class 2 and 3 that has been suggested to be pivotal in the transitioning of membrane sheets into double lamellar vesicles such proposed in the formation of autophagosome (Figure 3.10A-G). These intermediates seem to have been captured at a stage just prior to formation of CPVII class 3 end to end fusion giving rise to *bona fide* class 3 double lamellar CPVII. These vesicles may possibly

undergo membrane fission as envisioned for the final step in the formation of autophagosomes as per the “fission hypothesis”[228]. This characteristic of bent Golgi cisternae to form double membrane vesicles by end to end fusion resulting in lipid rearrangement and membrane fission to create a compartment within a compartment has also been recently reported in brain tissue, where these Golgi structures function as a degradosomes [229].

The morphological relationship between class 3 and class 4 is the most intriguing of all. Figure 8H-K shows a typical example of such a transitional CPVII that were in some of the 2D slices. This resembles class 3 CPVII where the NC are just bound to the inner membrane without any visible distortion of the membrane or budding. However, advancing through the z-slices for the same CPVII, it becomes apparent that the inner membrane at the point of contact with the NC exhibits bending consistent with various stages of alphavirus NC budding or envelopment. This observation led us to carefully examine the luminal content of Class 4 that apparently contains fully enveloped virions (Figure 3.10 L-O). To our surprise, we observed that while some of the class 4 CPVII had independent virions, others were connected to each other via intact bilayers indicating that their envelopment was incomplete at the time of cryofixation. Thus, our model proposes that Classes 2, 3 and 4 CPVII are all intermediates of the same morphological pathway that gives rise to intracellular enveloped virions during VEEV infection in mammalian cells (Figure 3.13).

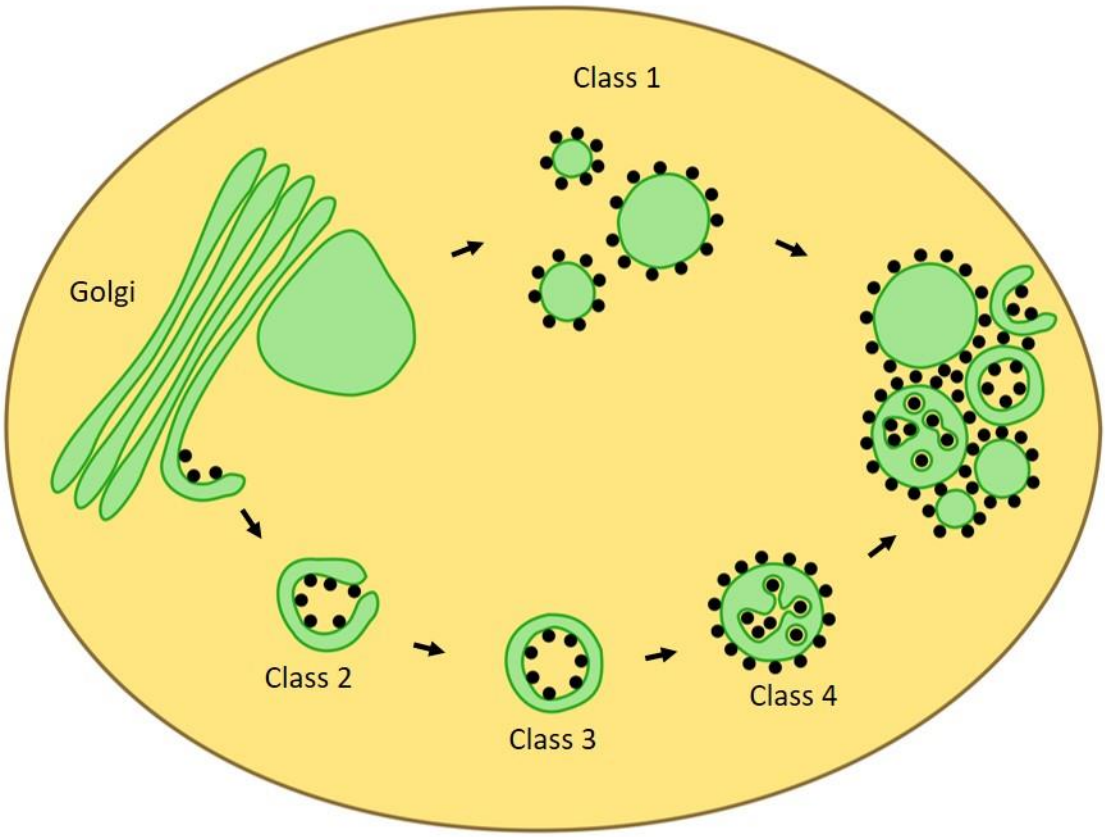

Figure 3.13. Electron microscopy and tomography based model of CPVII formation from the Golgi apparatus, maturation, and clustering at the plasma membrane. This morphological model illustrates two potential mechanisms of formation of CPVII from the Golgi. Class 1 forms from herniated Golgi, which may break down into the smaller single-membrane vesicles that are predominantly observed. The double-membrane CPVII forms originate from curling of Golgi in the presence of NC. Class 2 are cup-shaped intermediates in which the vesicle has not completely closed. Class 3 consists of completely closed double-membrane vesicles, and Class 4 have some degree of virus envelopment. All four classes of vesicles are observed in clusters, seemingly bound together by NC bound simultaneously to more than one vesicle. Clusters are observed in close proximity to the plasma membrane, and the various classes of vesicles have the potential to fuse with the PM allowing for the release of intracellularly enveloped virions as well as envelopment of the NC at the PM.

To gain further insight in this intracellular envelopment in alphaviruses, we looked into the potential for virus envelopment via this process. To this end, the surface areas of the inner compartment of Class 3 CPVII were measured and the number of NCs inside were counted to determine if there is enough membrane for the internal NCs to become fully enveloped. We approximated that 5000 nm^2 (dotted line, Figure 3.14A) of membrane is required to envelope each NC (approximation based on a 40 nm diameter of NC). For class 3 CPVII, we plotted the lumenal membrane surface area available per NC versus the percent of NC that were undergoing potential

budding. For each NC bound to the inner membrane, budding was determined as before based on the radius of curvature of the membrane at the point of attachment (Figure 3.8). In general, the more membrane available, the more NC exhibited budding; however, 53% of the CPVII (9/17) did not have sufficient membrane to envelope all internal NCs (Figure 3.14A). Thus, it is estimated that half of all NC inside double lamellar CPVII could not become fully enveloped virus.

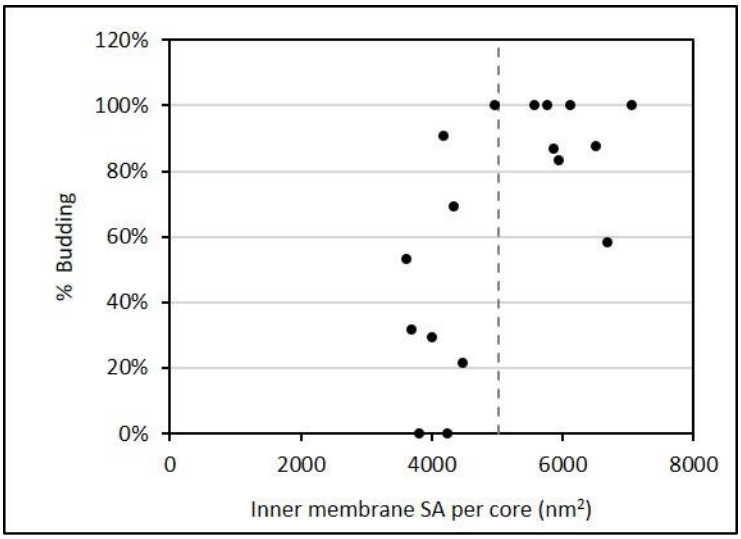

Figure 3.14. Budding potential for NC in class 3 CPVII assessed by available surface area. The inner membrane surface area for class 3 CPVII were calculated from their segmented volumes and the surface area per NC in each vesicle was determined. Percent budding for each CPVII was calculated as the fraction of inner NCs located on curved membrane, per the radius of curvature criteria as described in Figure 3.8. For each vesicle, the percent of NC budding was plotted against the inner membrane SA available per NC. The dashed line represents the 5000 nm^2 per NC (conservative estimate based on a 40-nm capsid) required to envelope every NC in the vesicle. Points to the left of the line thus represent CPVII which do not contain enough membrane surface area to fully envelope each NC they contain.

The large volume of the cell analyzed provides us some unique perspectives on the CPVII system**.** One salient feature of the CPVII that is apparent in our tomographic volume is that they can exist in clusters and they do so extensively near the plasma membrane. At the Golgi, these clusters can be connected via membrane connections as they often are parts of the same cisternae. Further away from the Golgi and at the PM the clusters composed of mostly of discrete vesicles held together by NC on their outer membranes via bivalent interactions (Figure 3.11)**.** Importantly, clustering could potentially bring together all the structural proteins critical for virus budding on one platform at the PM. Recent evidence indicates that budding at the PM occurs from E2-rich patches on the plasma membrane as discerned by light microscopy using Sindbis virus carrying GFP-tagged E2[230]. There is a strong possibility that these clusters that we describe here are in fact the

fluorescent patches seen at light microscopy resolution. We observe that although some of these CPVII clusters were located at a very close vicinity of the inner leaflet of the PM, we could not capture a significant number of CPVII in our tomographic volume that made contact with the PM. However, two examples of PM proximity were detected, where one appears to be a fusion event while another a NC on a CPVII made direct contact with the PM (See Figure 3.12). The rarity of fusion events observed in our 2D and 3D analysis could either be due to the fact that the process is very fast or the CPVII clusters do not really fuse but smaller vesicles emanating from it transport E2 and NC from a very close vicinity making the process very efficient.

The phenomenon of remodeling of the Golgi apparatus to induce CPVII formation is essentially an example of pathogen induced Golgi fragmentation. Golgi fragmentation is a phenomenon seen in endogenous events like mitosis, apoptosis, and also in certain cancers and neurodegenerative diseases[231]–[235]. Interestingly, it is also seen in MDCK cells that secrete human growth hormone, in differentiated muscle cells, and in other cell types as an adaptation to increased level of synthesis of certain proteins[236], [237]. Secretory demands of cells that require secretory Golgi outposts to be transported to close proximity to site of cargo delivery at the PM as possible [238]. Additionally, uroplakin transport in urothelial cells is mediated by fragmented Golgi that forms secretory Golgi outposts at the PM for efficient secretion of the protein [239], [240]. Thus recent evidence indicate that this fragmented state of Golgi could be an endogenous cellular program that could be activated by the cell as a response to specific cargo and its demands. Thus the alphavirus CPVII clusters at the PM could be an example of virus subversion of this program to induced secretory outposts that functions to meet the elevated level of structural protein transport to PM for budding.

This novel pathway of intracellular budding that we report here has some unique aspects that are distinct from other viruses that acquire their envelope from the Golgi apparatus. Viruses that exit via the Golgi usually bud into herniated cisternae as well as Golgi derived vacuoles that are thought to transport the virions to the PM for exocytic release[241], [242] (illustrated in Figure 3.15 A-B). However in VEEV, we neither see virions in the lumen of the cisternae nor NC budding into any of the forms of CPVII from their cytoplasmic surfaces. Instead envelopment takes place on the luminal wall of the Golgi derived double lamellar vesicles (DLV). Envelopment was not observed

on the bent cisternae before they transform into the DLV. A number of mechanistic hypothesis could be forwarded to explain this phenomenon, centering around the E2 glycoprotein and the NC and potentially their interaction. Work with bunyavirus glycoproteins has shown that viral glycoproteins by themselves can remodel and bend membranes and vacuolate the Golgi [218]. It is also possible that the intrinsic architecture of the Golgi could be a contributor. Recent work using cryo-electron tomography has shown that the flatness of the cisternae is due to the presence of closely spaced yet unidentified luminal proteins that zipper the membranes together into close apposition (18-19 nm) in the compact zone of the GA [243]. The availability of the glycoproteins in the cisternal membrane leads to indiscriminate binding of the NC. Once the membrane associated E2 engages with the NC, it is possible that forces that otherwise induce budding into herniated Golgi lumen ends up bending the zippered double lamellar structure of the cisternae due to architectural constraints (Figure 3.15 B-C). To this end we measured and compared the luminal width of a typical cisternae and DLVs with or without detectable budding events. The results indicate that budding events were always associated with increased luminal width (herniations) indicating that the Golgi architecture may play a role in this unique phenomenology in alphaviruses (Figure 3.15 E-K).

In summary, our work fills a number of outstanding gaps in the cellular pathology of this highly pathogenic group of viruses. First, using a HRP-tagged Golgi marker, we confirm that all forms of CPVII so far detected by us and others in the field, are in fact remodeled Golgi cisternae. Based on this finding we use serial-section ET to collect two large overlapping tomograms from a representative infected cell to reconstruct the intermediates of this Golgi conversion pathway. We propose a model for step-by-step morphological breakdown of the Golgi apparatus and its conversion into various intermediate forms of CPVII via membrane remodeling. Our model proposes that all forms of CPVII, despite their Golgi origin, are not the product of the same morphological pathway. We further show that alphaviruses undergo *bona fide* intracellular envelopment within the lumen of double lamellar CPVII that reach the PM in clusters held together with NC bound to their surface.

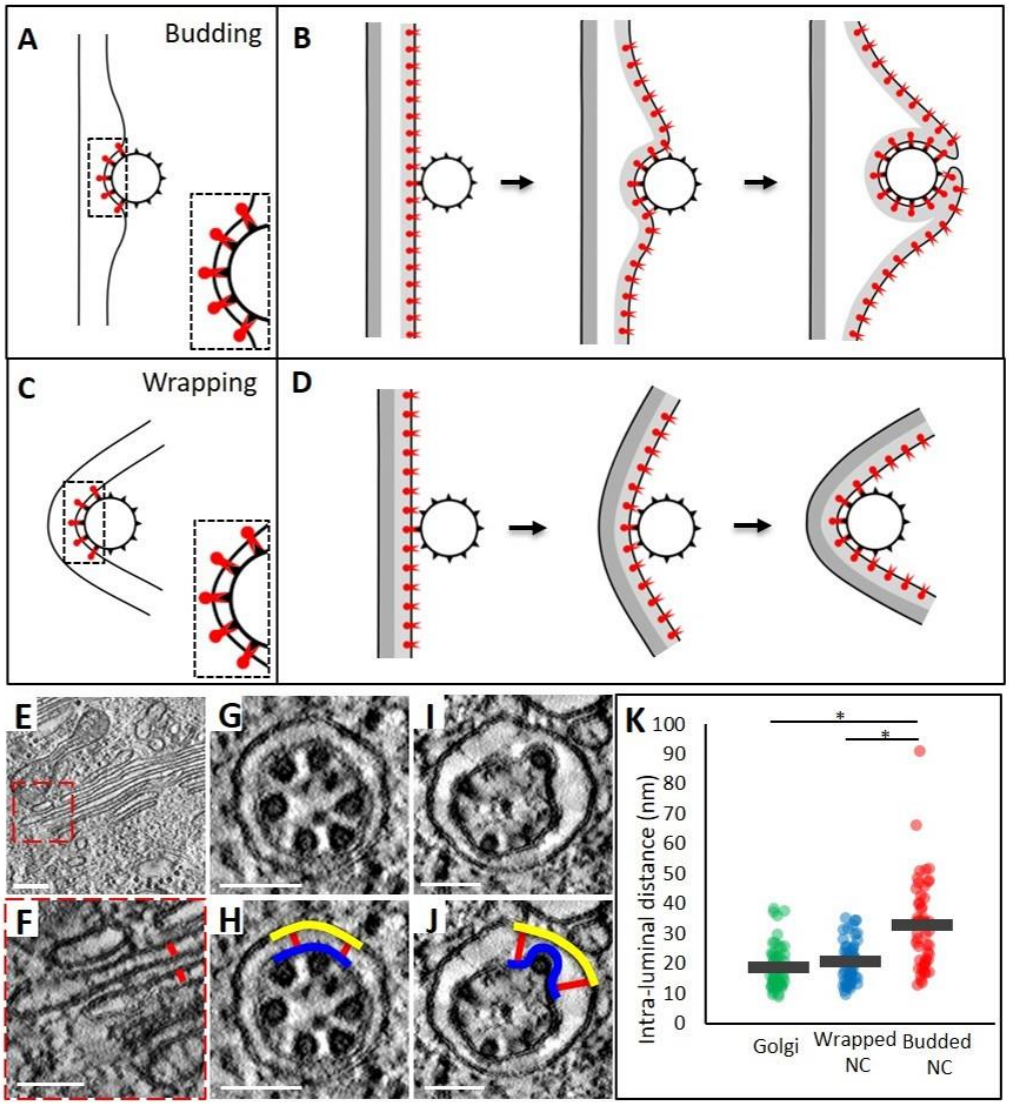

Figure 3.15. Model for the structure or state of the GA that determines whether DMV forms as a result of cisternal wrapping around the NC or canonical budding into the cisternal lumen. (A-B) Budding events could be explained as NC-glycoprotein interactions in a non-compact region of the Golgi, leading to displacement of the NC into the cisternal lumen. **(C-D)** Wrapping events could occur when interaction between the NC binding domains (black triangles) with the viral glycoproteins (red) occurs at the compact region of the GA (indicated by tightly apposed grey lines).**(E-K)** Measurement of the intra-luminal distance of Golgi cisternae (E-F) and double-membrane CPVIIs **(G-J)** from 3-nm thick tomographic slices. **(E)** Tomographic slice of a region of a Golgi stack with no signs of infection (no bound NC or signs of herniation or fragmentation into CPVII). **(F)** Close-up of two cisternae with red lines indicating the intra-luminal distance in the compact region of the Golgi. **(G-J)** Intra-luminal distance (red) of CPVIIs was measured as the distance between the outer (yellow) and inner (blue) membranes 40 nm to either side of the center of an attached NC. NCs were categorized as "budded" or "wrapped" based on whether the two membranes were parallel (wrapped, G-H) or not parallel (budded, I-J). **(K)** Comparison of intra-luminal distance in intact Golgi cisterna with that of class 3 CPVII for wrapped and budded NC. At least 60 measurements were taken for each of the three groups. Asterisks indicate $p < 0.0001$ using the Mann-Whitney U test. **Scale bars:** 200 nm (E) and 100 nm (F-J).

CHAPTER 4. THE CRYOAPEX METHOD FOR ELECTRON MICROSCOPY ANALYSIS OF MEMBRANE PROTEIN LOCALIZATION WITHIN ULTRASTRUCTURALLY PRESERVED CELLS

A version of this chapter has been published as the following journal article: [227]. *The ET work has been published in the following journal article:* [225].

Key cellular events like signal transduction and membrane trafficking rely on proper protein location within cellular compartments. Understanding precise subcellular localization of proteins is thus important for answering many biological questions. The quest for a robust label to identify protein localization combined with adequate cellular preservation and staining has been historically challenging. Recent advances in electron microscopy (EM) imaging have led to the development of many methods and strategies to increase cellular preservation and label target proteins. A relatively new peroxidase-based genetic tag, APEX2, is a promising leader in cloneable EM-active tags. Sample preparation for transmission electron microscopy (TEM) has also advanced in recent years with the advent of cryofixation by high pressure freezing (HPF) and low-temperature dehydration and staining via freeze substitution (FS). HPF and FS provide excellent preservation of cellular ultrastructure for TEM imaging, second only to direct cryo-imaging of vitreous samples. Here we present a protocol for the cryoAPEX method, which combines the use of the APEX2 tag with HPF and FS. In this protocol, a protein of interest is tagged with APEX2, followed by chemical fixation and the peroxidase reaction. In place of traditional staining and alcohol dehydration at room temperature, the sample is cryofixed and undergoes dehydration and staining at low temperature via FS. Using cryoAPEX, not only can a protein of interest be identified within subcellular compartments, but also additional information can be resolved with respect to its topology within a structurally preserved membrane. We show that this method can provide high enough resolution to decipher protein distribution patterns within an organelle lumen, and to distinguish the compartmentalization of a protein within one organelle in close proximity to other unlabeled organelles. Further, cryoAPEX is procedurally straightforward and amenable to cells grown in tissue culture. It is no more technically challenging than typical cryofixation and freeze substitution methods. CryoAPEX is widely applicable for TEM analysis of any membrane protein that can be genetically tagged.

4.1 Introduction

Biological studies often include questions of resolving subcellular protein localization within cells and organelles. Immunofluorescence microscopy provides a useful low-resolution view of protein localization, and recent advances in super-resolution imaging are pushing the bounds of resolution for fluorescently tagged proteins[244]–[246]. However, electron microscopy (EM) remains the gold standard for imaging high-resolution cellular ultrastructure, though the labeling of proteins is a challenge.

Historically, several EM methods have been used to approach questions of ultrastructural protein localization. One of the most commonly utilized methods is immunoelectron microscopy (IEM), where antigen-specific primary antibodies are used to detect the protein of interest. EM signal is generated by the application of secondary antibodies conjugated with electron-dense particles, most commonly colloidal gold[247], [248]. Alternately, antibodies conjugated with enzymes such as horse radish peroxidase (HRP) can be used to produce an electron-dense precipitate[249]–[251]. Two main approaches exist for IEM, termed pre-embedding and post-embedding labeling. In pre-embedding IEM, antibodies are introduced directly into cells, which necessitates light fixation and permeabilization of the cells[252]–[254]. Both steps can damage ultrastructure[255], [256]. Development of significantly smaller antibodies consisting of an antibody Fab fragment conjugated with 1.4-nm nanogold allows very gentle permeabilization conditions to be used; however, nanogold is too small for direct visualization under TEM and requires additional chemical enhancement steps to become visible[257]–[259]. In post-embedding IEM, antibodies are applied on thin sections of cells which have been fully processed by fixation, dehydration, and embedding in resin[260]. While this approach avoids the permeabilization step, preserving the epitope of interest throughout sample preparation is challenging[261]–[263]. The Tokuyasu method of light fixation followed by freezing, cryo-sectioning, and antibody detection provides improved epitope preservation[264], [265]. However, the technical requirements of cryo-ultramicrotomy, as well as the sub-optimal contrast achieved in the cell, are disadvantages[266].

The use of genetically encoded tags eliminates many of the difficulties of IEM related to detection of the protein of interest. A variety of tags are available, including HRP, ferritin, ReAsH, miniSOG, and metallothionein[267]–[275]. Each of these has advantages over previous methods, but each

also has drawbacks preventing widespread use. These drawbacks range from inactivity of HRP in the cytosol to the large size of the ferritin tag, light sensitivity of ReAsH, and small size and lack of compatibility with cellular staining of metallothionein. Recently, a protein derived from ascorbate peroxidase has been engineered as an EM tag, named APEX2[276], [277]. As a peroxidase, APEX2 can catalyze the oxidation of 3,3' diaminobenzidine (DAB), producing a precipitate that reacts with osmium tetroxide to provide local EM contrast with minimal diffusion from the protein of interest (less than 25 nm)[224], [276]. Unlike traditional HRP-based methods, APEX2 is extremely stable and remains active in all cellular compartments[276]. Samples can be processed for TEM using traditional EM sample staining and methods that allow good visualization of the surrounding structures[276]–[278]. Because of its small size, stability, and versatility, APEX2 has emerged as an EM tag with great potential.

Many of the approaches discussed above either cannot be or have not yet been combined with the current state of the art in ultrastructural preservation, cryofixation and low-temperature freeze-substitution. Thus, they suffer from a lack of membrane preservation and/or cell staining to determine accurate protein localization. This necessarily limits the resolution and interpretation of the data that can be obtained. Cryofixation by high pressure freezing (HPF) involves rapid freezing of samples in liquid nitrogen at a high pressure (~2100 bar), which causes vitrification rather than crystallization of aqueous samples, thus preserving cells in a near-native state[279]–[281]. HPF is followed by freeze substitution (FS), a low temperature (-90 °C) dehydration in acetone combined with incubation with typical EM stains such as osmium tetroxide and uranyl acetate. HPF and FS together provide a distinct advantage over traditional chemical fixation (a longer process which can lead to artefacts) and alcohol dehydration at room temperature or on ice (which can lead to extraction of lipids and sugars), and thus are desirable to combine with the best EM tags for protein detection.

One reason that HPF/FS has not been combined with APEX2 labeling is that light chemical fixation is a prerequisite for the peroxidase reaction, limiting the diffusion of the DAB reaction product. In APEX2 studies thus far, fixation and peroxidase reaction are followed by traditional EM methods for staining and alcohol dehydration[276], [278]. However, it has been shown that following chemical fixation with HPF/FS provides a distinct advantage in preservation over

traditional chemical fixation and alcohol dehydration alone[282]. The loss of ultrastructural integrity seen in traditional TEM samples appears less connected to fixation than to dehydration, which is typically done using alcohol at room temperature or on ice, and can lead to extraction of lipids and sugars[282], [283]. To develop the cryoAPEX method, we hypothesized that chemical fixation and peroxidase reaction, followed by HPF and FS, would produce an optimal result in terms of ultrastructural preservation.

Here we present the cryoAPEX protocol, which combines APEX2 tagging with cryofixation and freeze substitution methods (Figure 4.1). This straightforward protocol consists of transfection of an APEX2-tagged protein of interest, chemical fixation of cells, and the peroxidase reaction. HPF and FS are then performed followed by typical resin embedding and thin sectioning. TEM imaging reveals excellent preservation of ultrastructure using this method. Additionally, high-resolution subcellular localization and spatial distribution of an endoplasmic reticulum (ER) lumenal protein were observed. This method is widely useful for detection of membrane protein localization within cells for electron microscopy analysis. In our hands, the method has worked successfully for a variety of cell lines grown in tissue culture, including HEK-293T (human embryonic kidney), HeLa (human cervical cancer), Cos7 (African green monkey kidney fibroblast), and BHK (baby hamster kidney). Detailed instructions are described below using HEK-293T cells.

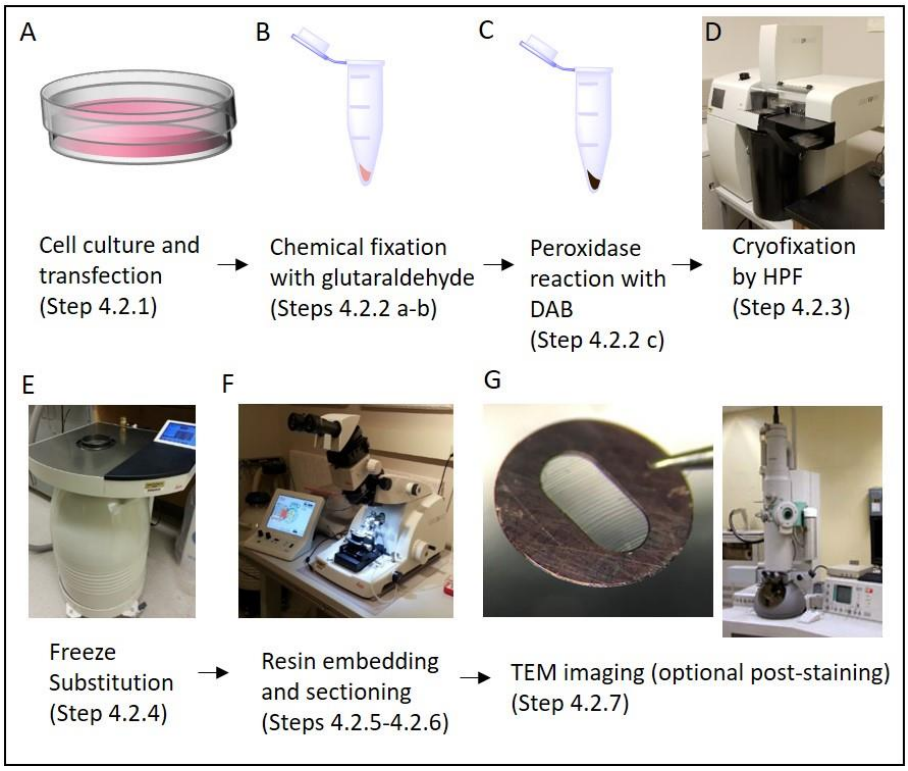

Figure 4.1. Schematic of the essential steps in the CryoAPEX protocol. (A) Cells are grown and transfected with an APEX2 plasmid. (B) Cells are pelleted and fixed with glutaraldehyde, followed by (C) incubation with DAB and hydrogen peroxide to produce the peroxidase reaction product. (D) The pellet is cryofixed by HPF, (E) freeze substituted with heavy metals and acetone, and (F) embedded in resin. Thin sections are collected on the microtome. (G) TEM imaging is performed and additional contrast may be added by post-staining.

4.2 Protocol

4.2.1 Cell culture and transfection

a. Seed HEK-293T cells on a 60 mm diameter or larger tissue culture dish and grow to 60%–90% confluence in a cell culture incubator at 37 °C and 5% CO_2.

b. Transfect cells with APEX2-tagged mammalian expression plasmids using transfection reagent according to the manufacturer's directions.

c. At 12-15 h post-transfection, wash cells once with phosphate buffered saline (PBS). Remove cells from the dish by gentle washing with PBS. A dissociation reagent such as trypsin may be used if required for a given cell type. Centrifuge at 500 x *g* for 5 min to form a pellet.

4.2.2 Chemical fixation and peroxidase reaction

a. Carefully remove the supernatant and resuspend the pellet in 2 mL of 2% glutaraldehyde (v/v) in 0.1 M sodium cacodylate buffer, pH 7.4, at room temperature. Place sample on ice and incubate for 30 min. Pellet the sample at 500 x *g* for 5 min at 4 °C. From this point until step 4.2.2 c-iii, keep the sample and solutions on ice, and perform centrifugation at 4 °C.

   CAUTION: Both glutaraldehyde and sodium cacodylate buffer (containing arsenic) are toxic. Proper safety procedures and personal protective equipment should be used during handling. Solutions containing glutaraldehyde and/or sodium cacodylate buffer should be disposed of as hazardous chemical waste.

b. Wash the pellet 3x for 5 min with 2 mL of 0.1 M sodium cacodylate buffer. For these as well as subsequent washes, gently resuspend the cell pellet in the required solution, then centrifuge for 5 min at 500 x *g* and carefully remove and discard the supernatant. Care should be taken with the repeated pelleting and resuspension steps, in order to minimize sample loss.

c. Carry out the peroxidase reaction

   i. Prepare a fresh solution containing 1 mg/mL of 3,3'-diaminobenzidine tetrahydrochloride (DAB) in 0.1 M sodium cacodylate buffer. Dissolve the DAB by vigorous vortexing for 5–10 min.

      CAUTION: DAB is toxic and a potential carcinogen and should be handled with proper safety procedures and personal protective equipment. Solutions containing DAB should be treated as hazardous chemical waste.

   ii. Wash pellet by resuspending in 3 mL of DAB solution followed by pelleting at 500 x *g* for 5 min.

   iii. Resuspend the pellet in 3 mL DAB solution to which hydrogen peroxide has been added to achieve a final concentration of 5.88 mM. Incubate for 30 min at room

temp. The pellet becomes visibly brown-colored indicating the presence of the insoluble DAB reaction product.

NOTE: The DAB incubation time may need to be optimized for each sample. The color change can be monitored on the light microscope. In our experience, a 15–45 minute incubation is adequate for most proteins. Hydrogen peroxide should be obtained from a freshly opened bottle or one that has been kept well-sealed after opening.

iv. Pellet the cells, then wash 2x for 5 min with 0.1 M sodium cacodylate buffer, followed by one wash in Dulbecco's modified Eagle's medium (DMEM) or cell media of choice.

d. Resuspend the cell pellet in 500 µL of a cryo-protectant solution of DMEM (or other cell media of choice) containing 10% fetal bovine serum and 15% bovine serum albumin. Pellet again, slightly increasing the centrifuge speed from 500 x *g* if required to achieve a pellet in the thick cryo-protectant solution. Discard the majority of the supernatant, ensuring that enough liquid is left so that the pellet will not dry out. Transport the cell pellet to the high pressure freezing instrument.

4.2.3 High pressure freezing

a. Fill the high-pressure freezer reservoir with liquid nitrogen (LN_2) and start the pump to fill the sample chamber with LN_2.

CAUTION: Use proper safety procedures and personal protective equipment when working with liquid nitrogen.

NOTE: These steps are specific to the Leica EMPACT2 high pressure freezer.

b. Wick away any remaining liquid from the cell pellet using the corner of a laboratory wipe or paper towel. Enough liquid should remain that the pellet forms a loose paste. It should be thin enough to be aspirated into a 20 µL pipet tip.

c. Aspirate 2-3 µL of the cell pellet and deposit it onto a membrane carrier. Fill the well of the membrane carrier completely, so that the surface tension creates a slight dome on top, but the liquid does not spill out of the well. No air bubbles should be present.

d. Slide the membrane carrier into the cartridge and secure. Place the cartridge into the HPF machine that has been prepped and primed, and press **Start** to freeze.

e. Inspect the temperature vs. time and pressure vs. time graphs to verify that the pressure reached 2100 bar and the temperature reached -196 °C within 200 ms, and both parameters remained steady for the 600 ms of measurement.

f. Repeat steps c to e until the cell pellet has been used or the desired number of samples has been frozen.

g. Keeping the cartridges immersed in LN_2, remove each membrane carrier from its cartridge, place into a plastic capsule, and place the plastic capsule into a cryo-vial full of LN_2.

NOTE: The protocol may be paused here. The cryo-vials with samples can be stored in a LN_2 dewar in cryo-canes or cryo-boxes.

4.2.4 Freeze substitution

CAUTION: Use proper safety procedures and personal protective equipment when working with liquid nitrogen. Additionally, many of the chemicals utilized in step 4.2.4 are toxic, including tannic acid, osmium tetroxide, and uranyl acetate. These chemicals must be handled according to proper safety procedures and disposed of as hazardous chemical waste.

a. Fill the automated freeze substitution unit with LN_2. Bring the temperature to -90 °C.

b. Prepare FS Mix 1 and begin FS.

    i. In a chemical hood, prepare a solution of 0.2% tannic acid (w/v) and 5% DI water in acetone and aliquot 1 mL per sample into cryo-vials. Place into LN_2 to freeze.

    ii. Place the FS Mix 1 vials and the cryo-vials containing the frozen cell pellets into the FS unit's sample chamber. Transfer the inner capsule containing the membrane carrier from the LN_2 vial into the corresponding vial containing FS Mix 1.

    iii. Start a FS protocol with its first step being 24 h at -90°C. After the 24 h, pause the FS, and wash the samples 3x for 5 min with acetone that has been cooled to -90 °C.

c. Prepare FS Mix 2 and complete FS.

    CAUTION: Osmium tetroxide is a highly toxic and oxidizing chemical that should only be handled by trained individuals according to established safety protocols. Protocols for the storage and disposal of osmium-containing solutions must be followed, as well as labeling of lab areas where osmium tetroxide is in use. Osmium tetroxide should be handled in a chemical hood with personal protective equipment including eye protection, a lab coat providing full arm protection, double Nitrile gloves, and an optional respirator.

    i. In a chemical hood, prepare a solution of 1% osmium tetroxide, 2% uranyl acetate, and 5% DI water in acetone. Aliquot 1 mL per sample into cryo-vials and place in LN_2 to freeze.

        NOTE: Stock solutions of tannic acid (10% w/v in acetone), osmium tetroxide (10% w/v in acetone) and uranyl acetate (8% w/v in methanol) may be prepared and stored in cryo-vials in a LN_2 dewar for ease of preparation of FS Mixes.

ii. Place the cryo-vials with FS Mix 2 into the FS unit and transfer the capsules from the third acetone wash into the FS Mix 2 vials. Incubate in FS Mix 2 for 72 h at -90 °C, followed by gradual warming to 0 °C over 12-18 h.

d. Keep the temperature at 0 °C and wash 3x for 30 min with pre-cooled acetone from a freshly opened bottle.

4.2.5 Resin infiltration and embedding

CAUTION: Durcupan resin is toxic prior to polymerization and should be handled with proper safety procedures and personal protective equipment. Any unpolymerized resin should be disposed of as hazardous chemical waste.

a. Infiltrate the samples with increasing concentrations of resin dissolved in acetone from a newly opened bottle. Prepare a mixture of resin components A, B, and D in a plastic beaker according to the manufacturer's directions, and incubate samples in the following resin concentrations: 2%, 4%, and 8% for 2 h each at 0 °C. Incubate in 15%, 30%, 60%, 90%, and 100% resin for 4 h each at room temperature. Incubate for 4 h in a mixture of components A, B, C, and D.

b. Place the membrane carriers with cell pellet side up into flat embedding molds and fill with resin (A, B, C, and D). Paper labels for the samples can be added to the wells at this time.

c. Polymerize in an oven at 60 °C for 24-36 h.

NOTE: The protocol can be paused after the polymerization.

d. Remove the blocks from the mold and let cool. To remove the membrane carrier, first place the sample in the vertical chuck of the ultramicrotome where it can be visualized with magnification. Separate the membrane carrier from the block by a combination of dabbing liquid nitrogen on the membrane carrier to separate the metal from the plastic, and using a razor blade to chip away the resin around the membrane carrier. When separated, gently lift away the membrane carrier leaving the cell pellet dome on the face of the block.

e. Place the block with the exposed cell pellet facing upward in a flat embedding mold that is slightly deeper than the first mold, and fill with resin. Polymerize at 60 °C for 24–36 h.

NOTE: The protocol can be paused after the polymerization.

4.2.6 Sectioning

a. Trim the block around the cell pellet using a razor blade. Then place the block in the sample chuck on the sectioning arm of an ultramicrotome. Using a glass or diamond knife, trim the block into a trapezoidal shape closely surrounding the cell pellet.

b. Obtain 90 nm ultrathin sections of the cell pellet using a glass or diamond knife.

c. Pick up a ribbon of sections on a TEM grid. Formvar-coated copper slot grids (1 x 2 mm slot) are useful for imaging serial sections. Dry the grid by blotting the edge on a piece of filter paper, and store in a TEM grid storage box.

NOTE: The protocol can be paused after sectioning.

4.2.7 TEM imaging

a. Mount the grid on the TEM holder and place into the microscope. We routinely use a Tecnai T12 at 80 kV for screening cryoAPEX samples. Acquire images of cells and subcellular structures of interest with APEX2 labeling.

b. If desired, obtain additional membrane contrast by the use of lead post-staining. See Figure 4.2 for comparison of non-post-stained samples (Figure 4.2 I–K) and lead post-stained samples (Figure 4.2 A–H).

    i. Float dry grids section-side down on a drop of dilute sodium chloride solution (~1.5 mM), 2x for 1 min each, then 1x for 10 min.

ii. Float grids on a drop of Sato's lead solution for 1 min. Wash by floating on sodium chloride solution 3x for 1 min, then on DI water 3x for 1 min. Blot excess liquid from the grids and store in a grid box.

CAUTION: Lead is a toxic chemical and should be handled with proper safety procedures and personal protective equipment. Solutions containing lead should be disposed of as hazardous chemical waste.

c. Image post-stained samples on the TEM.

NOTE: In traditional sample preparation for TEM, the lead contrasting step is performed prior to TEM imaging. However, it is recommended that for cryoAPEX samples, imaging is carried out first on non-contrasted samples. This ensures that the signal from the tag can be easily located by its strong contrast with the more lightly stained cellular structures. For many samples, no further staining will be required; however, if additional membrane contrast is desired, lead post-staining can be performed (Step 4.2.7b) and the sample re-imaged.

4.3 Representative results

In order to compare the ultrastructural preservation using the cryoAPEX method with traditional fixation and dehydration, we prepared samples in which an endoplasmic reticulum membrane (ERM; ER membrane) peptide was tagged with APEX2 and transfected into HEK-293T cells. ERM-APEX2 localizes to the cytoplasmic face of the ER and remodels the ER structure into morphologically distinct structures known as organized smooth ER (OSER)[277], [284], [285]. OSER morphology includes regions of smooth, parallel, densely stacked membranes which serve as an optimal region to compare ultrastructural preservation. Preparation of the sample by traditional APEX methods resulted in clear labeling of OSER structures (Figure 4.2A–D). Upon inspection at high magnification, the stacked membranes appeared ruffled and non-uniform gaps were present between concentric membrane densities, indicating poor membrane preservation and lipid extraction (Figure 4.2D). The sample prepared by cryoAPEX also had clearly defined labeling of OSER structures; however, the membranes were smooth and parallel, and little to no lipid extraction was seen (Figure 4.2E–H). The results from cryoAPEX were of similar high

quality preservation to those obtained from a sample which underwent HPF/FS without the additional chemical fixation and APEX2/DAB reaction steps (Figure 4.2 I–K).

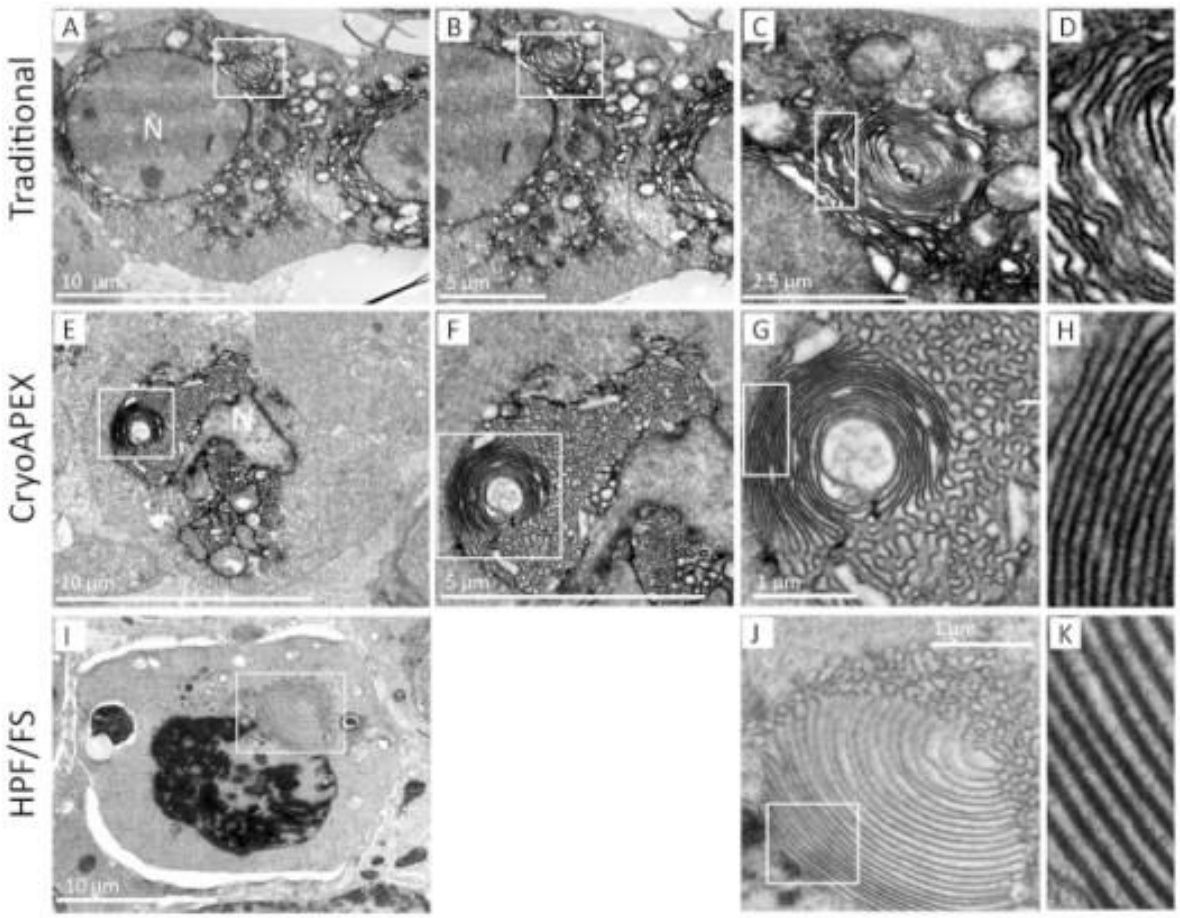

Figure 4.2. Comparison of OSER membrane preservation using traditional chemical fixation, cryoAPEX, and HPF/FS. The reorganized ER morphology in chemically fixed, DAB reacted ERM–APEX2-expressing cells that were processed via traditional chemical fixation and alcohol dehydration (A–D) or by cryoAPEX (E–H) was compared to ERM–APEX2 expressing cells that were cryofixed live and without the DAB reaction (I–K). The live cryofixed cells represent the best attainable ultrastructural preservation and serve here as the metric for evaluating membrane preservation obtained via the two APEX-based detection protocols (A–H). The evenly-spaced parallel lamellar stacking of the ER derived membranes obtained by cryoAPEX (exemplified in panels G and H), as opposed to the ruffled membranes obtained by traditional methods (panels C and D), highlights the superior membrane preservation obtained by cryoAPEX. This figure has been modified from Sengupta et al. 2019[225].

In addition to visually appreciable membrane preservation, the cryoAPEX method preserves the protein of interest such that aspects of protein distribution patterns may be observed in some cases. To illustrate this point, we used another ER-localized protein, huntingtin yeast interacting protein E (HYPE). HYPE is a membrane protein located on the luminal face of the ER membrane [286]–

[289]. HYPE-APEX2 constructs were overexpressed in HEK-293T cells. TEM analysis of 90 nm thin sections revealed that HYPE was present throughout the peripheral ER as well as the nuclear envelope (Figure 4.3 A,B). Additionally, the HYPE density was able to be resolved into regularly spaced foci along the lumenal ER membrane (Figure 4.3C, arrows). HYPE distribution and foci were also visible in a sample prepared with traditional fixation and dehydration; however, extensive membrane disruption and extraction were present, making the sample suboptimal (Figure 4.3D,E).

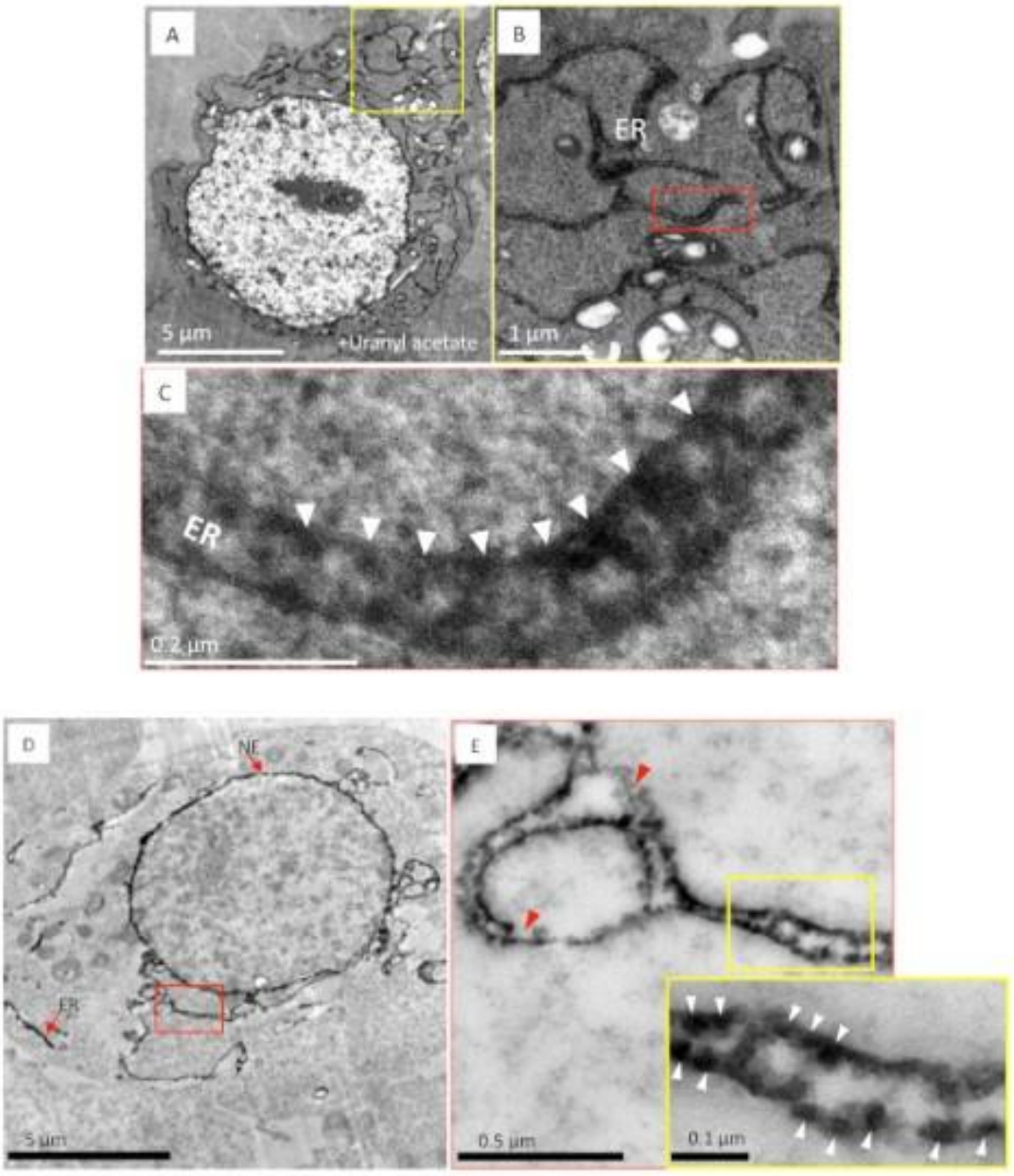

Figure 4.3. Protein localization of an APEX2-tagged ER membrane protein can be resolved into periodic foci. (A) An image of a thin section of a HEK-293T cell expressing HYPE–APEX2 and processed by cryoAPEX reveals staining of the ER in a well-preserved (dense) cytoplasmic background (B,C). Higher magnification images of a small section of the peripheral ER (demarcated by yellow box in A and shown in B, with further magnification of red box in B shown in C) exhibits periodic foci of APEX2-generated density (B, red box and C, white arrowheads showing periodicity between the HYPE foci). (D) Image of a thin section of a cell expressing HYPE-APEX2 and prepared by traditional chemical fixation and dehydration shows specific staining of the cortical ER and the nuclear envelope (red arrows). (E) At a higher magnification, periodic HYPE-specific foci were apparent within stretches of the ER (yellow box and white arrow heads in the inset), despite extensive membrane disruption, indicated by red arrows. NE = nuclear envelope. This figure has been modified from Sengupta et al. 2019[225].

To demonstrate the robust organellar specificity and applicability of the cryoAPEX method for a range of tagged proteins, we performed APEX2 labeling using three cellular markers. Mitochondria were labeled using mito-V5-APEX2[277]. This marker of the mitochondrial matrix provided specific staining of mitochondria only (Figure 4.4A). Likewise, we assessed plasma membrane labeling using CAAX-APEX2[277], which produced distinct staining of the plasma membrane only (Figure 4.4C). No labeling was observed in intracellular organelles (Figure 4.4C). Additionally, we created a new construct as a marker for the Golgi lumen by fusing the first 118 amino acids of the mouse isoform of α-mannosidase with the APEX2 gene[225]. The resulting MannII-APEX2 was transiently transfected into cells which were subsequently prepared by the cryoAPEX method. Stained Golgi stacks were clearly distinguishable from the surrounding organelles (Figure 4.4B). Individual stacks, cisternae, and some vesicles were labeled, typical of Golgi staining (Figure 4.4B). Altogether, these markers demonstrate that the cryoAPEX method provides specific labeling of membrane proteins within various organelles at high enough resolution to distinguish them from surrounding sub-cellular structures.

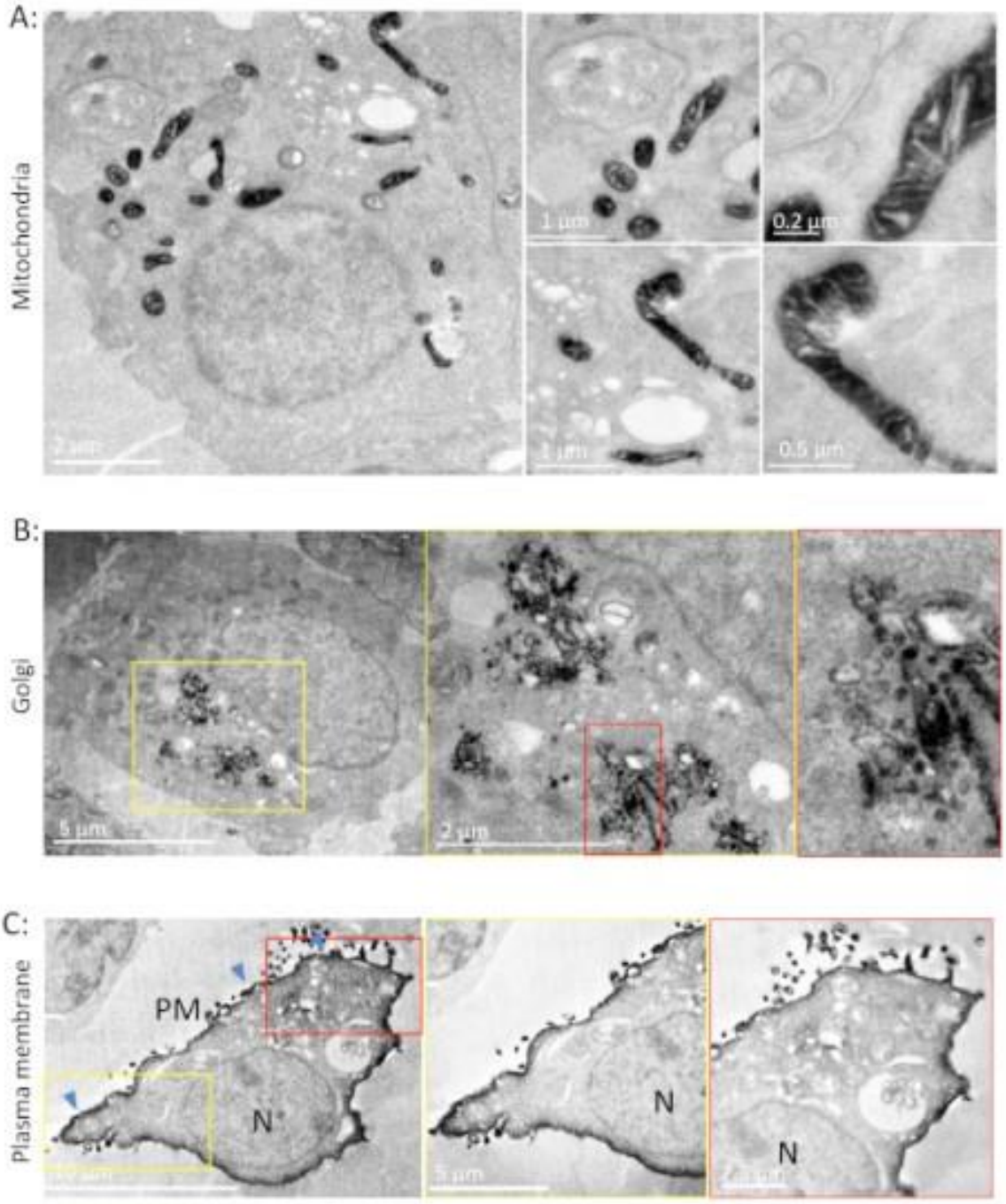

Figure 4.4. Organelle markers show specificity of the signal obtained from APEX2-tagged proteins. APEX2-tagged protein constructs designed to localize to the mitochondrial matrix (mito-V5-APEX2; shown in A), or the Golgi lumen (α-mannII-APEX2; shown in B), or the plasma membrane (CAAX-APEX2; shown in C) were transiently expressed in HEK293 cells and the samples processed by cryoAPEX. Each construct yielded organelle specific densities. Magnified views of two sections (yellow or red boxes) from the cells expressing α-mannIIAPEX2 (panel B) or CAAX-APEX2 (panel C) are shown. This figure has been modified from Sengupta et al. 2019[225].

Finally, we explored the amenability of cryoAPEX sample preparation for imaging protein densities through ET. Huntingtin yeast interacting protein E (HYPE) localizes to the ER lumen in distinct foci[225]. After transient transfection of HYPE-APEX2 in HEK-293T cells, the cryo-APEX protocol was performed followed by collection of a tilt series from a 250-nm section. The tomogram was reconstructed and the periodic density within the ER was clearly visualized in the resulting tomogram (Figure 4.5A). The ER membrane portion present in the volume was segmented by hand using interpolation and the drawing tools in IMOD, and the segmented surface was used as a mask to threshold the density inside the ER to produce an isosurface (Figure 4.5 B). Slicing of the resultant volume at various angles and depths revealed high enough resolution to detect regions of HYPE density and empty pockets where HYPE density is not present (Figure 4.5 C-D). Therefore, cryoAPEX is a promising method for observing near-native protein density and distribution in 3D within the cell.

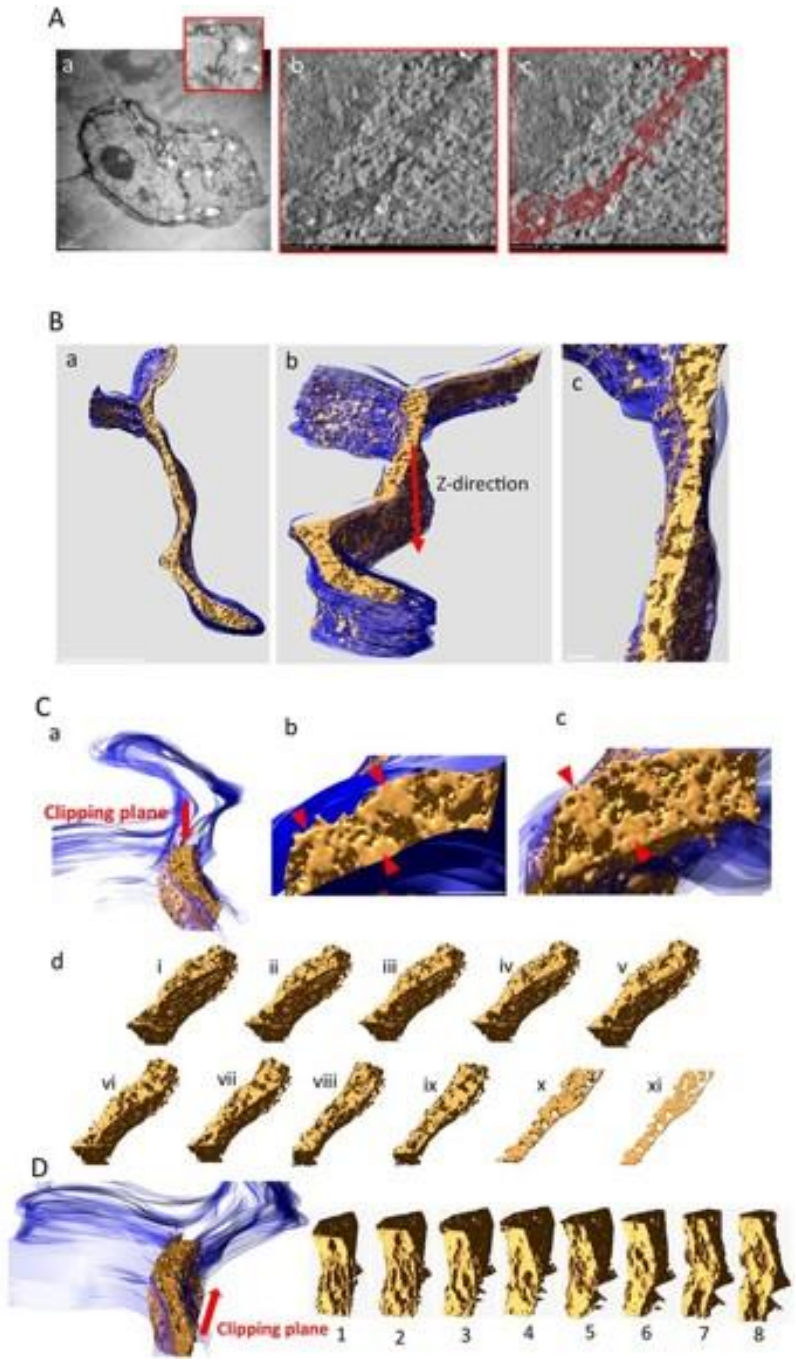

Figure 4.5. ET reconstruction of HYPE-APEX2 density within a cell prepared by the cryoAPEX protocol. (A) A TEM image of the HYPE–APEX2-expressing cell showing an area containing ER tubules from where the tilt-series was collected (panel a and magnified red box). Panel b shows a virtual slice of the reconstructed tomogram with threshholded hype density in c (in maroon). (B) 3D model of the ER membrane (blue) and the HYPE density within (gold) generated by threshholding (panels a–c). (C) Slices at different z-depths of the HYPE–APEX2 density (gold). HYPE's periodic density pattern is clearly visible along the lumenal walls. (D) Slices through the x-y plane of the HYPE-APEX2 density (gold).

4.4 Discussion

The cryoAPEX protocol presented here provides a robust method to characterize the localization of membrane proteins within the cellular environment. Not only does the use of a genetically encoded APEX2 tag provide precise localization of a protein of interest, but the use of cryofixation and low-temperature dehydration provides excellent preservation and staining of the surrounding cellular ultrastructure. Combined, these approaches are a powerful tool for localizing a protein with high precision within its subcellular context.

The crux of the advancement of this method is the fact that the loss of ultrastructure experienced after preparation by traditional TEM methods comes primarily from the dehydration step rather than the fixation step[282]. It was previously believed that peroxidase-based methods were incompatible with HPF/FS because they require chemical fixation prior to the peroxidase reaction. To work around this, a protocol named CryoCHEM was recently developed in which samples are initially cryofixed, followed by rehydration and the peroxidase reaction[290]. This approach provides excellent target localization with significant improvements in sample staining and preservation. It has been shown to be useful for tissue samples and in cases where correlative fluorescence and electron microscopy is desired. In parallel to cryoCHEM, our method combines glutaraldehyde fixation with HPF and FS. CryoAPEX offers a streamlined protocol that works effectively even for small cellular samples.

Access to high pressure freezing and freeze substitution instruments is crucial to the cryoAPEX method. These instruments and skills are increasingly common in EM facilities. Even if HPF and FS equipment are not readily available, the chemically fixed sample is stable enough for a short amount of time to be transported modest distances[282]. We have found that samples can be stored after the DAB reaction at 4 °C for at least 48 hours prior to HPF without significant loss of quality. Another critical aspect of the cryoAPEX protocol is the inclusion of controls, which are essential for a robust experiment and convincing results. Samples prepared by transient transfection with efficiency less than 100% will contain negative control cells as well as labeled cells within the same sample. If using cell lines with stable expression of APEX2, a separate negative control should be prepared by transfection of cells with the non-APEX2 labeled protein of interest. Several constructs that can serve as organellar controls are available through Addgene, and published

images are available in this and other publications that can be used for verification[225], [276]–[278]. In-depth discussion of experimental design and verification of new APEX2 fusion constructs has been provided by Martell et al.[278]

While cryoAPEX is broadly useful for the detection of membrane proteins, some limitations exist. Although APEX2 is a small 28 kDa protein, some proteins may not be able to incorporate the tag[276], [277]. APEX2 is not considered useful for labeling soluble proteins in the cytosol, due to the diffuse reaction product[276], [278]. Additionally, the detection of small quantities of protein poses a challenge due to the presence of staining in the surrounding cell. Preparation by HPF and FS preserves cellular components which are extracted by traditional fixation and dehydration. This leads to overall darker staining in the cell, potentially competing with low levels of APEX2 labeling.

The cryoAPEX technique is widely applicable to many proteins, with a limited number of steps that may require optimization. First, due to individual variability among proteins, the protein expression level and/or DAB reaction time may need to be adjusted in order for the signal to be visualized above the background staining of the cell. Helpful information and protocols for validation of new APEX2 fusion constructs and optimization of the expression and DAB staining are provided by Martell et al.[278] From a cellular staining perspective, the FS protocol and/or chemicals may need to be adjusted for optimal visualization of different organelle membranes, within different cell types, tissues, or organisms[291]–[295]. In our experience, the FS conditions presented here have worked well for a variety of mammalian cell lines.

The hybrid approach of cryoAPEX has the potential to be applied to many other genetic labeling techniques. Replacing traditional alcohol dehydration with HPF/FS is expected to greatly improve the ultrastructural preservation and the protein localization information. Utilizing sapphire discs as a cell substrate to fix cells as a monolayer improves the preservation of the cell periphery, including the cytoskeleton and cell-cell contacts. Minor modifications to the protocol would be required to use sapphire discs. APEX technology can be used to detect green fluorescent protein (GFP) tagged proteins via a GFP-binding peptide[224]. This indirect method of detection opens up the potential to utilize APEX technology for the myriad proteins already tagged with GFP. The

recently-introduced split APEX2 will be advantageous for proximity and interaction studies[296]. Additionally, existing HRP-based methods can be combined with HPF/FS to improve cellular preservation. One example is *fl*uorescent *i*ndicator and *p*eroxidase for *p*recipitation with *E*M *r*esolution (FLIPPER), in which individual cell markers have been fused with both a fluorescent tag and HRP, providing lumenal markers for Golgi or ER[297]. Use of improved peroxidase substrates in place of DAB is also possible with this method, including substrates which are optimized for RNA labeling [298]. CryoAPEX also provides in-cell labeling and ultrastructural preservation necessary for three dimensional analysis of protein distribution through electron tomography, and potentially at high volumes through SBF-SEM or FIB-SEM[225], [299].

Overall, CryoAPEX is a robust method with wide applicability. In principle, it can be applied to any membrane protein, whether within the lumenal space of an organelle, on the cytoplasmic face, within vesicles, on the cell's plasma membrane or even in the extracellular space. For this vast range of membrane proteins, the cryoAPEX method provides the potential to see the localization and distribution of a protein with accuracy within its subcellular context.

REFERENCES

[1] A. P. Waterson and L. Wilkinson, *An introduction to the history of virology*. Cambridge, London, New York, Melbourne: Cambridge University Press, 1978.

[2] D. H. Krüger, P. Schneck, and H. R. Gelderblom, "Helmut Ruska and the visualisation of viruses," *Lancet*, vol. 355, no. 9216, pp. 1713–1717, 2000.

[3] G. A. Kausche, E. Pfankuch, and H. Ruska, "Die Sichtbarmachung yon pflanzlichem Virus im Übermikroskop.," *Naturwissenschaften*, vol. 27, pp. 292–299, 1939.

[4] H. Ruska, B. von Borries, and E. Ruska, "Die Bedeutung der Übermikroskopie für die Virusforschung," *Arch. Gesamte Virusforsch.*, vol. 1, no. 1, pp. 155–169, 1940.

[5] B. von Borries, E. Ruska, and H. Ruska, "Bakterien und Virus in übermikroskopischer Aufnahme," *Klin. Wochenschr.*, vol. 17, no. 27, pp. 921–925, 1938.

[6] H. Ruska, "Über das Virus der Varicellen und des Zoster," *Klin. Wochenschr.*, vol. 22, pp. 703–704, 1943.

[7] H. Ruska, "Die sichtbarmachung der bakteriophagen lyse im übermikroskop," *Naturwissenschaften*, vol. 28, no. 3, pp. 45–46, 1940.

[8] F. Kallman, R. C. Williams, R. Dulbecco, and M. Vogt, "Fine structure of changes produced in cultured cells sampled at specified intervals during a single growth cycle of polio virus," *J. Cell Biol.*, vol. 4, no. 3, pp. 301–308, 1958.

[9] B. G. Kopek, G. Perkins, D. J. Miller, M. H. Ellisman, and P. Ahlquist, "Three-dimensional analysis of a viral RNA replication complex reveals a virus-induced mini-organelle.," *PLoS Biol.*, vol. 5, no. 9, pp. 2022–2034, Sep. 2007.

[10] I. Romero-Brey and R. Bartenschlager, "Membranous replication factories induced by plus-strand RNA viruses," *Viruses*, vol. 6, no. 7, pp. 2826–2857, 2014.

[11] M. R. Denison, "Seeking membranes: Positive-strand RNA virus replication complexes," *PLoS Biol.*, vol. 6, no. 10, pp. 2098–2100, 2008.

[12] J. Mackenzie, "Wrapping things up about virus RNA replication," *Traffic*, vol. 6, no. 11, pp. 967–977, 2005.

[13] S. Miller and J. Krijnse-Locker, "Modification of intracellular membrane structures for virus replication.," *Nat. Rev. Microbiol.*, vol. 6, no. 5, pp. 363–74, May 2008.

[14] J. A. Den Boon, A. Diaz, and P. Ahlquist, "Cytoplasmic viral replication complexes," *Cell Host Microbe*, vol. 8, no. 1, pp. 77–85, 2010.

[15] G. A. Belov, V. Nair, B. T. Hansen, F. H. Hoyt, E. R. Fischer, and E. Ehrenfeld, "Complex Dynamic Development of Poliovirus Membranous Replication Complexes," *J. Virol.*, vol. 86, no. 1, pp. 302–312, 2012.

[16] R. W. A. L. Limpens, H. M. Van Der Schaar, D. Kumar, A. J. Koster, and E. J. Snijder, "The Transformation of Enterovirus Replication Structures : a Three- Dimensional Study of Single- and Double-Membrane Compartments," vol. 2, no. 5, pp. 1–10, 2011.

[17] C. E. Melia *et al.*, "The Origin, Dynamic Morphology, and PI4P-Independent Formation of Encephalomyocarditis Virus Replication Organelles," *MBio*, vol. 9, no. 2, pp. e00420-18, 2018.

[18] J. Fontana, C. López-Iglesias, W.-P. Tzeng, T. K. Frey, J. J. Fernández, and C. Risco, "Three-dimensional structure of Rubella virus factories.," *Virology*, vol. 405, no. 2, pp. 579–91, Sep. 2010.

[19] I. Romero-Brey *et al.*, "Three-dimensional architecture and biogenesis of membrane structures associated with hepatitis C virus replication.," *PLoS Pathog.*, vol. 8, no. 12, p. e1003056, Jan. 2012.

[20] P. Ferraris *et al.*, "Sequential biogenesis of host cell membrane rearrangements induced by hepatitis C virus infection," *Cell. Mol. Life Sci.*, vol. 70, no. 7, pp. 1297–1306, 2013.

[21] S. Welsch *et al.*, "Composition and Three-Dimensional Architecture of the Dengue Virus Replication and Assembly Sites," *Cell Host Microbe*, vol. 5, no. 4, pp. 365–375, Apr. 2009.

[22] J. Junjhon, J. G. Pennington, T. J. Edwards, R. Perera, J. Lanman, and R. J. Kuhn, "Ultrastructural characterization and three-dimensional architecture of replication sites in dengue virus-infected mosquito cells.," *J. Virol.*, vol. 88, no. 9, pp. 4687–97, May 2014.

[23] L. K. Gillespie, A. Hoenen, G. Morgan, M. Jason, and J. M. Mackenzie, "The Endoplasmic Reticulum Provides the Membrane Platform for Biogenesis of the Flavivirus Replication Complex," *J. Virol.*, vol. 84, no. 20, pp. 10438–10447, Oct. 2010.

[24] L. Miorin *et al.*, "Three-dimensional architecture of tick-borne encephalitis virus replication sites and trafficking of the replicated RNA.," *J. Virol.*, vol. 87, no. 11, pp. 6469–81, Jun. 2013.

[25] T. Bílý, M. Palus, L. Eyer, J. Elsterová, M. Vancová, and D. Růžek, "Electron Tomography Analysis of Tick-Borne Encephalitis Virus Infection in Human Neurons," *Sci. Rep.*, vol. 5, p. 10745, 2015.

[26] M. Cortese *et al.*, "Ultrastructural Characterization of Zika Virus Replication Factories," *Cell Rep.*, vol. 18, no. 9, pp. 2113–2123, 2017.

[27] K. Knoops *et al.*, "SARS-coronavirus replication is supported by a reticulovesicular network of modified endoplasmic reticulum.," *PLoS Biol.*, vol. 6, no. 9, p. e226, Sep. 2008.

[28] H. J. Maier *et al.*, "Infectious bronchitis virus generates spherules from zippered endoplasmic reticulum membranes," *MBio*, vol. 4, no. 5, 2013.

[29] K. Knoops, M. Bárcena, R. W. A. L. Limpens, A. J. Koster, A. M. Mommaas, and E. J. Snijder, "Ultrastructural Characterization of Arterivirus Replication Structures: Reshaping the Endoplasmic Reticulum To Accommodate Viral RNA Synthesis," *J. Virol.*, vol. 86, no. 5, pp. 2474–2487, Mar. 2012.

[30] B. van der Hoeven, D. Oudshoorn, A. J. Koster, E. J. Snijder, M. Kikkert, and M. Bárcena, "Biogenesis and architecture of arterivirus replication organelles," *Virus Res.*, vol. 220, pp. 70–90, 2016.

[31] K. J. Ertel *et al.*, "Cryo-electron tomography reveals novel features of a viral rna replication compartment," *Elife*, vol. 6, pp. 1–24, 2017.

[32] C. E. Melia *et al.*, “Origins of enterovirus replication organelles established by whole-cell electron microscopy,” *MBio*, vol. 10, no. 3, pp. 1–12, 2019.

[33] D. Magliano, J. A. Marshall, D. S. Bowden, N. Vardaxis, J. Meanger, and J. Y. Lee, “Rubella virus replication complexes are virus-modified lysosomes,” *Virology*, vol. 240, no. 1, pp. 57–63, 1998.

[34] S. Froshauer, J. Kartenbeck, and A. Helenius, “Alphavirus RNA Replicase Is Located on the Cytoplasmic Surface of Endosomes and Lysosomes,” *J. Cell Biol.*, vol. 107, no. 6, pp. 2075–2086, 1988.

[35] E. I. Frolova, R. Gorchakov, L. Pereboeva, S. Atasheva, and I. Frolov, “Functional Sindbis virus replicative complexes are formed at the plasma membrane.,” *J. Virol.*, vol. 84, no. 22, pp. 11679–11695, Nov. 2010.

[36] J. Peränen and L. Kääriäinen, “Biogenesis of type I cytopathic vacuoles in Semliki Forest virus-infected BHK cells.,” *J. Virol.*, vol. 65, no. 3, pp. 1623–1627, 1991.

[37] P. Kujala, A. Ikaheimonen, N. Ehsani, H. Vihinen, P. Auvinen, and L. Kaariainen, “Biogenesis of the Semliki Forest Virus RNA Replication Complex,” *J. Virol.*, vol. 75, no. 8, pp. 3873–3884, 2001.

[38] E. D. Rossignol, K. N. Peters, J. H. Connor, and E. Bullitt, “Zika virus induced cellular remodelling,” *Cell. Microbiol.*, vol. 19, no. 8, pp. 1–10, 2017.

[39] J. F. David-Ferreira and R. A. Manaker, “An electron microscope study of the development of a mouse hepatitis virus in tissue culture cells,” *J. Cell Biol.*, vol. 24, pp. 57–78, 1965.

[40] R. Gosert, A. Kanjanahaluethai, D. Egger, K. Bienz, and S. C. Baker, “RNA Replication of Mouse Hepatitis Virus Takes Place at Double-Membrane Vesicles,” *J. Virol.*, vol. 76, no. 8, pp. 3697–3708, Apr. 2002.

[41] M. Ulasli, M. H. Verheije, C. A. M. de Haan, and F. Reggiori, “Qualitative and quantitative ultrastructural analysis of the membrane rearrangements induced by coronavirus.,” *Cell. Microbiol.*, vol. 12, no. 6, pp. 844–61, Jun. 2010.

[42] A. H. de Wilde *et al.*, “MERS-coronavirus replication induces severe in vitro cytopathology and is strongly inhibited by cyclosporin A or interferon-α treatment,” *J. Gen. Virol.*, vol. 94, no. PART8, pp. 1749–1760, 2013.

[43] H. J. Maier, P. C. Hawes, and E. M. Cottam, “Infectious Bronchitis Virus Generates Spherules from Zippered,” *MBio*, 2013.

[44] CDC, “SARS Basics Fact Sheet,” *National Center for Immunization and Respiratory Diseases, Division of Viral Diseases*, 2017. [Online]. Available: https://www.cdc.gov/sars/about/fs-sars.html.

[45] C. Drosten *et al.*, “Identification of a novel coronavirus in patients with severe acute respiratory syndrome,” *N. Engl. J. Med.*, vol. 348, no. 20, pp. 1967–1976, 2003.

[46] T. G. Ksiazek *et al.*, “A Novel Coronavirus Associated with Severe Acute Respiratory Syndrome,” *N. Engl. J. Med.*, vol. 348, no. 20, pp. 1953–1966, 2003.

[47] S. K. P. Lau *et al.*, “Severe acute respiratory syndrome coronavirus-like virus in Chinese horseshoe bats,” *Proc. Natl. Acad. Sci. U. S. A.*, vol. 102, no. 39, pp. 14040–14045, 2005.

[48] W. Li *et al.*, "Bats are natural reservoirs of SARS-like coronaviruses," *Science (80-.).*, vol. 310, no. 5748, pp. 676–679, 2005.

[49] WHO, "Middle East respiratory syndrome coronavirus (MERS-CoV)," *Emergencies*, 2020. [Online]. Available: https://www.who.int/emergencies/mers-cov/en/.

[50] X. Chen, A. A. Chughtai, A. Dyda, and C. R. Macintyre, "Comparative epidemiology of Middle East respiratory syndrome coronavirus (MERS-CoV) in Saudi Arabia and South Korea," *Emerg. Microbes Infect.*, vol. 6, no. 6, 2017.

[51] V. M. Corman *et al.*, "Rooting the Phylogenetic Tree of Middle East Respiratory Syndrome Coronavirus by Characterization of a Conspecific Virus from an African Bat," *J. Virol.*, vol. 88, no. 19, pp. 11297–11303, 2014.

[52] B. L. Haagmans *et al.*, "Middle East respiratory syndrome coronavirus in dromedary camels: An outbreak investigation," *Lancet Infect. Dis.*, vol. 14, no. 2, pp. 140–145, 2014.

[53] E. I. Azhar *et al.*, "Evidence for camel-to-human transmission of MERS coronavirus," *N. Engl. J. Med.*, vol. 370, no. 26, pp. 2499–2505, 2014.

[54] WHO, "Coronavirus disease (COVID-19) pandemic," *Diseases*, 2020. [Online]. Available: https://www.who.int/emergencies/diseases/novel-coronavirus-2019.

[55] P. Zhou *et al.*, "A pneumonia outbreak associated with a new coronavirus of probable bat origin," *Nature*, vol. 579, no. 7798, pp. 270–273, 2020.

[56] R. L. Graham, E. F. Donaldson, and R. S. Baric, "A decade after SARS: Strategies for controlling emerging coronaviruses," *Nat. Rev. Microbiol.*, vol. 11, no. 12, pp. 836–848, 2013.

[57] G. Gerna *et al.*, "Genetic Variability of Human Coronavirus OC43-, 229E-, and NL63-Like Strains and Their Association With Lower Respiratory Tract Infections of Hospitalized Infants and Immunocompromised Patients," *J. Med. Virol.*, vol. 78, pp. 938–949, 2006.

[58] K. Pyrc, B. Berkhout, and L. van der Hoek, "The Novel Human Coronaviruses NL63 and HKU1," *J. Virol.*, vol. 81, no. 7, pp. 3051–3057, 2007.

[59] A. E. Gorbalenya, L. Enjuanes, J. Ziebuhr, and E. J. Snijder, "Nidovirales: Evolving the largest RNA virus genome," *Virus Res.*, vol. 117, no. 1, pp. 17–37, 2006.

[60] A. R. Fehr and S. Perlman, "Coronaviruses: An Overview of Their Replication and Pathogenesis," in *Coronaviruses: Methods and Protocols*, vol. 1282, no. 1, H. J. Maier, Ed. New York, 2015, pp. 1–282.

[61] A. M. Mielech, Y. Chen, A. D. Mesecar, and S. C. Baker, "Nidovirus papain-like proteases: Multifunctional enzymes with protease, deubiquitinating and deISGylating activities," *Virus Res.*, vol. 194, pp. 184–190, 2014.

[62] B. W. Neuman, "Bioinformatics and functional analyses of coronavirus nonstructural proteins involved in the formation of replicative organelles," *Antiviral Res.*, vol. 135, pp. 97–107, 2016.

[63] A. J. W. te Velthuis, J. J. Arnold, C. E. Cameron, S. H. E. van den Worm, and E. J. Snijder, "The RNA polymerase activity of SARS-coronavirus nsp12 is primer dependent," *Nucleic Acids Res.*, vol. 38, no. 1, pp. 203–214, 2009.

[64] I. Imbert *et al.*, "A second, non-canonical RNA-dependent RNA polymerase in SARS coronavirus," *EMBO J.*, vol. 25, no. 20, pp. 4933–4942, 2006.

[65] A. J. W. te Velthuis, S. H. E. van den Worm, and E. J. Snijder, "The SARS-coronavirus nsp7+nsp8 complex is a unique multimeric RNA polymerase capable of both de novo initiation and primer extension.," *Nucleic Acids Res.*, vol. 40, no. 4, pp. 1737–47, Feb. 2012.

[66] Y. Zhai *et al.*, "Insights into SARS-CoV transcription and replication from the structure of the nsp7-nsp8 hexadecamer.," *Nat. Struct. Mol. Biol.*, vol. 12, no. 11, pp. 980–6, Nov. 2005.

[67] R. Züst *et al.*, "Coronavirus non-structural protein 1 is a major pathogenicity factor: Implications for the rational design of coronavirus vaccines," *PLoS Pathog.*, vol. 3, no. 8, pp. 1062–1072, 2007.

[68] M. P. Egloff *et al.*, "The severe acute respiratory syndrome-coronavirus replicative protein nsp9 is a single-stranded RNA-binding subunit unique in the RNA virus world," *Proc. Natl. Acad. Sci. U. S. A.*, vol. 101, no. 11, pp. 3792–3796, 2004.

[69] A. Seybert, A. Hegyi, S. G. Siddell, and J. Ziebuhr, "The human coronavirus 229E superfamily 1 helicase has RNA and DNA duplex-unwinding activities with 5'-to-3' polarity," *RNA*, vol. 6, no. 7, pp. 1056–1068, 2000.

[70] A. Seybert, C. C. Posthuma, L. C. van Dinten, E. J. Snijder, A. E. Gorbalenya, and J. Ziebuhr, "A Complex Zinc Finger Controls the Enzymatic Activities of Nidovirus Helicases," *J. Virol.*, vol. 79, no. 2, pp. 696–704, 2005.

[71] J. A. Tanner *et al.*, "The severe acute respiratory syndrome (SARS) coronavirus NTPasefhelicase belongs to a distinct class of 5′ to 3′ viral helicases," *J. Biol. Chem.*, vol. 278, no. 41, pp. 39578–39582, 2003.

[72] L. D. Eckerle *et al.*, "Infidelity of SARS-CoV Nsp14-exonuclease mutant virus replication is revealed by complete genome sequencing," *PLoS Pathog.*, vol. 6, no. 5, pp. 1–15, 2010.

[73] K. Bhardwaj, P. Liu, J. L. Leibowitz, and C. C. Kao, "The Coronavirus Endoribonuclease Nsp15 Interacts with," pp. 4294–4304, 2012.

[74] K. A. Ivanov *et al.*, "Major genetic marker of nidoviruses encodes a replicative endoribonuclease," *Proc. Natl. Acad. Sci. U. S. A.*, vol. 101, no. 34, pp. 12694–12699, 2004.

[75] R. Züst *et al.*, "Ribose 2'-O-methylation provides a molecular signature for the distinction of self and non-self mRNA dependent on the RNA sensor Mda5," *Nat. Immunol.*, vol. 12, no. 2, pp. 137–143, 2011.

[76] E. J. Snijder *et al.*, "Unique and conserved features of genome and proteome of SARS-coronavirus, an early split-off from the coronavirus group 2 lineage," *J. Mol. Biol.*, vol. 331, no. 5, pp. 991–1004, 2003.

[77] M. R. Denison, R. L. Graham, E. F. Donaldson, L. D. Eckerle, and R. S. Baric, "Coronaviruses An RNA proofreading machine regulates replication fidelity and diversity," *RNA Biol.*, vol. 8, no. 2, pp. 270–279, 2011.

[78] M. M. Angelini, M. Akhlaghpour, and B. W. Neuman, "Severe acute respiratory syndrome coronavirus nonstructural proteins 3, 4, and 6 induce double-membrane vesicles," *MBio*, vol. 4, no. 4, pp. e00524-13, 2013.

[79] M. C. Hagemeijer *et al.*, "Membrane rearrangements mediated by coronavirus nonstructural proteins 3 and 4.," *Virology*, vol. 458–459, pp. 125–35, Jun. 2014.

[80] M. C. Hagemeijer, P. J. M. M. Rottier, and C. A. M. M. de Haan, "Biogenesis and dynamics of the coronavirus replicative structures.," *Viruses*, vol. 4, no. 11, pp. 3245–69, Nov. 2012.

[81] C. A. M. de Haan and P. J. M. Rottier, "Molecular Interactions in the Assembly of Coronaviruses," *Adv. Virus Res.*, vol. 64, no. 5, pp. 165–230, 2005.

[82] L. Wilson, C. Mckinlay, P. Gage, and G. Ewart, "SARS coronavirus E protein forms cation-selective ion channels," *Virology*, vol. 330, no. 1, pp. 322–331, 2004.

[83] L. Wilson, P. Gage, and G. Ewart, "Hexamethylene amiloride blocks E protein ion channels and inhibits coronavirus replication," *Virology*, vol. 353, no. 2, pp. 294–306, 2006.

[84] M. R. Denison *et al.*, "The Putative Helicase of the Coronavirus Mouse Hepatitis Virus Is Processed from the Replicase Gene Polyprotein and Localizes in Complexes That Are Active in Viral RNA Synthesis," *J. Virol.*, vol. 73, no. 8, pp. 6862–6871, 1999.

[85] Y. van der Meer *et al.*, "Localization of mouse hepatitis virus nonstructural proteins and RNA synthesis indicates a role for late endosomes in viral replication.," *J. Virol.*, vol. 73, no. 9, pp. 7641–57, 1999.

[86] D. A. Brian, B. G. Hague, and T. E. Kienzle, "The coronavirus hemagglutinin esterase glycoprotein," in *The Coronaviridae*, S. G. Siddell, Ed. New York, 1995, pp. 165–179.

[87] Q. F. Zhang *et al.*, "Morphology and morphogenesis of severe acute respiratory syndrome (SARS)-associated virus," *Acta Biochim. Biophys. Sin. (Shanghai).*, vol. 35, no. 6, pp. 587–591, 2003.

[88] B. W. Neuman *et al.*, "A structural analysis of M protein in coronavirus assembly and morphology.," *J. Struct. Biol.*, vol. 174, no. 1, pp. 11–22, Apr. 2011.

[89] J. S. M. Peiris, Y. Guan, and K. Y. Yuen, "Severe acute respiratory syndrome," *Nat. Med.*, vol. 10, no. 12S, pp. S88–S97, 2004.

[90] H. Hofmann, K. Pyrc, L. Van Der Hoek, M. Geier, B. Berkhout, and S. Pöhlmann, "Human coronavirus NL63 employs the severe acute respiratory syndrome coronavirus receptor for cellular entry," *Proc. Natl. Acad. Sci. U. S. A.*, vol. 102, no. 22, pp. 7988–7993, 2005.

[91] W. Li *et al.*, "Angiotensin-converting enzyme 2 is a functional receptor for the SARS coronavirus," *Nature*, vol. 426, no. NOVEMBER, pp. 450–454, 2003.

[92] M. Hoffmann *et al.*, "SARS-CoV-2 Cell Entry Depends on ACE2 and TMPRSS2 and Is Blocked by a Clinically Proven Protease Inhibitor," *Cell*, vol. 181, no. 2, pp. 271-280.e8, 2020.

[93] V. S. Raj *et al.*, "Dipeptidyl peptidase 4 is a functional receptor for the emerging human coronavirus-EMC," *Nature*, vol. 495, no. 7440, pp. 251–254, 2013.

[94] R. K. Williams, G. S. Jiang, and K. V. Holmes, "Receptor for mouse hepatitis virus is a member of the carcinoembryonic antigen family of glycoproteins," *Proc. Natl. Acad. Sci. U. S. A.*, vol. 88, no. 13, pp. 5533–5536, 1991.

[95] P. Nédellec *et al.*, "Bgp2, a new member of the carcinoembryonic antigen-related gene family, encodes an alternative receptor for mouse hepatitis viruses.," *J. Virol.*, vol. 68, no. 7, pp. 4525–4537, 1994.

[96] S. Belouzard, V. C. Chu, and G. R. Whittaker, "Activation of the SARS coronavirus spike protein via sequential proteolytic cleavage at two distinct sites," *Proc. Natl. Acad. Sci. U. S. A.*, vol. 106, no. 14, pp. 5871–5876, 2009.

[97] B. J. Bosch, R. van der Zee, C. A. M. de Haan, and P. J. M. Rottier, "The Coronavirus Spike Protein Is a Class I Virus Fusion Protein: Structural and Functional Characterization of the Fusion Core Complex," *J. Virol.*, vol. 77, no. 16, pp. 8801–8811, 2003.

[98] C. S. Goldsmith *et al.*, "Ultrastructural characterization of SARS coronavirus," *Emerg. Infect. Dis.*, vol. 10, no. 2, pp. 320–326, 2004.

[99] E. J. Snijder *et al.*, "Ultrastructure and origin of membrane vesicles associated with the severe acute respiratory syndrome coronavirus replication complex.," *J. Virol.*, vol. 80, no. 12, pp. 5927–40, Jun. 2006.

[100] J. Klumperman, J. K. Locker, A. Meijer, M. C. Horzinek, H. J. Geuze, and P. J. M. Rottier, "Coronavirus M Proteins Accumulate in the Golgi Complex beyond the Site of Virion Budding," vol. 68, no. 10, pp. 6523–6534, 1994.

[101] J. Tooze, S. Tooze, and G. Warren, "Replication of coronavirus MHV-A59 in sac- cells: determination fo the first site of budding of progeny virions," *Eur. J. Cell Biol.*, vol. 33, pp. 281–293, 1984.

[102] Y. Cong, P. Verlhac, and F. Reggiori, "The interaction between nidovirales and autophagy components," *Viruses*, vol. 9, no. 7, 2017.

[103] M. C. Hagemeijer *et al.*, "Dynamics of Coronavirus Replication-Transcription Complexes," *J. Virol.*, vol. 84, no. 4, pp. 2134–2149, 2010.

[104] B. H. Harcourt *et al.*, "Identification of Severe Acute Respiratory Syndrome Coronavirus Replicase Products and Characterization of Papain-Like Protease Activity," *J. Virol.*, vol. 78, no. 24, pp. 13600–13612, 2004.

[105] A. Kanjanahaluethai, Z. Chen, D. Jukneliene, and S. C. Baker, "Membrane topology of murine coronavirus replicase nonstructural protein 3," *Virology*, vol. 361, no. 2, pp. 391–401, 2007.

[106] M. Oostra, E. G. te Lintelo, M. Deijs, M. H. Verheije, P. J. M. Rottier, and C. A. M. de Haan, "Localization and Membrane Topology of Coronavirus Nonstructural Protein 4: Involvement of the Early Secretory Pathway in Replication," *J. Virol.*, vol. 81, no. 22, pp. 12323–12336, 2007.

[107] M. Oostra *et al.*, "Topology and membrane anchoring of the coronavirus replication complex: not all hydrophobic domains of nsp3 and nsp6 are membrane spanning.," *J. Virol.*, vol. 82, no. 24, pp. 12392–405, Dec. 2008.

[108] M. H. Verheije *et al.*, "Mouse hepatitis coronavirus RNA replication depends on GBF1-mediated ARF1 activation," *PLoS Pathog.*, vol. 4, no. 6, p. e1000088, 2008.

[109] F. Reggiori *et al.*, "Coronaviruses hijack the LC3-I-positive EDEMosomes, ER-derived vesicles exporting short-lived ERAD regulators, for replication," *Cell Host Microbe*, vol. 7, no. 6, pp. 500–508, Jun. 2010.

[110] M. Molinari, V. Calanca, C. Galli, P. Lucca, and P. Paganetti, "Role of EDEM in the release of misfolded glycoproteins from the calnexin cycle," *Science (80-.).*, vol. 299, no. 5611, pp. 1397–1400, 2003.

[111] Y. Oda, N. Hosokawa, I. Wada, and K. Nagata, "EDEM As an Acceptor of Terminally Misfolded Glycoproteins Released from Calnexin," *Science (80-.).*, vol. 299, no. February, pp. 1394–97, 2003.

[112] R. Bernasconi, T. Pertel, J. Luban, and M. Molinari, "A dual task for the Xbp1-responsive OS-9 variants in the mammalian endoplasmic reticulum: Inhibiting secretion of misfolded protein conformers and enhancing their disposal," *J. Biol. Chem.*, vol. 283, no. 24, pp. 16446–16454, 2008.

[113] J. C. Christianson, T. A. Shaler, R. E. Tyler, and R. R. Kopito, "OS-9 and GRP94 deliver mutant α1-antitrypsin to the Hrd1-SEL1L ubiquitin ligase complex for ERAD," *Nat. Cell Biol.*, vol. 10, no. 3, pp. 272–282, 2008.

[114] C. Zuber, J. H. Cormier, B. Guhl, R. Santimaria, D. N. Hebert, and J. Roth, "EDEM1 reveals a quality control vesicular transport pathway out of the endoplasmic reticulum not involving the COPII exit sites.," *Proc. Natl. Acad. Sci. U. S. A.*, vol. 104, no. 11, pp. 4407–4412, 2007.

[115] V. Le Fourn, B. Guhl, R. Santimaria, C. Zuber, and J. Roth, "Basal autophagy is involved in the degradation of the ERAD component EDEM1," *Cell. Mol. Life Sci.*, vol. 66, pp. 1434–1445, 2009.

[116] T. Calì, C. Galli, S. Olivari, and M. Molinari, "Segregation and rapid turnover of EDEM1 by an autophagy-like mechanism modulates standard ERAD and folding activities," *Biochem. Biophys. Res. Commun.*, vol. 371, no. 3, pp. 405–410, 2008.

[117] L. A. Silva and T. S. Dermody, "Chikungunya virus: Epidemiology, replication, disease mechanisms, and prospective intervention strategies," *J. Clin. Invest.*, vol. 127, no. 3, pp. 737–749, 2017.

[118] J. E. Staples, R. F. Breiman, and A. M. Powers, "Chikungunya Fever: An Epidemiological Review of a Re-Emerging Infectious Disease," *Clin. Infect. Dis.*, vol. 49, no. 6, pp. 942–948, 2009.

[119] A. Toivanen, "Alphaviruses: An emerging cause of arthritis?," *Curr. Opin. Rheumatol.*, vol. 20, no. 4, pp. 486–490, 2008.

[120] M. A. Zacks and S. Paessler, "Encephalitic alphaviruses," *Vet. Microbiol.*, vol. 140, no. 3–4, pp. 281–286, 2010.

[121] S. C. Weaver and W. K. Reisen, "Present and future arboviral threats," *Antiviral Res.*, vol. 85, no. 2, pp. 328–345, 2010.

[122] A. Suhrbier, M.-C. Jaffar-Bandjee, and P. Gasque, "Arthritogenic alphaviruses - an overview," *Nat. Rev. Rheumatol.*, vol. 8, pp. 420–429, 2012.

[123] J. H. Strauss and E. G. Strauss, “The alphaviruses: gene expression, replication, and evolution,” *Microbiol. Rev.*, vol. 58, no. 3, pp. 491–562, 1994.

[124] E. F. da Silva-Júnior, G. O. Leoncini, É. E. S. Rodrigues, T. M. Aquino, and J. X. Araújo-Júnior, “The medicinal chemistry of Chikungunya virus,” *Bioorganic Med. Chem.*, vol. 25, no. 16, pp. 4219–4244, 2017.

[125] J. Jin *et al.*, “Neutralizing Monoclonal Antibodies Block Chikungunya Virus Entry and Release by Targeting an Epitope Critical to Viral Pathogenesis,” *Cell Rep.*, vol. 13, no. 11, pp. 2553–2564, 2015.

[126] E. Reichert, A. Clase, A. Bacetty, and J. Larsen, “Alphavirus Antiviral Drug Development: Scientific Gap Analysis and Prospective Research Areas,” *Biosecurity and Bioterrorism*, vol. 7, no. 4, pp. 413–427, 2009.

[127] L. J. Chang *et al.*, “Safety and tolerability of chikungunya virus-like particle vaccine in healthy adults: A phase 1 dose-escalation trial,” *Lancet*, vol. 384, no. 9959, pp. 2046–2052, 2014.

[128] J. H. Erasmus, S. L. Rossi, and S. C. Weaver, “Development of vaccines for chikungunya fever,” *J. Infect. Dis.*, vol. 214, no. Suppl 5, pp. S488–S496, 2016.

[129] E. Hefti, D. H. L. Bishop, D. T. Dubin, and V. Stollar, “5′ Nucleotide Sequence of Sindbis Viral RNA,” *J. Virol.*, vol. 17, no. 1, pp. 149–159, 1976.

[130] J. A. Lemm, T. Rümenapf, E. G. Strauss, J. H. Strauss, and C. M. Rice, “Polypeptide requirements for assembly of functional Sindbis virus replication complexes: a model for the temporal regulation of minus- and plus-strand RNA synthesis.,” *EMBO J.*, vol. 13, no. 12, pp. 2925–2934, 1994.

[131] Y. Shirako and J. H. Strauss, “Regulation of Sindbis virus RNA replication: uncleaved P123 and nsP4 function in minus-strand RNA synthesis, whereas cleaved products from P123 are required for efficient plus-strand RNA synthesis.,” *J. Virol.*, vol. 68, no. 3, pp. 1874–1885, 1994.

[132] L. Vasiljeva, A. Merits, A. Golubtsov, V. Sizemskaja, L. Kääriäinen, and T. Ahola, “Regulation of the Sequential Processing of Semliki Forest Virus Replicase Polyprotein,” *J. Biol. Chem.*, vol. 278, no. 43, pp. 41636–41645, 2003.

[133] T. Ahola, A. Lampio, P. Auvinen, and L. Kääriäinen, “Semliki Forest virus mRNA capping enzyme requires association with anionic membrane phospholipids for activity,” *EMBO J.*, vol. 18, no. 11, pp. 3164–3172, 1999.

[134] A. Lampio *et al.*, “Membrane binding mechanism of an RNA virus-capping enzyme,” *J. Biol. Chem.*, vol. 275, no. 48, pp. 37853–37859, 2000.

[135] P. Spuul, A. Salonen, A. Merits, E. Jokitalo, L. Kääriäinen, and T. Ahola, “Role of the Amphipathic Peptide of Semliki Forest Virus Replicase Protein nsP1 in Membrane Association and Virus Replication,” *J. Virol.*, vol. 81, no. 2, pp. 872–883, 2007.

[136] P. Laakkonen, M. Hyvönen, J. Peränen, and L. Kääriäinen, “Expression of Semliki Forest virus nsP1-specific methyltransferase in insect cells and in Escherichia coli.,” *J. Virol.*, vol. 68, no. 11, pp. 7418–7425, 1994.

[137] S. Mi, R. Durbin, H. V. Huang, C. M. Rice, and V. Stollar, “Association of the sindbis virus RNA methyltransferase activity with the nonstructural protein nsP1,” *Virology*, vol. 170, no. 2, pp. 385–391, 1989.

[138] S. Mi and V. Stollar, “Expression of sindbis virus nsP1 and methyltransferase activity inEscherichia coli,” *Virology*, vol. 184, no. 1, pp. 423–427, 1991.

[139] L. Vasiljeva, A. Merits, P. Auvinen, and L. Kääriäinen, “Identification of a novel function of the Alphavirus capping apparatus. RNA 5’-triphosphatase activity of Nsp2,” *J. Biol. Chem.*, vol. 275, no. 23, pp. 17281–17287, 2000.

[140] M. Rikkonen, “Functional significance of the nuclear-targeting and NTP-binding motifs of semliki forest virus nonstructural protein nsP2,” *Virology*, vol. 218, no. 2, pp. 352–361, 1996.

[141] M. R. Singleton, M. S. Dillingham, and D. B. Wigley, “Structure and Mechanism of Helicases and Nucleic Acid Translocases,” *Annu. Rev. Biochem.*, vol. 76, no. 1, pp. 23–50, 2007.

[142] J. C. Rupp, K. J. Sokoloski, N. N. Gebhart, and R. W. Hardy, “Alphavirus RNA synthesis and non-structural protein functions,” *J. Gen. Virol.*, vol. 96, no. 9, pp. 2483–2500, 2015.

[143] J. K. Rubach, B. R. Wasik, J. C. Rupp, R. J. Kuhn, R. W. Hardy, and J. L. Smith, “Characterization of purified Sindbis virus nsP4 RNA-dependent RNA polymerase activity in vitro,” *Virology*, vol. 384, no. 1, pp. 201–208, 2009.

[144] S. Tomar, R. W. Hardy, J. L. Smith, and R. J. Kuhn, “Catalytic Core of Alphavirus Nonstructural Protein nsP4 Possesses Terminal Adenylyltransferase Activity,” *J. Virol.*, vol. 80, no. 20, pp. 9962–9969, 2006.

[145] R. Raju and H. V Huang, “Analysis of Sindbis virus promoter recognition in vivo, using novel vectors with two subgenomic mRNA promoters.,” *J. Virol.*, vol. 65, no. 5, pp. 2501–2510, 1991.

[146] H. Garoff, D. Huylebroeck, A. Robinson, U. Tillman, and P. Liljestrom, “The signal sequence of the p62 protein of Semliki Forest virus is involved in initiation but not in completing chain translocation,” *J. Cell Biol.*, vol. 111, no. 3, pp. 867–876, 1990.

[147] S. K. Jain, S. DeCandido, and M. Kielian, “Processing of the p62 envelope precursor protein of semliki forest virus,” *J. Biol. Chem.*, vol. 266, no. 9, pp. 5756–5761, 1991.

[148] I. De Curtis and K. Simons, “Dissection of Semliki Forest virus glycoprotein delivery from the trans-Golgi network to the cell surface in permeabilized BHK cells,” *Proc. Natl. Acad. Sci. U. S. A.*, vol. 85, no. 21, pp. 8052–8056, 1988.

[149] S. Mukhopadhyay *et al.*, “Mapping the structure and function of the E1 and E2 glycoproteins in alphaviruses,” *Structure*, vol. 14, no. 1, pp. 63–73, 2006.

[150] M. Kielian, C. Chanel-Vos, and M. Liao, “Alphavirus entry and membrane fusion,” *Viruses*, vol. 2, no. 4, pp. 796–825, 2010.

[151] R. Zhang *et al.*, “4.4 Å cryo-EM structure of an enveloped alphavirus Venezuelan equine encephalitis virus.,” *EMBO J.*, vol. 30, no. 18, pp. 3854–63, 2011.

[152] H. Garoff, K. Simons, and O. Renkonen, “Isolation and characterization of the membrane proteins of Semliki Forest virus,” *Virology*, vol. 61, no. 2, pp. 493–504, 1974.

[153] B. Simizu, K. Yamamoto, K. Hashimoto, and T. Ogata, “Structural proteins of Chikungunya virus.,” *J. Virol.*, vol. 51, no. 1, pp. 254–258, 1984.

[154] K. Gaedigk-Nitschko and M. J. Schlesinger, “The sindbis virus 6K protein can be detected in virions and is acylated with fatty acids,” *Virology*, vol. 175, no. 1, pp. 274–281, 1990.

[155] P. Liljeström, S. Lusa, D. Huylebroeck, and H. Garoff, “In vitro mutagenesis of a full-length cDNA clone of Semliki Forest virus: the small 6,000-molecular-weight membrane protein modulates virus release.,” *J. Virol.*, vol. 65, no. 8, pp. 4107–4113, 1991.

[156] S. Lusa, H. Garoff, and P. Liueström, “Fate of the 6K membrane protein of semliki forest virus during virus assembly,” *Virology*, vol. 185, no. 2, pp. 843–846, 1991.

[157] J. V. Melton, G. D. Ewart, R. C. Weir, P. G. Board, E. Lee, and P. W. Gage, “Alphavirus 6K proteins form ion channels,” *J. Biol. Chem.*, vol. 277, no. 49, pp. 46923–46931, 2002.

[158] V. Madan, M. A. Sanz, and L. Carrasco, “Requirement of the vesicular system for membrane permeabilization by Sindbis virus,” *Virology*, vol. 332, no. 1, pp. 307–315, 2005.

[159] V. Madan, A. Castelló, and L. Carrasco, “Viroporins from RNA viruses induce caspase-dependent apoptosis,” *Cell. Microbiol.*, vol. 10, no. 2, pp. 437–451, 2008.

[160] M. A. Sanz and L. Carrasco, “Sindbis Virus Variant with a Deletion in the 6K Gene Shows Defects in Glycoprotein Processing and Trafficking: Lack of Complementation by a Wild-Type 6K Gene intrans,” *J. Virol.*, vol. 75, no. 16, pp. 7778–7784, 2001.

[161] H. Garoff, A. M. Frischauf, K. Simons, H. Lehrach, and H. Delius, “Nucleotide sequence of cDNA coding for semliki forest virus membrane glycoproteins,” *Nature*, vol. 288, no. 5788, pp. 236–241, 1980.

[162] A. Omar and H. Koblet, “Semliki forest virus particles containing only the E1 envelope glycoprotein are infectious and can induce cell-cell fusion,” *Virology*, vol. 166, no. 1, pp. 17–23, 1988.

[163] J. M. Wahlberg and H. Garoff, “Membrane fusion process of Semliki Forest virus I: Low pH-induced rearrangement in spike protein quaternary structure precedes virus penetration into cells,” *J. Cell Biol.*, vol. 116, no. 2, pp. 339–348, 1992.

[164] C. Chevillon, L. Briant, F. Renaud, and C. Devaux, “The Chikungunya threat: an ecological and evolutionary perspective,” *Trends Microbiol.*, vol. 16, no. 2, pp. 80–88, 2008.

[165] T. L. Tellinghuisen, A. E. Hamburger, B. R. Fisher, R. Ostendorp, and R. J. Kuhn, “In Vitro Assembly of Alphavirus Cores by Using Nucleocapsid Protein Expressed in Escherichia coli,” *J. Virol.*, vol. 73, no. 7, pp. 5309–5319, 1999.

[166] R. Holland Cheng *et al.*, “Nucleocapsid and glycoprotein organization in an enveloped virus,” *Cell*, vol. 80, no. 4, pp. 621–630, 1995.

[167] R. Zhang *et al.*, “4.4 Å cryo-EM structure of an enveloped alphavirus Venezuelan equine encephalitis virus,” *EMBO J.*, vol. 30, no. 18, pp. 3854–3863, 2011.

[168] A. Helenius, J. Kartenbeck, K. Simons, and E. Fries, “On the entry of semliki forest virus into BHK-21 cells,” *J. Cell Biol.*, vol. 84, no. 2, pp. 404–420, 1980.

[169] M. Marsh, E. Bolzau, and A. Helenius, “Penetration of semliki forest virus from acidic prelysosomal vacuoles,” *Cell*, vol. 32, no. 3, pp. 931–940, 1983.

[170] J. M. Wahlberg, R. Bron, J. Wilschut, and H. Garoff, “Membrane fusion of Semliki Forest virus involves homotrimers of the fusion protein.,” *J. Virol.*, vol. 66, no. 12, pp. 7309–7318, 1992.

[171] D. L. Gibbons, A. Ahn, P. K. Chatterjee, and M. Kielian, “Formation and Characterization of the Trimeric Form of the Fusion Protein of Semliki Forest Virus,” *J. Virol.*, vol. 74, no. 17, pp. 7772–7780, 2000.

[172] P. M. Grimley, I. K. Berezesky, and R. M. Friedman, “Cytoplasmic structures associated with an arbovirus infection: loci of viral ribonucleic acid synthesis.,” *J. Virol.*, vol. 2, no. 11, pp. 1326–1338, 1968.

[173] H. Garoff, M. Sjöberg, and R. H. Cheng, “Budding of alphaviruses,” *Virus Res.*, vol. 106, no. 2, pp. 103–116, 2004.

[174] P. Soonsawad *et al.*, “Structural evidence of glycoprotein assembly in cellular membrane compartments prior to Alphavirus budding.,” *J. Virol.*, vol. 84, no. 21, pp. 11145–51, Nov. 2010.

[175] L. Echavarria-Consuegra, J. M. Smit, and F. Reggiori, “Role of autophagy during the replication and pathogenesis of common mosquito-borne flavi- and alphaviruses,” *Open Biol.*, vol. 9, no. 3, 2019.

[176] M. Mussgay and J. Weibel, “Electron Microscopic and Biological Studies on the Growth of Venezuelan Equine Encephalitis Virus in KB Cells,” *Virology*, vol. 62, pp. 52–62, 1962.

[177] K. E. Owen and R. J. Kuhn, “Alphavirus budding is dependent on the interaction between the nucleocapsid and hydrophobic amino acids on the cytoplasmic domain of the E2 envelope glycoprotein.,” *Virology*, vol. 230, no. 2, pp. 187–96, 1997.

[178] H. Zhao, B. Lindqvist, H. Garoff, C. H. von Bonsdorff, and P. Liljestrom, “A tyrosine-based motif in the cytoplasmic domain of the alphavirus envelope protein is essential for budding,” *EMBO J.*, vol. 13, no. 18, pp. 4204–4211, 1994.

[179] L. N. Liu, H. Lee, R. Hernandez, and D. T. Brown, “Mutations in the endo domain of sindbis virus glycoprotein E2 block phosphorylation, reorientation of the endo domain, and nucleocapsid binding,” *Virology*, vol. 222, no. 1, pp. 236–246, 1996.

[180] G. Griffiths, P. Quinn, and G. Warren, “Dissection of the Golgi Complex. I. Monensin Inhibits the Transport of Viral Membrane Proteins from Medial to Trans Golgi Cisternae in Baby Hamster Kidney Cells Infected with Semliki Forest Virus,” *J. Cell Biol.*, vol. 96, no. 3, pp. 835–850, 1983.

[181] G. Griffiths, S. D. Fuller, R. Back, M. Hollinshead, S. Pfeiffer, and K. Simons, “The dynamic nature of the Golgi complex.,” *J. Cell Biol.*, vol. 108, no. 2, pp. 277–97, 1989.

[182] R. S. Brown, J. J. Wan, and M. Kielian, “The Alphavirus Exit Pathway: What We Know and What We Wish We Knew,” *Viruses*, vol. 10, no. 2, p. 89, 2018.

[183] J. Krijnse-Locker, M. Ericsson, P. J. M. Rottier, and G. Griffiths, “Characterization of the budding compartment of mouse hepatitis virus: Evidence that transport from the RER to the Golgi complex requires only one vesicular transport step,” *J. Cell Biol.*, vol. 124, no. 1–2, pp. 55–70, 1994.

[184] M. Puhka, H. Vihinen, M. Joensuu, and E. Jokitalo, “Endoplasmic reticulum remains continuous and undergoes sheet-to-tubule transformation during cell division in mammalian cells,” *J. Cell Biol.*, vol. 179, no. 5, pp. 895–909, 2007.

[185] M. Puhka, M. Joensuu, H. Vihinen, I. Belevich, and E. Jokitalo, “Progressive sheet-to-tubule transformation is a general mechanism for endoplasmic reticulum partitioning in dividing mammalian cells,” *Mol. Biol. Cell*, vol. 23, pp. 2424–2432, 2012.

[186] M. West, N. Zurek, A. Hoenger, and G. K. Voeltz, “A 3D analysis of yeast ER structure reveals how ER domains are organized by membrane curvature,” *J. Cell Biol.*, vol. 193, no. 2, pp. 333–346, 2011.

[187] J. Nixon-Abell *et al.*, “Increased spatiotemporal resolution reveals highly dynamic dense tubular matrices in the peripheral ER,” *Science (80-.).*, vol. 354, no. 6311, 2016.

[188] L. S. Sturman and K. K. Takemoto, “Enhanced growth of a murine coronavirus in transformed mouse cells.,” *Infect. Immun.*, vol. 6, no. 4, pp. 501–507, 1972.

[189] J. A. Robb and C. W. Bond, “Pathogenic murine coronaviruses I. Characterization of biological behavior in vitro and virus-specific intracellular RNA of strongly neurotropic JHMV and weakly neurotropic A59V viruses,” *Virology*, vol. 94, no. 2, pp. 352–370, 1979.

[190] M. C. Freeman, R. L. Graham, X. Lu, C. T. Peek, and M. R. Denison, “Coronavirus Replicase-Reporter Fusions Provide Quantitative Analysis of Replication and Replication Complex Formation,” *J. Virol.*, vol. 88, no. 10, pp. 5319–5327, 2014.

[191] J. O. Fleming, R. A. Shubin, M. A. Sussman, N. Casteel, and S. A. Stohlman, “Monoclonal Antibodies to the Matrix (E1) Glycoprotein of Mouse Hepatitis Virus Protect Mice from Encephalitis,” *Virology*, vol. 168, pp. 162–167, 1989.

[192] M. D. Abràmoff, P. J. Magalhães, and S. J. Ram, “Image processing with ImageJ,” *Biophotonics Int.*, vol. 11, no. 7, pp. 36–41, 2004.

[193] J. Schindelin *et al.*, “Fiji: An open-source platform for biological-image analysis,” *Nat. Methods*, vol. 9, no. 7, pp. 676–682, 2012.

[194] P. Thévenaz and M. Unser, “User-Friendly Semiautomated Assembly of Accurate Image Mosaics in Microscopy,” *Microsc. Res. Tech.*, vol. 70, no. 2, pp. 135–146, 2007.

[195] J. R. Kremer, D. N. Mastronarde, and J. R. McIntosh, “Computer visualization of three-dimensional image data using IMOD.,” *J. Struct. Biol.*, vol. 116, no. 1, pp. 71–76, 1996.

[196] D. Mastronarde, “SerialEM: A Program for Automated Tilt Series Acquisition on Tecnai Microscopes Using Prediction of Specimen Position,” *Microsc. Microanal.*, vol. 9, no. Suppl 2, pp. 1182–1183, 2003.

[197] I. Belevich, M. Joensuu, D. Kumar, H. Vihinen, and E. Jokitalo, “Microscopy Image Browser: A Platform for Segmentation and Analysis of Multidimensional Datasets,” *PLoS Biol.*, vol. 14, no. 1, pp. 1–13, 2016.

[198] R. J. De Groot, R. W. Van Leen, M. J. Dalderup, H. Vennema, M. C. Horzinek, and W. J. Spaan, "Stably expressed FIPV peplomer protein induces cell fusion and elicits neutralizing antibodies in mice," *Virology*, vol. 171, no. 2, pp. 493–502, Aug. 1989.

[199] L. S. Sturman, K. V Holmes, and J. Behnke, "Isolation of coronavirus envelope glycoproteins and interaction with the viral nucleocapsid.," *J. Virol.*, vol. 33, no. 1, pp. 449–462, 1980.

[200] A. H. de Wilde *et al.*, "MERS-coronavirus replication induces severe in vitro cytopathology and is strongly inhibited by cyclosporin A or interferon-α treatment," *J. Gen. Virol.*, vol. 94, no. PART8, pp. 1749–1760, 2013.

[201] M. Hayashi-Nishino, N. Fujita, T. Noda, A. Yamaguchi, T. Yoshimori, and A. Yamamoto, "Electron tomography reveals the endoplasmic reticulum as a membrane source for autophagosome formation," *Autophagy*, vol. 6, no. 2, pp. 301–303, 2010.

[202] T. Uemura *et al.*, "A Cluster of Thin Tubular Structures Mediates Transformation of the Endoplasmic Reticulum to Autophagic Isolation Membrane," *Mol. Cell. Biol.*, vol. 34, no. 9, pp. 1695–1706, 2014.

[203] K. W. Pedersen, Y. Van Der Meer, N. Roos, and E. J. Snijder, "Open Reading Frame 1a-Encoded Subunits of the Arterivirus Replicase Induce Endoplasmic Reticulum-Derived Double-Membrane Vesicles Which Carry the Viral Replication Complex," *J. Virol.*, vol. 73, no. 3, pp. 2016–2026, 1999.

[204] S. Miller and J. Krijnse-Locker, "Modification of intracellular membrane structures for virus replication," *Nat. Rev. Microbiol.*, vol. 6, no. 5, pp. 363–74, May 2008.

[205] B. Wolk, B. Buchele, D. Moradpour, and C. M. Rice, "A Dynamic View of Hepatitis C Virus Replication Complexes," *J. Virol.*, vol. 82, no. 21, pp. 10519–10531, 2008.

[206] I. Monastyrska, M. Ulasli, P. J. M. Rottier, J. L. Guan, F. Reggiori, and C. A. M. De Haan, "An autophagy-independent role for LC3 in equine arteritis virus replication," *Autophagy*, vol. 9, no. 2, pp. 164–174, 2013.

[207] M. Sharma *et al.*, "Japanese encephalitis virus replication is negatively regulated by autophagy and occurs on LC3-I- and EDEM1-containing membranes," *Autophagy*, vol. 10, no. 9, pp. 1637–1651, 2014.

[208] M. Alirezaei, C. T. Flynn, M. R. Wood, S. Harkins, and J. L. Whitton, "Coxsackievirus can exploit LC3 in both autophagy-dependent and -independent manners in vivo," *Autophagy*, vol. 11, no. 8, pp. 1389–1407, 2015.

[209] A. C. Sims, J. Ostermann, and M. R. Denison, "Mouse Hepatitis Virus Replicase Proteins Associate with Two Distinct Populations of Intracellular Membranes," *J. Virol.*, vol. 74, no. 12, pp. 5647–5654, 2000.

[210] A. G. Bost, E. Prentice, and M. R. Denison, "Mouse hepatitis virus replicase protein complexes are translocated to sites of M protein accumulation in the ERGIC at late times of infection," *Virology*, vol. 285, pp. 21–29, 2001.

[211] M. C. Hagemeijer, A. M. Vonk, I. Monastyrska, P. J. M. Rottier, and C. a M. de Haan, "Visualizing coronavirus RNA synthesis in time by using click chemistry," *J. Virol.*, vol. 86, no. 10, pp. 5808–16, May 2012.

[212] H. M. N. Al-Mulla *et al.*, "Competitive Fitness in Coronaviruses Is Not Correlated with Size or Number of Double-Membrane Vesicles under Reduced-Temperature Growth Conditions," *MBio*, vol. 5, no. 2, pp. e01107-13, 2014.

[213] L. M. Westrate, J. E. Lee, W. A. Prinz, and G. K. Voeltz, "Form Follows Function: The Importance of Endoplasmic Reticulum Shape," *Annu. Rev. Biochem.*, vol. 84, no. 1, pp. 791–811, 2015.

[214] R. Heald and O. Cohen-Fix, "Morphology and function of membrane-bound organelles," *Curr. Opin. Cell Biol.*, vol. 26, no. 1, pp. 79–86, 2014.

[215] Y. H. Chen *et al.*, "Phosphatidylserine vesicles enable efficient en bloc transmission of enteroviruses," *Cell*, vol. 160, no. 4, pp. 619–630, 2015.

[216] M. Hollinshead, H. L. Johns, C. L. Sayers, C. Gonzalez-Lopez, G. L. Smith, and G. Elliott, "Endocytic tubules regulated by Rab GTPases 5 and 11 are used for envelopment of herpes simplex virus," *EMBO J.*, vol. 31, no. 21, pp. 4204–4220, 2012.

[217] N. Y. Hsu *et al.*, "Viral reorganization of the secretory pathway generates distinct organelles for RNA replication," *Cell*, vol. 141, no. 5, pp. 799–811, 2010.

[218] N. Gahmberg, E. Kuismanen, S. Keränen, and R. F. Pettersson, "Uukuniemi virus glycoproteins accumulate in and cause morphological changes of the Golgi complex in the absence of virus maturation.," *J. Virol.*, vol. 57, no. 3, pp. 899–906, 1986.

[219] J. Jose, J. Snyder, and R. Kuhn, "A structural and functional perspective of alphavirus replication and assembly," *Future Microbiol.*, vol. 4, pp. 837–856, 2009.

[220] J. H. Strauss and E. G. Strauss, "The alphaviruses: Gene expression, replication, and evolution," *Microbiological Reviews*, vol. 58, no. 3. pp. 491–562, 1994.

[221] C. Sanchez-San Martin, C. Y. Liu, and M. Kielian, "Dealing with low pH: entry and exit of alphaviruses and flaviviruses," *Trends Microbiol.*, vol. 17, no. 11, pp. 514–521, 2009.

[222] P. Kujala, A. Ikäheimonen, N. Ehsani, and H. Vihinen, "Biogenesis of the Semliki Forest Virus RNA Replication Complex Biogenesis of the Semliki Forest Virus RNA Replication Complex," vol. 75, no. 8, 2001.

[223] S. R. Radoshitzky *et al.*, "siRNA Screen Identifies Trafficking Host Factors that Modulate Alphavirus Infection," *PLoS Pathog.*, vol. 12, no. 3, pp. 1–30, 2016.

[224] N. Ariotti *et al.*, "Modular Detection of GFP-Labeled Proteins for Rapid Screening by Electron Microscopy in Cells and Organisms," *Dev. Cell*, vol. 35, no. 4, pp. 513–525, 2015.

[225] R. Sengupta, M. J. Poderycki, and S. Mattoo, "CryoAPEX – an electron tomography tool for subcellular localization of membrane proteins," *J. Cell Sci.*, vol. 132, no. 6, p. jcs222315, 2019.

[226] R Core Team, "R: A language and environment for statistical computing. R Foundation for Statistical Computing," 2019. [Online]. Available: https://www.r-project.org/.

[227] E. M. Mihelc, S. Angel, R. V Stahelin, and S. Mattoo, "The CryoAPEX Method for Electron Microscopy Analysis of Membrane Protein Localization Within Ultrastructurally-Preserved Cells," *J. Vis. Exp.*, p. e60677, 2020.

[228] R. L. Knorr, R. Lipowsky, and R. Dimova, "Autophagosome closure requires membrane scission," *Autophagy*, vol. 11, no. 11, pp. 2134–2137, 2015.

[229] M. R. Fernandez-Fernandez, D. Ruiz-Garcia, E. Martin-Solana, F. J. Chichon, J. L. Carrascosa, and J.-J. Fernandez, "3D electron tomography of brain tissue unveils distinct Golgi structures that sequester cytoplasmic contents in neurons.," *J. Cell Sci.*, vol. 130, pp. 83–90, 2016.

[230] M. G. Martinez, E.-L. Snapp, G. S. Perumal, F. P. Macaluso, and M. Kielian, "Imaging the Alphavirus Exit Pathway," *J. Virol.*, vol. 88, no. 12, pp. 6922–6933, 2014.

[231] D. Corda, M. L. Barretta, R. I. Cervigni, and A. Colanzi, "Golgi complex fragmentation in G2/M transition: An organelle-based cell-cycle checkpoint," *IUBMB Life*, vol. 64, no. 8. pp. 661–670, 2012.

[232] S. Mukherjee, R. Chiu, S. M. Leung, and D. Shields, "Fragmentation of the Golgi apparatus: An early apoptotic event independent of the cytoskeleton," *Traffic*, vol. 8, no. 4, pp. 369–378, 2007.

[233] R. Chiu, L. Novikov, S. Mukherjee, and D. Shields, "A caspase cleavage fragment of p115 induces fragmentation of the Golgi apparatus and apoptosis.," *J. Cell Biol.*, vol. 159, no. 4, pp. 637–648, 2002.

[234] G. Joshi, Y. Chi, Z. Huang, and Y. Wang, "Aβ-induced Golgi fragmentation in Alzheimer's disease enhances Aβ production.," *Proc. Natl. Acad. Sci. U. S. A.*, vol. 111, no. 13, pp. E1230-9, 2014.

[235] A. Petrosyan, "Onco-Golgi: Is Fragmentation a Gate to Cancer Progression?," *Biochem. Mol. Biol. J.*, vol. 1, no. 1, p. 6, 2015.

[236] Z. Lu, D. Joseph, E. Bugnard, K. J. M. Zaal, and E. Ralston, "Golgi complex reorganization during muscle differentiation: Visualization in living cells and mechanism," *Mol. Biol. Cell*, vol. 12, no. 4, pp. 795–808, 2001.

[237] V. L. Rudick, M. J. Rudick, and A.-M. Brun-Zinkernagel, "Amplification of the Golgi complex in MDCK cells secreting human growth hormone," *J. Cell Sci.*, vol. 104, pp. 509–520, 1993.

[238] C. Hanus and M. D. Ehlers, "Secretory outposts for the local processing of membrane cargo in neuronal dendrites," *Traffic*, vol. 9, no. 9. pp. 1437–1445, 2008.

[239] M. E. Kreft, D. Giandomenico, G. V Beznoussenko, N. Resnik, A. A. Mironov, and K. Jezernik, "Golgi apparatus fragmentation as a mechanism responsible for uniform delivery of uroplakins to the apical plasma membrane of uroepithelial cells," *Biol. Cell*, vol. 102, no. 11, pp. 593–607, 2010.

[240] T. Višnjar *et al.*, "Uroplakin traffic through the Golgi apparatus induces its fragmentation: new insights from novel in vitro models," *Sci. Rep.*, vol. 7, no. 12842, 2017.

[241] M. C. Hagemeijer *et al.*, "Dynamics of coronavirus replication-transcription complexes.," *J. Virol.*, vol. 84, no. 4, pp. 2134–49, Feb. 2010.

[242] E. Lavi, Q. Wang, S. R. Weiss, and N. K. Gonatas, “Syncytia formation induced by coronavirus infection is associated with fragmentation and rearrangement of the Golgi apparatus,” *Virology*, vol. 221, no. 2, pp. 325–334, 1996.

[243] B. D. Engel, M. Schaffer, S. Albert, S. Asano, J. M. Plitzko, and W. Baumeister, “In situ structural analysis of Golgi intracisternal protein arrays.,” *Proc. Natl. Acad. Sci. U. S. A.*, vol. 112, no. 36, pp. 11264–9, 2015.

[244] B. Huang, M. Bates, and X. Zhuang, “Super-Resolution Fluorescence Microscopy,” *Annu. Rev. Biochem.*, vol. 78, pp. 993–1016, 2009.

[245] A. M. Sydor, K. J. Czymmek, E. M. Puchner, and V. Mennella, “Super-Resolution Microscopy : From Single Molecules to Supramolecular Assemblies,” *Trends Cell Biol.*, vol. 25, no. 12, pp. 730–748, 2015.

[246] J. Vangindertael, R. Camacho, W. Sempels, H. Mizuno, P. Dedecker, and K. P. F. Janssen, “An introduction to optical super-resolution microscopy for the adventurous biologist,” *Methods Appl. Fluoresc.*, vol. 6, no. 2, p. 022003, 2018.

[247] J. De Mey, M. Moeremans, G. Geuens, R. Nuydens, and M. De Brabander, “High resolution light and electron microscopic localization of tubulin with the IGS (Immuno Gold Staining) method,” *Cell Biol. Int. Rep.*, vol. 5, no. 9, pp. 889–899, 1981.

[248] W. Faulk and G. Taylor, “An immunocolloid method for the electron microscope,” *Immunochemistry*, vol. 8, pp. 1081–1083, 1971.

[249] W. J. Brown, E. Constantinescu, and M. G. Farquhar, “Redistribution of Mannose-6-Phosphate Receptors Induced by Tunicamycin and Chloroquine,” *J. Cell Biol.*, vol. 99, no. July, pp. 320–326, 1984.

[250] W. J. Brown and M. G. Farquhar, “The Mannose-6-phosphate Enzymes Is Concentrated Receptor for Lysosomal in Cis Golgi Cisternae,” *Cell*, vol. 36, no. February 1984, pp. 295–307, 1984.

[251] L. A. Sternberger, P. H. Hardy, J. J. Cuculis, and H. G. Meyer, “The unlabeled antibody enzyme method of immunohistochemistry,” *J. Histochem. Cytochem.*, vol. 18, no. 5, pp. 315–333, 1970.

[252] C. Oliver, “Pre-embedding Labeling Methods,” in *Immunocytochemical Methods and Protocols*, vol. 588, C. Oliver and M. C. Jamur, Eds. Humana Press, 2010, pp. 381–386.

[253] E. V Polishchuk and R. S. Polishchuk, “Pre-embedding labeling for subcellular detection of molecules with electron microscopy,” *Tissue Cell*, vol. 57, no. November 2018, pp. 103–110, 2019.

[254] R. S. Polishchuk, E. V Polishchuk, and A. Luini, “Visualizing Live Dynamics and Ultrastructure of Intracellular Organelles with Preembedding Correlative Light-Electron Microscopy,” in *Correlative Light and Electron Microscopy*, vol. 111, T. Mueller-Reichert and P. Verkade, Eds. Elsevier, 2012, pp. 21–35.

[255] B. M. Humbel, M. D. M. De Jong, W. H. Müller, and A. J. Verkleij, “Pre-embedding immunolabeling for electron microscopy: An evaluation of permeabilization methods and markers,” *Microsc. Res. Tech.*, vol. 42, no. April, pp. 43–58, 1998.

[256] U. Schnell, F. Dijk, K. A. Sjollema, and B. N. G. Giepmans, “Immunolabeling artifacts and the need for live-cell imaging,” *Nat. Methods*, vol. 9, no. 2, pp. 152–158, 2012.

[257] J. F. Hainfeld and R. D. Powell, “New Frontiers in Gold Labeling,” *J. Histochem. Cytochem.*, vol. 48, no. 4, pp. 471–480, 2000.

[258] J. F. Hainfeld and F. R. Furuya, “A 1.4-nm Gold Cluster Covalently Attached to Antibodies Improves Immunolabeling,” *J. Histochem. Cytochem.*, vol. 40, no. 2, pp. 177–184, 1992.

[259] W. Baschong and Y. Stierhof, “Preparation, Use, and Enlargement of Ultrasmall Gold Particles in Immunoelectron Microscopy,” *Microsc. Res. Tech.*, vol. 42, no. March, pp. 66–79, 1998.

[260] J. Roth, M. Bendayan, and L. Orci, “Ultrastructural loclaization of intracellular antigens by the use of Protein A-gold complex,” *J. Histochem. Cytochem.*, vol. 26, no. 12, pp. 1074–1081, 1978.

[261] B. L. Armbruster, E. Carlemalm, R. Chiovetti, R. M. Garavito, J. A. Hobot, and E. Kellenberger, “Specimen preparation for electron microscopy using low temperature embedding resins,” *J. Microsc.*, vol. 126, no. November 1981, pp. 77–85, 1982.

[262] C. B. Fowler, T. J. O. Leary, and J. T. Mason, “Modeling formalin fixation and histological processing with ribonuclease A : effects of ethanol dehydration on reversal of formaldehyde cross-links,” *Lab. Investig.*, vol. 88, pp. 785–791, 2008.

[263] G. R. Newman and J. A. Hobot, “Modern Acrylics for Post-embedding Immunostaining Techniques,” *J. Histochem. Cytochem.*, vol. 35, no. 9, pp. 971–981, 1987.

[264] K. T. Tokuyasu, “A technique for ultracryotomy of cell suspensions and tissues,” *J. Cell Biol.*, vol. 57, no. 2, pp. 551–565, 1973.

[265] K. T. Tokuyasu, “Application of cryoultramicrotomy to immunocytochemistry,” *J. Microsc.*, vol. 143, no. August, pp. 139–149, 1986.

[266] W. Möbius and G. Posthuma, “Sugar and ice : Immunoelectron microscopy using cryosections according to the Tokuyasu method,” *Tissue Cell*, vol. 57, no. September 2018, pp. 90–102, 2019.

[267] G. Gaietta *et al.*, “Multicolor and Electron Microscopic Imaging of Connexin Trafficking,” *Science (80-.).*, vol. 296, no. April, pp. 503–508, 2002.

[268] C. Uttamapinant *et al.*, “A fluorophore ligase for site-specific protein labeling inside living cells,” *Proc Natl Acad Sci U S A*, vol. 107, no. 24, pp. 10914–10919, 2010.

[269] B. Porstmann, T. Porstmann, E. Nugel, and U. Evers, “Which of the Commonly Used Marker Enzymes Gives the Best Results in Colorimetric and Fluorimetric Enzyme Immunoassays: Horseradish Peroxidase, Alkaline Phosphatase or Beta-Galactosidase,” *J. Immunol. Methods*, vol. 79, pp. 27–37, 1985.

[270] X. Shu *et al.*, “A Genetically Encoded Tag for Correlated Light and Electron Microscopy of Intact Cells , Tissues , and Organisms,” *PLoS Biol.*, vol. 9, no. 4, p. e1001041, 2011.

[271] C. P. Mercogliano and D. J. DeRosier, “Concatenated metallothionein as a clonable gold label for electron microscopy.,” *J. Struct. Biol.*, vol. 160, no. 1, pp. 70–82, Oct. 2007.

[272] Q. Wang, C. P. Mercogliano, and J. Löwe, "A ferritin-based label for cellular electron cryotomography.," *Structure*, vol. 19, no. 2, pp. 147–54, Feb. 2011.

[273] C. Risco, E. Sanmartín-Conesa, W.-P. Tzeng, T. K. Frey, V. Seybold, and R. J. de Groot, "Specific, sensitive, high-resolution detection of protein molecules in eukaryotic cells using metal-tagging transmission electron microscopy.," *Structure*, vol. 20, no. 5, pp. 759–66, May 2012.

[274] C. Hopkins, A. Gibson, J. Stinchcombe, and C. E. Futter, "Chimeric Molecules Employing Horseradish Peroxidase as Reporter Enzyme for Protein Localization in the Electron Microscope," in *Methods in Enzymology*, vol. 327, J. Thorner, S. D. Emr, and J. N. Abelson, Eds. 2000, pp. 35–45.

[275] C. Hoffmann *et al.*, "Fluorescent labeling of tetrcysteine-tagged proteins in intact cells," *Nat. Protoc.*, vol. 5, no. 10, pp. 1666–1677, 2010.

[276] J. D. Martell *et al.*, "Engineered ascorbate peroxidase as a genetically encoded reporter for electron microscopy," *Nat. Biotechnol.*, vol. 30, no. 11, pp. 1143–1150, 2012.

[277] S. S. Lam *et al.*, "Directed evolution of APEX2 for electron microscopy and proximity labeling," *Nat. Methods*, vol. 12, no. 1, 2015.

[278] J. D. Martell, T. J. Deerinck, S. S. Lam, M. H. Ellisman, and A. Y. Ting, "Electron microscopy using the genetically encoded APEX2 tag in cultured mammalian cells," *Nat. Protoc.*, vol. 12, no. 9, pp. 1792–1816, 2017.

[279] D. Studer, B. M. Humbel, and M. Chiquet, "Electron microscopy of high pressure frozen samples: Bridging the gap between cellular ultrastructure and atomic resolution," *Histochem. Cell Biol.*, vol. 130, no. 5, pp. 877–889, 2008.

[280] R. Dahl and L. A. Staehelin, "High-pressure Freezing for the Preservation of Biological Structure : Theory and Practice," *J. Electron Microsc. Tech.*, vol. 13, pp. 165–174, 1989.

[281] K. L. McDonald, "High-Pressure Freezing for Preservation of High Resolution Fine Structure and Antigenicity for Immunolabeling," in *Electron Microscopy Methods and Protocols*, vol. 117, N. Hajibagheri, Ed. Totowa, NJ: Humana Press, 1999, pp. 77–97.

[282] G. E. Sosinsky *et al.*, "The combination of chemical fixation procedures with high pressure freezing and freeze substitution preserves highly labile tissue ultrastructure for electron tomography applications," *J. Struct. Biol.*, vol. 161, pp. 359–371, 2008.

[283] E. D. Korn and R. A. Weisman, "Loss of lipids during preparation of amoebae for electron microscopy," *Biochem. Biophys. Acta*, vol. 116, no. 4, pp. 309–316, 1966.

[284] E. L. Snapp *et al.*, "Formation of stacked ER cisternae by low affinity protein interactions," *J. Cell Biol.*, vol. 163, no. 2, pp. 257–269, 2003.

[285] G. Sandig, E. Kärgel, R. Menzel, F. Vogel, T. Zimmer, and W. Schunck, "Regulation of endoplasmic reticulum biogenesis in response to cytochrome P450 overproduction," *Drug Metab. Rev.*, vol. 31, no. 2, pp. 393–410, 1999.

[286] P. W. Faber, G. T. Barnes, J. Srinidhi, J. Chen, J. F. Gusella, and M. E. Macdonald, "Huntingtin interacts with a family of WW domain proteins," *Hum. Mol. Genet.*, vol. 7, no. 9, pp. 1463–1474, 1998.

[287] C. A. Worby *et al.*, "Article The Fic Domain : Regulation of Cell Signaling by Adenylylation," *Mol. Cell*, vol. 34, no. 1, pp. 93–103, 2009.

[288] A. Sanyal *et al.*, "A Novel Link between Fic (Filamentation Induced by cAMP) - mediated Adenylylation / AMPylation and the Unfolded Protein Response," *J. Biol. Chem.*, vol. 290, no. 13, pp. 8482–8499, 2015.

[289] S. Mattoo *et al.*, "Comparative Analysis of Histophilus somni Immunoglobulin-binding Protein A (IbpA) with Other Fic Domain-containing Enzymes Reveals Differences in Substrate and Nucleotide Specificities," *J. Biol. Chem.*, vol. 286, no. 37, pp. 32834–32842, 2011.

[290] T. K. Tsang *et al.*, "High-quality ultrastructural preservation using cryofixation for 3D electron microscopy of genetically labeled tissues," *Elife*, vol. 7, pp. 1–23, 2018.

[291] T. H. Giddings, "Freeze-substitution protocols for improved visualization of membranes in high-pressure frozen samples.," *J. Microsc.*, vol. 212, no. Pt 1, pp. 53–61, Oct. 2003.

[292] K. L. McDonald and R. I. Webb, "Freeze substitution in 3 hours or less.," *J. Microsc.*, vol. 243, no. 3, pp. 227–33, Sep. 2011.

[293] K. McDonald, "Cryopreparation methods for electron microscopy of selected model systems.," *Methods Cell Biol.*, vol. 79, no. 06, pp. 23–56, Jan. 2007.

[294] C. Buser and P. Walther, "Freeze-substitution: the addition of water to polar solvents enhances the retention of structure and acts at temperatures around -60 degrees C.," *J. Microsc.*, vol. 230, no. Pt 2, pp. 268–77, May 2008.

[295] N. Jiménez, K. Vocking, E. G. Van Donselaar, B. M. Humbel, J. A. Post, and A. J. Verkleij, "Tannic acid-mediated osmium impregnation after freeze-substitution : A strategy to enhance membrane contrast for electron tomography," *J. Struct. Biol.*, vol. 166, no. 1, pp. 103–106, 2009.

[296] Y. Han, T. C. Branon, D. Boassa, D. Shechner, M. H. Ellisman, and A. Ting, "Directed Evolution of Split APEX2 Peroxidase," *ACS Chem. Biol.*, vol. 14, pp. 619–635, 2019.

[297] J. Kuipers, T. J. Van Ham, R. D. Kalicharan, U. Schnell, and B. N. G. Giepmans, "FLIPPER, a combinatorial probe for correlated live imaging and electron microscopy, allows identification and quantitative analysis of various cells and organelles," *Cell Tissue Res.*, vol. 360, pp. 61–70, 2015.

[298] Y. Zhou, G. Wang, P. Wang, Z. Li, T. Yue, and J. Wang, "Expanding APEX2 Substrates for Spatial-specific Labeling of Nucleic Acids and Proteins in Living Cells," *Angew. Chem. Int. Ed. Engl.*, p. In Press, 2019.

[299] M. Joesch *et al.*, "Reconstruction of genetically identified neurons imaged by serial-section electron microscopy," *Elife*, vol. 5, pp. 1–13, 2016.

PUBLICATION

Mihelc EM, Angel S, Stahelin RV, Mattoo S. (2020). The CryoAPEX Method for Electron Microscopy Analysis of Membrane Protein Localization Within Ultrastructurally-Preserved Cells. *Journal of Visualized Experiments* (156), e60677.